UNIVERSITY OF CALIFORNIA, SAN DIEGO

Web-Tapered Steel Beam-Column Elements for Nonlinear Analysis with Cyclic Loading

A Thesis submitted in partial satisfaction of the requirements
for the degree Master of Science

in

Structural Engineering

by

Brighton Laiman

Committee in charge:

Professor Chia-Ming Uang, Chair
Professor Joel Conte
Professor Gilberto Mosqueda
Professor Benson P. Shing

2014

The Thesis of Brighton Laiman is approved and it is acceptable in quality and form for publication on microfilm and electronically:

Chair

University of California, San Diego

2014

TABLE OF CONTENTS

LIST OF FIGURES

LIST OF TABLES

ACKNOWLEDGEMENTS

I would first and foremost like to thank Professor Chia-Ming Uang for giving me the opportunity to study under him. His support and actions as my advisor throughout my academic life have been invaluable and played an important role in developing, as well as expanding, my engineering knowledge and intuition.

I would like to thank Metal Building Manufacturers Association (MBMA) for their financial support of my research. I would like to thank Xi Zhang, Kim J.R. Rasmussen, and Hao Zhang for providing their modified source code of OpenSees implementation which served as a baseline for this research. I would also like to thank Dr. Matthew Smith for being a good friend and acting as a mentor throughout my graduate studies. His help and knowledge has played a significant role in terms of this research topic as I worked alongside him.

Finally, I would like to thank my father for always acting as my life advisor and always believing in my highest potential and my mother for always supporting me during rough times. Without both of their wisdom and guidance I would not be able to be where I am today.

VITA

2012	Bachelor of Science in Structural Engineering, University of California, San Diego, California
2014	Master of Science in Structural Engineering, University of California, San Diego, California

ABSTRACT OF THE THESIS

Web-Tapered Steel Beam-Column Elements
for Nonlinear Analysis with Cyclic Loading

by

Brighton Laiman

Master of Science in Structural Engineering

University of California, San Diego, 2014

Professor Chia-Ming Uang, Chair

Many of today's low-rise building structures consist of thin-walled metal members that form Metal Building Frames (MBFs). Members associated with MBFs typically involve tapered webs. Although use of web-tapered members for MBFs are driven by economical efficiency, understanding on how these type of members respond under seismic loading is limited. Design of web-tapered members generally is governed by lateral-torsional buckling (LTB) and local buckling. To better understand the seismic response of MBFs that buckle, use of numerical methods that can simulate buckling and post-buckling behavior are desirable. Since it is not inefficient to use elements such as shells or solids for extensive seismic analyses, development of a one-dimensional beam-

column element is researched and incorporated to the software OpenSees in order to capture warping and non-prismatic effects.

In addition to monotonic correlations, six full-scale web-tapered members cyclically tested at UCSD were analyzed using this proposed beam-column element. Parametric studies associated with these analyses were also performed and included variation of axial loads, initial imperfections, and residual stresses. Based on the predicted analyses, events of initial LTB were captured reasonably well. However, it was observed that the proposed element is limited in its capabilities by events of local buckling.

Because of local buckling limitation, attempt to expand the proposed element by introducing combined flange-web displacements was pursued. Although formulation of the updated element was successfully implemented, issues associated with initiating local buckling were observed during preliminary verification. Further development of incorporating initial displacements to the flanges is thus required.

1 INTRODUCTION

1.1 General

Metal buildings are typically designed to resist lateral loads, in their transverse direction (see Figure 1.1), through steel moment resisting frames composed of web-tapered I-shaped beams (i.e., rafters and columns), herein called metal building frames (MBF). The use of MBF is commonly seen in industrial, retail, office, educational, athletic, agricultural, arenas, storage, and other applications (Newman 2004). Because these structural systems under design loads experience moment gradients throughout each member, non-prismatic members are commonly used in order to be economically efficient.

Compared to a prismatic hot-rolled, wide-flange member, with compact sections, a web-tapered, built-up, I-shaped member with slender and noncompact sections is more complicated in behavior, analysis, and design (AISC 2010). The latter are prone to lateral-torsional buckling (LTB) and local buckling (LB), including flange local buckling (FLB) and web local buckling (WLB).

For seismic design, current design codes like Minimum Design Loads for Buildings and Other Structures ASCE 7-10 (ASCE 2010) and Seismic Design Manual AISC 341 (AISC 2010) assume that a MBF, thus designed, will go beyond elastic behavior and experience inelastic action, including yielding and buckling. To refine or develop a rational seismic design procedure, which recognizes the unique structural characteristics of the MBF, it is essential that the inelastic response at both the member and the system levels are readily and reliably simulated.

Numerical modeling for thin-walled metal members has become valuable and commonly used throughout structural analysis. Although the use of computer software for analyses may be appealing to the common user, poor choice of an element formulation can lead to high computational expense and unreliable results. Commercial software, such as ABAQUS (SIMULIA Inc. 2013), possess attributes which allow simulations of LTB and LB to occur given proper modeling and parameters. However, computational effort required by such software may be time consuming and inefficient in cases like a P695 study (FEMA 2009), when extensive nonlinear time-history analyses of frames involving yielding and buckling, under a suite of earthquake ground motions are required. Due to this inconvenience, alternative methods that can yield comparable results with less computational effort are highly desired.

The Open System for Earthquake Engineering System (OpenSees) is an open source software package in which the use of nonlinear elements, material models, and many other libraries can be formulated for numerical modeling (McKenna et al. 2000). Due to the nature of open source software, researchers globally are able to access, utilize, and modify the package for their particular needs.

OpenSees is written in C++ and each finite element module needed for an analysis is implemented as a class. Due to the framework and structure of OpenSees, addition and modifications of entities such as elements or material models can be done without prior knowledge of how the overall program functions globally. Since the formulation of new elements can be done through inheritance from existing elements, a developer can focus their efforts on their elements only.

Existing implementation of beam-column elements in OpenSees allows occurrence of Euler-type flexural buckling at the member level. But steel flexural members, especially those used in metal building construction, are also prone to LTB, which cannot be simulated by the existing beam-column elements. However, previous works, Alemdar (2001) and Chang (2006) for instance, have numerically shown that sophisticated beam-column element formulations can work exceptionally well at simulating this buckling mode. Kitipornchai and Trahair (1975) adapted differential equations for inelastic buckling of tapered monosymmetric I-beams under moment gradients and expanded them using the finite-integral method. Yang and McGuire (1986) developed an updated Lagrangian procedure for nonlinear analysis that included nonuniform torsion and the incorporation of a warping degree of freedom (DOF) at each node of a beam element. Yang and Yau (1987) derived the differential equations of equilibrium for tapered I-beams and developed a finite element formulation for beams taking into account geometric nonlinearities. Bradford et al. (1987) developed a geometrically nonlinear finite-element method applicable for inelastic lateral buckling of I-section beams and beam-columns based on a reference axis arbitrary passing a point along the midheight of the web. Ronagh et al. (2000) presented a finite element formulation through nonlinear Green-Lagrange axial strains and Kirchoff stress-resultants of beams with general variable cross-sections. Zhang et al. (2011) presented a nonlinear beam-column derivation for doubly symmetric members using linear and second order approximations of the Green-Lagrange strain equation and incorporated it into OpenSees. Based on these findings, it is desirable that a modified formulation that accounts for warping, non-prismatic web-taper, and Wagner effects (Alemdar 2001) are incorporated for studies of metal building applications.

In addition to LTB phenomenon, LB occurrence is also of concern in MBFs, because noncompact or slender sections are commonly used. Although design procedures handle these two phenomena as independent limit states, experimental cyclic testing (Smith et al. 2013) has shown that LTB and LB are quite often coupled together. Such an instance is seen in Figure 1.2, where a physical test beam specimen undergoes an initial event of LTB as well as FLB during cyclic testing. For this reason, it is desirable to develop a beam-column element that can simulate not only LTB but also FLB.

1.2 Objective

The objective of this research was to develop, in the framework of OpenSees, a three-dimensional, inelastic, beam-column element to simulate the cyclic response of web-tapered steel members. The element, termed Tapered Element A in this research, incorporates the warping and Wagner effects in order to simulate flexural buckling as well as lateral-torsional buckling. Tapered Element B is built on Tapered Element A, but with additional features included to simulate the local buckling effects as well.

Development and use of these two elements is limited to thin-walled members of singly-symmetric I-shaped sections. Furthermore, capabilities of these elements only accommodate non-prismatic features of tapered webs, but not tapered flanges. Capabilities of modeling members with singly-symmetric or doubly-symmetric I-shape geometries have shown to work well. Although the proposed elements do not consider tapered flange geometry, derivation techniques can include flange-taper in addition to the incorporated web-taper. Thorough modeling of the proposed elements are compared to published work to verify their diverse capability with varying boundary conditions, loading conditions,

geometric configurations, material properties, use of residual stresses, and member imperfections.

1.3 Organization of Thesis

Chapter 2 presents the development of Tapered Element A which incorporates warping and non-prismatic web-taper effects. Chapter 3 presents implementation of Tapered Element A into the OpenSees framework based on the work presented in Chapter 2. Chapter 4 documents correlation studies using Tapered Element A for members that are monotonically loaded. Chapter 5 documents analysis and correlation studies of six full-scale specimens that are cyclically loaded. Chapter 6 presents the development of Tapered Element B in order to include effects of LB. Finally, Chapter 7 provides a summary and conclusions from this research as well as suggestions for continued development of Tapered Element B.

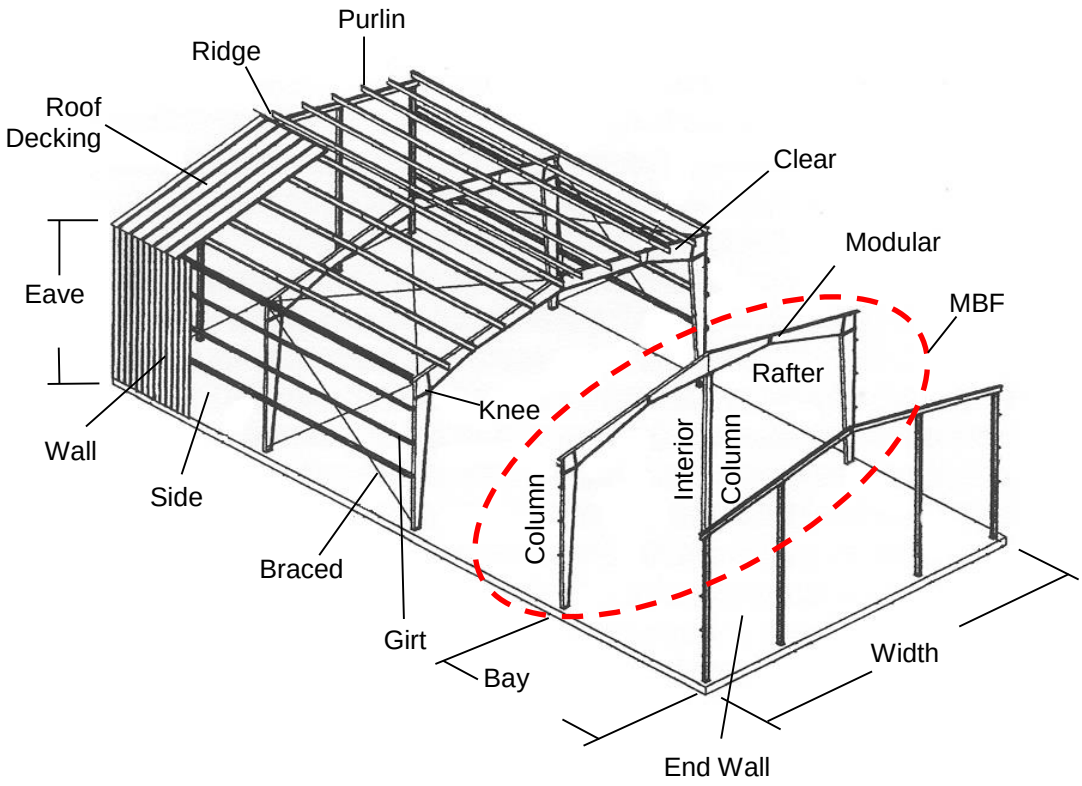

Figure 1.1 Metal Building Components (Newman 2004)

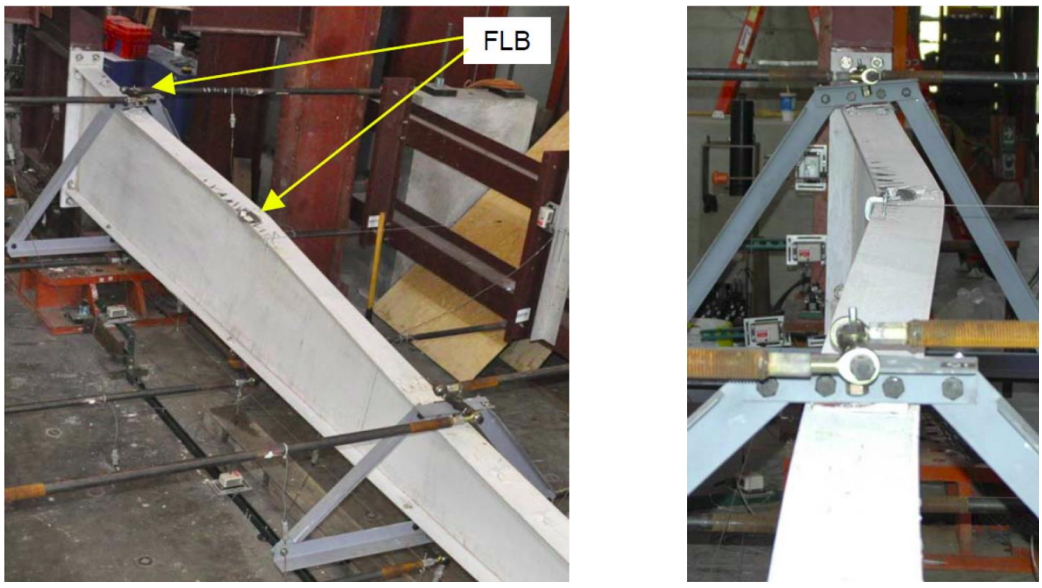

Figure 1.2 Global and Local Buckling Interaction with LTB (Smith et al. 2013)

2 DEVELOPMENT OF TAPERED ELEMENT A

2.1 General

LTB causes or results in large displacements and rotations experienced throughout the member. To handle these large deformations, the use of a corotational approach (Alemdar 2001) is typically involved in order to extract corresponding strain values from a deformed configuration. Constitutive relations allow the retrieval of the corresponding stresses as well as the tangent modulus of the material model. In addition, an element tangent stiffness matrix is developed for the proposed beam-column element, which is dependent on the cross-sectional properties as well as geometrical nonlinearities.

2.2 Three-Dimensional Geometrical Reference Frames

Applications of open thin-walled members that undergo large displacements and rotations throughout nonlinear analysis is commonly encountered in engineering practice. The capability of allowing such large displacements and rotations enables proper analytical buckling predictions as well as handling of post-buckling trajectories. Assessment of such situations can be done through use of a corotational approach (Crisfield 1990), which allows treatment of removing rigid body displacement modes (RBMs) in order to determine strain deformations from a corotational, or natural, reference frame. This corotational approach allows the behavior of a beam-column element to be represented in three related reference frames: the global frame, the local frame, and the natural frame. By removing RBMs from the global and local frames, the natural strain deformations for an element can be determined.

Corotational transformations are commonly used in nonlinear analyses. Thorough development and discussion of this geometrical transformation are described through works of Crisfield (1990), Alemdar (2001), Chang (2006), and by many others. Incorporation of the corotational approach in OpenSees is implemented and developed through the foundation of Crisfield's formulation. However, modification is necessary to extend the existing coordinate transformation class to allow for the extra warping DOFs.

In a typical 3-D beam-column element, the global and local frames each consists of six degrees-of-freedom (DOFs) at an element end node: three displacements and three rotations. Thus, a typical beam-column element consist of 12 DOFs. With the removal of RBMs, the same element has only seven DOFs in the natural frame: three local rotations at each end and an element axial elongation.

In addition to the DOFs seen in a typical beam-column element, the proposed element considers an additional DOF that represents warping at each end node. A physical depiction of this phenomenon is visualized in Figure 2.1. An undeformed state shows that the member segment has a perfectly plane cross-section. Once warping occurs, the top and bottom flanges of the cross-section twist in opposing directions with respect to the undeformed section as seen with the dashed segments. This event where the cross-section no longer remains plane is referred to as warping and is directly related to ϕ, the torsional (or twist) angle throughout the member (AISC 2003).

Within the proposed element, this additional DOF is added at each node to represent warping, such that the beam-column element has 14 DOFs total. Correspondingly, the element consists of 9 DOFs in the natural frame when warping contributions are considered. A representative depiction of the proposed element reference frames and

(a) Top Flange (b) Bottom Flange

Figure 2.1 Plan View of Cross-Sectional Warping

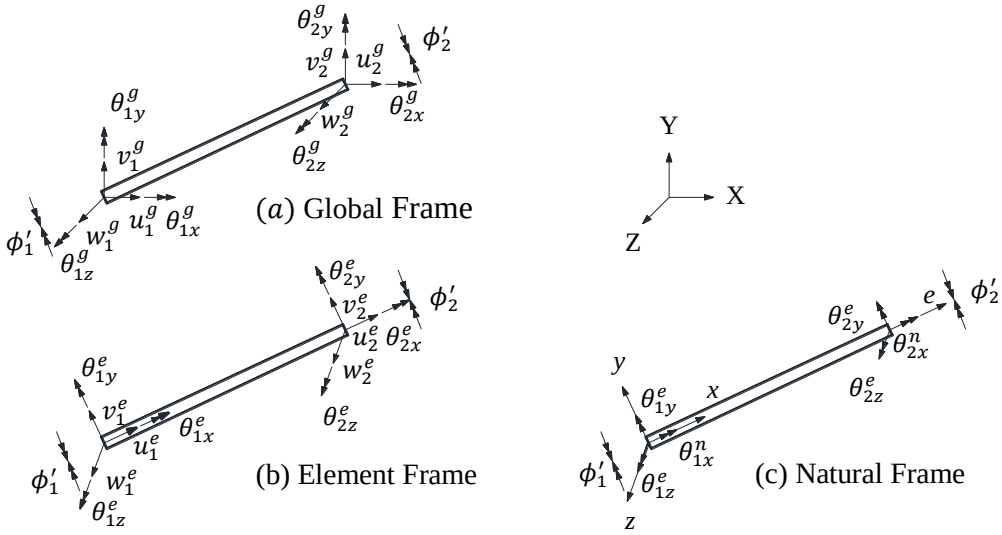

Figure 2.2 Element DOFs in Proposed Beam-Column Element

DOFs are seen in Figure 2.2. Throughout the discussion of this work, the DOF ordering for the natural frame is as follows:

$$\boldsymbol{q_n} = [\theta_{1x}^n \quad \theta_{1z}^n \quad \theta_{1y}^n \quad \phi_1' \quad \theta_{2x}^n \quad \theta_{2z}^n \quad \theta_{2y}^n \quad \phi_2' \quad e]^T \tag{2.1}$$

2.3 Uniaxial Green-Lagrange Strain and Torsional Shear Strain

Figure 2.3 shows a representation of an arbitrary cross-section with the centroid (C), shear center (S) of the cross-section, and location of an arbitrary reference axis (O) passing through the cross-section, where origin of the cross-sectional coordinates begin. Additionally, an arbitrary point, *P*, that coincides with a plate's (flange or web) mid-thickness with coordinates (*y*, *z*) is seen in the figure.

Typical beam-column derivations are more commonly seen to use either a cross-section's centroid or shear center as the nodal reference axis. To generalize and accommodate user preference, the proposed beam-column element was derived so that the reference axis may pass through any arbitrary point of a cross-section, a feature which is convenient for modeling MBFs. As a result, the reference axis may be defined through the mid-height of the web plate, for simplicity.

Formulation of the existing OpenSees beam-column element uses a uniaxial Green-Lagrange strain assumption (Chang 2006):

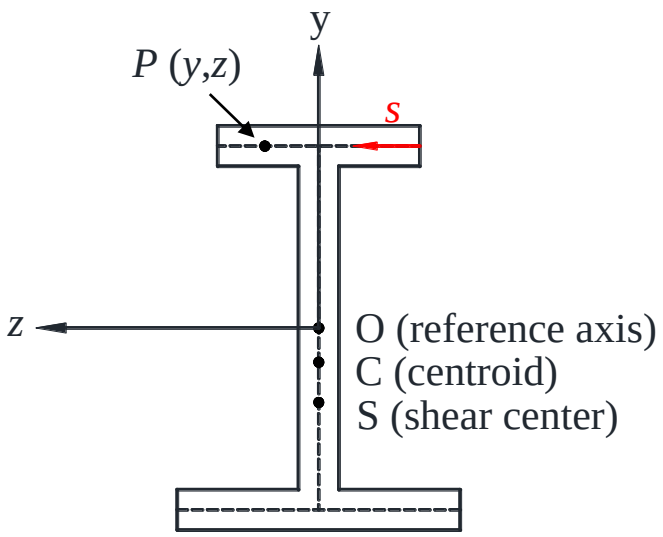

Figure 2.3 Coordinate System of a Singly-Symmetric I-Section

$$\varepsilon_x = u' + v'y' + w'z' + \frac{1}{2}(u'^2 + v'^2 + w'^2) \tag{2.2}$$

where *u* is the longitudinal displacement along the *x*-axis, *v* the transverse displacement in the *y*-axis, and *w* the transverse displacement in the *z*-axis of the arbitrary point *P*. The derivatives are with respect to *x*. Note that the second and third terms on the right-hand side of Eq. (2.2) account for the non-prismatic effect of the section for the web and flanges, respectively. The displacement components are obtained and elaborated through Ronagh (2000) as follows:

$$\begin{aligned} v &= v_0 - z\,sin\,\phi - y(1 - cos\,\phi) \\ w &= w_0 + y\,sin\,\phi - z(1 - cos\,\phi) \\ u &= u_0 - y\alpha_z - z\alpha_y - \omega\phi' \\ \alpha_y &= w_0'\,cos\,\phi - v_0'\,sin\,\phi \\ \alpha_z &= v_0'\,cos\,\phi + w_0'\,sin\,\phi \end{aligned} \tag{2.3}$$

where u_0 is the longitudinal displacement along the *x*-axis, v_0 the transverse displacement in the *y*-axis, and w_0 the transverse longitudinal displacement in the *z*-axis located at the reference axis of the cross-section. The cross-sectional twist, ϕ, is the counter-clockwise rotation relative to the *y*-axis about the shear center, and the warping function of the cross-section, ω, is defined by Ronagh (2000):

$$\omega(x, y, z) = \int_s \left(z_{,s}\,y - y_{,s}\,z\right)ds \tag{2.4}$$

where *s* is a coordinate tangent to the wall of the cross-section of each flange and web plate seen in Figure 2.3.

Taking the derivatives of *u*, *v*, and *w* in Eq. (2.3) and utilizing small angle theory (i.e., $\sin(\phi) \approx \phi$ and $\cos(\phi) \approx 1$), the displacements of a point *P* in Eq. (2.3) become:

$$\begin{aligned} u' &= u_0' - (y' - z'\phi - z\phi')v_0' - (y - z\phi)v_0'' - (y'\phi + y\phi' + z')w_0' \\ &\quad -(y\phi + z)w_0'' - \omega'\phi' - \omega\phi'' \\ v' &= v_0' - z'\phi - z\phi' \\ w' &= w'_0 + y'\phi + y\phi' \end{aligned} \tag{2.5}$$

Note that terms involving z' are kept for a general case of non-prismatic members consisting of both web-taper and flange-taper. Equivalent results are obtained through derivations done by Alemdar (2001) and Chang (2006), where the former is limited to prismatic members and the latter considers non-prismatic effects of both web-taper and flange-taper. Upon substituting Eq. (2.5) into Eq. (2.2), the expanded uniaxial Green-Lagrange strain equation becomes:

$$\begin{aligned} \varepsilon_x &= u_0' - (yv_0'' + zw_0'') - \omega\phi'' - (\omega' + y'z - z'y)\phi' + \frac{1}{2}(v_0'^2 + w_0'^2) \\ &\quad +(zv_0'' - yw_0'')\phi + \frac{1}{2}(y^2 + z^2)\phi'^2 \end{aligned} \tag{2.6}$$

Interpretation of the terms follow (Chang 2006):

u_0'	axial strain due to elongation at origin O,
$-(yv_0'' + zw_0'')$	axial strain due to bending about both axes,
$\omega\phi''$	axial strain due to warping,
$(\omega' + y'z - z'y)\phi'$	axial strain due to non-prismatic member effects with warping,
$\frac{1}{2}(v_0'^2 + w_0'^2)$	axial strain and bending coupling effects,

$(zv_0'' - yw_0'')\phi$ axial strain, combined bending, and torsional coupling effects, and

$\frac{1}{2}(y^2 + z^2)\phi'^2$ Wagner effect (coupling between axial strain and torsion).

This result shows that nonlinear second-order terms produces twisting and warping effects which are not seen when only linear terms of Eq. (2.6) are kept.

As a special case, neglecting the nonlinear terms in Eq. (2.6) results in a simplified version of the Green-Lagrage strain that solely considers axial strains due to elongation and bending about both axes:

$$\varepsilon_x = u_0' - yv_0'' - zw_0'' \tag{2.7}$$

This simplified form currently forms the basis for the existing beam-column element in OpenSees. As will be shown later, this simplified form lacks key attributes compared to the proposed element.

Although derivation of the proposed beam-column element neglects shear strains caused by bending and warping based on Vlasov's theory of thin-walled members, shear from the torsional effects of three-dimensional analyses and mechanics must still be accounted for. To consider this phenomenon, it is assumed that the shear strain due to torsional effects varies linearly throughout the thickness of the cross-section and that it has a zero value at the mid-thickness of a member's plate. Inclusion of this shear strain is treated separately from the axial strain and taken to be:

$$\gamma = -2\hat{r}\phi' \tag{2.8}$$

in which $\hat{r}$ represents the distance of a point measured normal to the mid-surface of a plate. The stress vector corresponding to the strain vector, $\boldsymbol{\varepsilon} = [\varepsilon_x \quad \gamma]^T$, is $\boldsymbol{\sigma} = [\sigma_x \quad \tau]^T$.

Taking the variation of both the uniaxial strain and shear strain in Eq. (2.6) and Eq. (2.8) yields:

$$\delta\varepsilon_x = \delta u_0' + v_0'\delta v_0' + w_0'\delta w_0' - y(\delta v_0'' + \phi\delta w_0'' + w_0''\delta\phi) + z(\phi\delta v_0'' - \delta w_0'' + v_0''\delta\phi) + (y^2 + z^2)\phi'\delta\phi' - \omega\delta\phi'' - (\omega' + y'z - z'y)\delta\phi' \quad (2.9)$$

$$\delta\gamma = -2\hat{r}\delta\phi' \quad (2.10)$$

where ψ is a warping effect due to a tapered web and tapered flanges:

$$\psi = \omega' + y'z - z'y \quad (2.11)$$

Combining the strain variations into vector form and corresponding relations from Eqs. (2.9) and (2.10) into matrix form yields:

$$\delta\boldsymbol{\varepsilon} = \begin{bmatrix}\delta\varepsilon_x \\ \delta\gamma\end{bmatrix} = \begin{bmatrix}1 & -y & z & (y^2+z^2) & -\omega & -\psi \\ 0 & 0 & 0 & 0 & 0 & -2\hat{r}\end{bmatrix} \begin{bmatrix}1 & v_0' & w_0' & 0 & 0 & 0 & 0 & 0 \\ 0 & 0 & 0 & 1 & \phi & w_0'' & 0 & 0 \\ 0 & 0 & 0 & \phi & -1 & v_0'' & 0 & 0 \\ 0 & 0 & 0 & 0 & 0 & 0 & \phi' & 0 \\ 0 & 0 & 0 & 0 & 0 & 0 & 0 & 1 \\ 0 & 0 & 0 & 0 & 0 & 0 & 1 & 0\end{bmatrix} \begin{bmatrix}\delta u_0' \\ \delta v_0' \\ \delta w_0' \\ \delta v_0'' \\ \delta w_0'' \\ \delta\phi \\ \delta\phi' \\ \delta\phi''\end{bmatrix}$$

or

$$\delta\boldsymbol{\varepsilon} = \mathbf{S}\cdot\mathbf{Q}\cdot\delta\mathbf{v} \quad (2.12)$$

2.4 Theoretical Element Tangent Stiffness Matrix

Previous researchers (e.g., Alemdar (2001), Chang (2006), Zhang et al. (2011), and many others) have shown that incorporating warping to the Green-Lagrange strain equation capture effects of LTB very well. Dependent on their research, various simplifications or generalizations were taken into account through their efforts in the expansion of the Green-Lagrange equation discussed in the previous section. Although the

axial strain equation derived in Eq. (2.6) is a generalized case for non-prismatic members consisting of web and flange taper, the focus of research work is on web-tapered members. Therefore, z' may be neglected and Eq. (2.6) becomes:

$$\varepsilon_x = u_0' - (yv_0'' + zw_0'') - \omega\phi'' - (\omega' + y'z)\phi' + \frac{1}{2}(v_0'^2 + w_0'^2) + (zv_0'' - yw_0'')\phi + \frac{1}{2}(y^2 + z^2)\phi'^2 \tag{2.13}$$

The University of Sydney, Australia has previously shown implementation of warping effects into OpenSees (Zhang et al. 2011). Although benchmark results with their element correlated well with published work and alternative finite element analysis (FEA) software, their formulation was for prismatic doubly-symmetric members only. However, the incorporations done by Zhang et al. (2011) served as a foundation for implementing the proposed element into OpenSees.

As mentioned in Section 2.2, the proposed element has a total of 9 DOFs in the natural reference frame. These deformations are due to the axial deformation as well as three local rotations and one warping rotation relative to the undeformed element at each end. Interpolation (shape) functions are used to assume the displacement fields along the *x*-axis by using a linear function for the axial displacement as well as cubic Hermitian functions for the transverse displacements and torsional angle, ϕ, relation:

$$\begin{aligned} u_0(x) &= \mathbf{N}_u^T \mathbf{q}_n \\ v_0(x) &= \mathbf{N}_v^T \mathbf{q}_n \\ w_0(x) &= \mathbf{N}_w^T \mathbf{q}_n \\ \phi(x) &= \mathbf{N}_\phi^T \mathbf{q}_n \end{aligned} \tag{2.14}$$

where $\boldsymbol{q}_n$ is the element displacement vector defined in Eq. (2.1) based on the natural reference frame. The interpolating functions are:

$$\begin{aligned}
\mathbf{N}_u^T &= [0 \quad 0 \quad 0 \quad 0 \quad 0 \quad 0 \quad 0 \quad 0 \quad N_u] \\
\mathbf{N}_v^T &= [0 \quad N_{v1} \quad 0 \quad 0 \quad 0 \quad N_{v2} \quad 0 \quad 0 \quad 0] \\
\mathbf{N}_w^T &= [0 \quad 0 \quad -N_{w1} \quad 0 \quad 0 \quad 0 \quad -N_{w2} \quad 0 \quad 0] \\
\mathbf{N}_\phi^T &= [N_{\phi 1} \quad 0 \quad 0 \quad N_{\phi 2} \quad N_{\phi 3} \quad 0 \quad 0 \quad N_{\phi 4} \quad 0]
\end{aligned} \tag{2.15}$$

where

$$N_u = \frac{x}{L} \tag{2.16}$$

$$N_{v1} = N_{w1} = N_{\phi 2} = x\left(1 - \frac{x}{L}\right)^2 \tag{2.17}$$

$$N_{v2} = N_{w2} = N_{\phi 4} = -x\left(\frac{x}{L}\right) + x\left(\frac{x}{L}\right)^2 \tag{2.18}$$

$$N_{\phi 1} = 1 - 3\left(\frac{x}{L}\right)^2 + 2\left(\frac{x}{L}\right)^3 \tag{2.19}$$

$$N_{\phi 3} = 3\left(\frac{x}{L}\right)^2 - 2\left(\frac{x}{L}\right)^3 \tag{2.20}$$

With the aid of Eq. (2.15), $\delta \boldsymbol{v}$ from Eq. (2.12) can be re-written as:

$$\delta \mathbf{v} = \mathbf{B} \delta \mathbf{q_n} \tag{2.21}$$

or

$$\begin{bmatrix} \delta u_0' \\ \delta v_0' \\ \delta w_0' \\ \delta v_0'' \\ \delta w_0'' \\ \delta\phi \\ \delta\phi' \\ \delta\phi'' \end{bmatrix} = \begin{bmatrix} 0 & 0 & 0 & 0 & 0 & 0 & 0 & 0 & N_u' \\ 0 & N_{v1}' & 0 & 0 & 0 & N_{v2}' & 0 & 0 & 0 \\ 0 & 0 & -N_{w1}' & 0 & 0 & 0 & -N_{w2}' & 0 & 0 \\ 0 & N_{v1}'' & 0 & 0 & 0 & N_{v2}'' & 0 & 0 & 0 \\ 0 & 0 & -N_{w1}'' & 0 & 0 & 0 & -N_{w2}'' & 0 & 0 \\ N_{\phi1} & 0 & 0 & N_{\phi2} & N_{\phi3} & 0 & 0 & N_{\phi4} & 0 \\ N_{\phi1}' & 0 & 0 & N_{\phi2}' & N_{\phi3}' & 0 & 0 & N_{\phi4}' & 0 \\ N_{\phi1}'' & 0 & 0 & N_{\phi2}'' & N_{\phi3}'' & 0 & 0 & N_{\phi4}'' & 0 \end{bmatrix} \begin{bmatrix} \delta\theta_{1x}^n \\ \delta\theta_{1z}^n \\ \delta\theta_{1y}^n \\ \delta\phi_1' \\ \delta\theta_{2x}^n \\ \delta\theta_{2z}^n \\ \delta\theta_{2y}^n \\ \delta\phi_2' \\ \delta e \end{bmatrix} \tag{2.22}$$

Therefore, Eq. (2.12) becomes:

$$\delta\boldsymbol{\varepsilon} = \mathbf{S} \cdot \mathbf{Q} \cdot \mathbf{B} \cdot \delta\mathbf{q_n} \tag{2.23}$$

The element tangent stiffness matrix of the proposed beam-column element can be obtained through the principle of virtual work:

$$\int_{V_0} (\delta\boldsymbol{\varepsilon}^{\mathrm{T}}\boldsymbol{\sigma})\,\mathrm{dV}_0 - \delta\mathbf{q}_{\mathrm{n}}{}^{\mathrm{T}}\mathbf{F}_{\mathrm{ext}} = 0 \tag{2.24}$$

where $\mathbf{F}_{ext}$ is an external force vector in the natural coordinate reference frame. Substituting Eq. (2.23) into Eq. (2.24), the following equation is obtained:

$$\delta\mathbf{q_n}^{\mathrm{T}}\left(\int_{V_0} (\mathbf{B}^{\mathrm{T}}\mathbf{Q}^{\mathrm{T}}\mathbf{S}^{\mathrm{T}}\boldsymbol{\sigma})\mathrm{dV}_0 - \mathbf{F}_{\mathrm{ext}}\right) = 0 \tag{2.25}$$

The first term inside the parentheses is the internal force vector based on the volume of an element, V_0, and cross-sectional area, A_0:

$$\mathbf{p} = \int_{V_0} (\mathbf{B}^{\mathrm{T}}\mathbf{Q}^{\mathrm{T}}\mathbf{S}^{\mathrm{T}}\boldsymbol{\sigma})\mathrm{dV}_0 = \int_0^L \left[\mathbf{B}^{\mathrm{T}}\mathbf{Q}^{\mathrm{T}} \int_{A_0} (\mathbf{S}^{\mathrm{T}}\boldsymbol{\sigma})\,\mathrm{d}A_0\right]\mathrm{dx} \tag{2.26}$$

where the section stress-resultant vector, $\mathbf{D} = [P \quad M_z \quad M_y \quad W \quad B \quad T_{sv}]^T$, is

$$\mathbf{D} = \int_{A_0} \mathbf{S}^{\mathrm{T}}\boldsymbol{\sigma}\,\mathrm{d}A_0 \tag{2.27}$$

And $\boldsymbol{\sigma} = [\sigma_x \quad \tau]^T$ is the section stress. Discussion of the section stress-resultant vector components will be presented in the following section.

Based on the constitutive relation between stress and strain, the variation of the stress can be directly related to the variation of the natural nodal displacements as follows:

$$\delta\boldsymbol{\sigma} = \mathbf{C}\delta\boldsymbol{\varepsilon} = \mathbf{C}\cdot\mathbf{S}\cdot\mathbf{Q}\cdot\mathbf{B}\cdot\delta\mathbf{q_n} \tag{2.28}$$

where $\boldsymbol{C}$ is a matrix consisting of the tangent Young's modulus, E_T, and the shear modulus, G, which is discussed in Section 2.5.

Therefore, taking the variation of Eq. (2.26) directly results into the formation of the element tangent local stiffness matrix as:

$$\begin{aligned}
\delta\mathbf{p} &= \delta\left[\int_0^L (\mathbf{B}^{\mathrm{T}}\mathbf{Q}^{\mathrm{T}}\mathbf{D})dx\right] \\
&= \int_0^L (\mathbf{B}^{\mathrm{T}}\delta\mathbf{Q}^{\mathrm{T}}\mathbf{D})dx + \int_0^L (\mathbf{B}^{\mathrm{T}}\mathbf{Q}^{\mathrm{T}}\delta\mathbf{D})dx \\
&= \int_0^L (\mathbf{B}^{\mathrm{T}}\delta\mathbf{Q}^{\mathrm{T}}\mathbf{D})dx + \int_0^L \left(\mathbf{B}^{\mathrm{T}}\mathbf{Q}^{\mathrm{T}}\int_{A_0}\mathbf{S}^{\mathrm{T}}\delta\boldsymbol{\sigma}\,\mathrm{d}A_0\right)dx \\
&= \int_0^L (\mathbf{B}^{\mathrm{T}}\mathbf{G}\mathbf{B})dx\;\delta\mathbf{q_n} + \int_0^L \left(\mathbf{B}^{\mathrm{T}}\mathbf{Q}^{\mathrm{T}}\int_{A_0}\mathbf{S}^{\mathrm{T}}\mathbf{C}\mathbf{S}\mathbf{Q}\mathbf{B}\mathrm{d}A_0\right)dx\;\delta\mathbf{q_n} \\
&= \left[\int_0^L (\mathbf{B}^{\mathrm{T}}\mathbf{G}\mathbf{B})dx + \int_0^L (\mathbf{B}^{\mathrm{T}}\mathbf{Q}^{\mathrm{T}}\mathbf{k_s}\mathbf{Q}\mathbf{B})dx\right]\delta\mathbf{q_n} \\
&= [\mathbf{K_G} + \mathbf{K_M}]\delta\mathbf{q_n} = \mathbf{K_{tan}}\;\delta\mathbf{q_n}
\end{aligned} \tag{2.29}$$

where the internal geometric stiffness matrix, $\mathbf{G}$, is obtained through:

$$\delta\mathbf{Q}^{\mathrm{T}}\mathbf{D} = \mathbf{G}\delta\mathbf{v} = \mathbf{G}\mathbf{B}\delta\mathbf{q_n} \tag{2.30}$$

In Eq. (2.29), $\mathbf{K}_{\boldsymbol{tan}}$ is the element tangent stiffness matrix in the natural reference frame, $\mathbf{k_s}$ is the section tangent stiffness matrix to be discussed in more detail in Section 2.5, and $\mathbf{G}$ is taken to be:

$$\mathbf{G} = \begin{bmatrix} 0 & 0 & 0 & 0 & 0 & 0 & 0 & 0 \\ 0 & P & 0 & 0 & 0 & 0 & 0 & 0 \\ 0 & 0 & P & 0 & 0 & 0 & 0 & 0 \\ 0 & 0 & 0 & 0 & 0 & M_y & 0 & 0 \\ 0 & 0 & 0 & 0 & 0 & M_z & 0 & 0 \\ 0 & 0 & 0 & M_y & M_z & 0 & 0 & 0 \\ 0 & 0 & 0 & 0 & 0 & 0 & W & 0 \\ 0 & 0 & 0 & 0 & 0 & 0 & 0 & 0 \end{bmatrix} \tag{2.31}$$

2.5 Theoretical Section Tangent Stiffness Matrix

The section stiffness matrix previously mentioned and described in Eq. (2.29) is:

$$\mathbf{k_s} = \int_{A_0} \mathbf{S^T C S}\, dA_0 \tag{2.32}$$

where $\boldsymbol{C}$ is a matrix that contains the constitutive relations of the tangent Young's modulus, E_T, and shear modulus, G, between the section stresses and section strains. This term takes the form of:

$$\mathbf{C} = \begin{bmatrix} E_T & 0 \\ 0 & G \end{bmatrix} \tag{2.33}$$

Substitution and manipulation of Eq. (2.32) yields the final form of the section tangent stiffness matrix:

$$\mathbf{k_s} = E_T \int_{A_0} \begin{bmatrix} 1 & & & & & \\ -y & y^2 & & & sym. & \\ z & -yz & z^2 & & & \\ \chi & -y\chi & z\chi & \chi^2 & & \\ -\omega & y\omega & -z\omega & -\chi\omega & \omega^2 & \\ -\psi & y\psi & -z\psi & -\chi\psi & \omega\psi & \psi^2 + 4G\hat{r}^2/E_T \end{bmatrix} dA_0 \tag{2.34}$$

where $\chi = y^2 + z^2$ and the terms ω (Eq. (2.4)) and ψ (Eq. (2.11)) are functions of warping and non-prismatic effects, respectively.

It is important to note that formulation of the section tangent stiffness matrix in Eq. (2.34) is a general result of an arbitrary longitudinal reference axis located on the cross-

section (see Figure 2.3). Simplification of the result can be obtained if the reference axis coincides with the cross-sectional shear center. Although having this configuration is convenient for members with doubly symmetric and prismatic geometry, use of a cross-section's shear center as the reference axis poses issues when dealing with non-prismatic and singly symmetric thin-walled members. For instance, a cross-section's shear center for such a member is not consistent along its length. Therefore, computational effort would be required to determine the shear center location of each integration point used throughout each element of a member. Due to the generalized result of the section stiffness matrix in Eq. (2.34), the reference frame can be conveniently placed at the cross-section's web plate mid-height. Through this, the extra effort of computing and determining each element's shear center at an integration point is unnecessary.

The section tangent stiffness matrix for the existing beam-column element model implemented in OpenSees only contains the first three rows and columns of Eq. (2.34):

$$\mathbf{k_s} = E_T \int_{A_0} \begin{bmatrix} 1 & & sym. \\ -y & y^2 & \\ z & -yz & z^2 \end{bmatrix} dA_0 \tag{2.35}$$

While the existing OpenSees implementation only takes into consideration bi-axial bending, the proposed element includes Wagner, warping, and non-prismatic effects. Wagner effects result in either an increase or decrease in torsional stiffness based on how the normal stress is acting on the cross-section. Further discussion of this effect is discussed in detail in Kitipornchai and Trahair (1975). Contributions of these Wagner effects are seen through the fourth row and column of Eq. (2.34), while warping contributions correspond with the fifth row and column, and non-prismatic member contributions correspond with the sixth row and column. Specifically, the variable ψ seen

in the sixth row and column denotes the non-prismatic consideration through warping effects due to a tapered web.

2.6 Discretization for Finite Element Implementation

As previously mentioned, the corresponding section stress-resultant vector from Eq. (2.27) is explicitly stated as (Chang 2006):

$$\mathbf{D} = \begin{bmatrix} \int_{A_0} \sigma_x \, dA_0 \\ \int_{A_0} -y\sigma_x \, dA_0 \\ \int_{A_0} z\sigma_x \, dA_0 \\ \int_{A_0} (y^2 + z^2)\, \sigma_x dA_0 \\ \int_{A_0} -\omega \, \sigma_x dA_0 \\ \int_{A_0} (-\psi\sigma_x + 4\hat{r}^2 G\phi')dA_0 \end{bmatrix} = \begin{bmatrix} P \\ M_z \\ M_y \\ W \\ B \\ T_{sv} \end{bmatrix} \tag{2.36}$$

where the terms of this vector are referred to as:

P = axial force,

M_z = bending moment about the z-axis,

M_y = bending moment about the y-axis,

W = Wagner force,

B = Bi-moment force about the y-axis, and

T_{sv} = St. Venant torsion.

Both the expressions for the section tangent stiffness matrix and section stress-resultant vector are based on the exact integral and analytical form. However, results in these forms are impractical for computer software implementation. Thus, each cross-

section must be discretized into a finite number of square fibers. By doing so, substitution of the integration in the analytical solution is achieved through summation of all the cross-sectional fibers. The discretized forms of the section tangent stiffness matrix and section stress-resultant vector are:

$$\mathbf{k_s} = \sum_{i=1}^{n} E_{Ti} A_i \begin{bmatrix} 1 & & & & & \\ -y_i & y_i^2 & & & sym. & \\ z_i & -y_i z_i & z_i^2 & & & \\ \chi_i & -y_i \chi_i & z_i \chi_i & {\chi_i}^2 & & \\ -\omega_i & y_i \omega_i & -z_i \omega_i & -\chi_i \omega_i & \omega_i^2 & \\ -\psi_i & y_i \psi_i & -z_i \psi_i & -\chi_i \psi_i & \omega_i \psi_i & \psi_i^2 + G\dfrac{t_{pi}^2}{E_{Ti}} \end{bmatrix} \tag{2.37}$$

$$\mathbf{D} = \sum_{i=1}^{n} A_i \begin{bmatrix} \sigma_i \\ -y_i \sigma_i \\ z_i \sigma_i \\ (y_i^2 + z_i^2)\sigma_i \\ -\omega_i \sigma_i \\ \left(-\psi_i \sigma_i - \dfrac{t_{pi} \tau_i}{3}\right) \end{bmatrix} \tag{2.38}$$

where n is the total number of fibers discretized throughout the cross-section.

Through the use of fiber discretization, individual fibers of a cross-section requires key attributes such that correct numerical solutions are computed. Thus, each fiber is required to have its own y_i and z_i coordinate, fiber area (A_i), tangent modulus (E_{ti}), stress value (σ_i), strain value (ε_i), and torsion coefficient (J_i). Because this research deals with thin-walled members, each plate is discretized through a single row of fibers as shown in Figure 2.4. Because the single layer of fibers, torsional effects being treated as linearly elastic, simplification of the torsional coefficient of each plate fiber, J_i, is taken to be:

$$J_i = \frac{b_{pi} t_{pi}^3}{3} = \frac{t_{pi}^4}{3} = \frac{t_{pi}^2 A_i^2}{3} \tag{2.39}$$

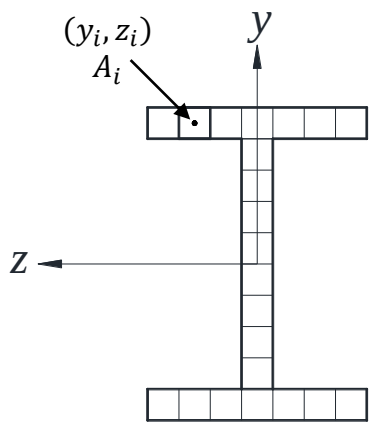

Figure 2.4 Fiber Discretization of Cross-Section

Each fiber is capable of possessing its own tangent modulus value. This is essential in cases where inelastic material models are used and especially important when residual stresses are considered and allows the non-uniform section yield patterns to occur throughout the flanges and web. Similarly, each fiber throughout a given cross-section also has a shear modulus value. But, because torsional shear strain is treated to remain consistently linear-elastic, this parameter, G, is taken to be constant throughout analysis.

Typically, coupling between normal stresses and shear stresses are needed to consider a yielding criterion of inelastic response. This would, therefore, require utilization of a stress resultant-based material model (e.g., Von Mises yield criterion) in order to satisfy such a criterion as done by Alemdar (2001). Although this routine is commonly seen through use of continua formulations, model simplification can also be achieved through a uniaxial approach.

Simplification of Eq. (2.37) is seen when dealing with cases pertaining specifically to prismatic members. All terms which correspond with ψ result to a zero value due to the constant web-height, resulting in a pure torsional stiffness in the last row and column of

the matrix. For a prismatic, linear-elastic, doubly-symmetric member is simplified and in the form of:

$$\mathbf{k_s} = \sum_{i=1}^{n} E_{ti} A_i \begin{bmatrix} 1 & & & & & sym. \\ 0 & y_i^2 & & & & \\ 0 & 0 & z_i^2 & & & \\ (y_i^2 + z_i^2) & 0 & 0 & (y_i^2 + z_i^2)^2 & & \\ 0 & 0 & 0 & 0 & \omega_i^2 & \\ 0 & 0 & 0 & 0 & 0 & \left(G\frac{t_{pi}^2}{E_{ti}}\right) \end{bmatrix} \tag{2.40}$$

2.7 Element Tangent Stiffness Matrix with Smoothing

The proposed beam-column element, as derived above, cannot exhibit inextensible bending, as described by Crisfield (1991). Within modeling of buckling analyses, many buckling modes are observed to nearly, if not completely, omit any form of axial extension (Belytschko 2000). Crisfield (1991) discussed this issue, stating that use of a linear function to represent axial deformations is insufficient when cubic functions are used to interpolate transverse displacements. He suggested the use of a quintic function to account for the axial components to omit cases of membrane locking. However, formulation of such a function can be long and cumbersome as it is pointed out by Chang (2006) and Alemdar (2001). Alternatively, Crisfield (1990) proposed an ad-hoc method in which smoothing incorporations of the axial strain may be used within the previously discussed formulation. Incorporation of the smoothing effects discussed in this section are used throughout the finite element implementation into OpenSees. The existing beam-column element currently implemented in OpenSees neglects the problem of inextensible bending.

Earlier equation derivations remain unaltered from the smoothing effects except the uniaxial Green-Lagrange strain seen in Eq. (2.6). After incorporation of smoothing effects, the new form of the strain equation becomes:

$$\varepsilon_x = u_0' - (yv_0'' + zw_0'') - \omega\phi'' - \psi\phi' + \frac{1}{60}\boldsymbol{\Theta}_n^T\mathbf{X}\boldsymbol{\Theta}_n + (zv_0'' - yw_0'')\phi + \frac{1}{2}(y^2 + z^2)\phi'^2 \tag{2.41}$$

where $\boldsymbol{\Theta}_n$ represents a vector containing the element nodal rotations in the natural reference frame defined through Eq. (2.1) and $\boldsymbol{X}$ is defined to be:

$$\mathbf{X} = \begin{bmatrix} 0 & 0 & 0 & 0 & 0 & 0 \\ 0 & 4 & 0 & 0 & -1 & 0 \\ 0 & 0 & 4 & 0 & 0 & -1 \\ 0 & 0 & 0 & 0 & 0 & 0 \\ 0 & -1 & 0 & 0 & 4 & 0 \\ 0 & 0 & -1 & 0 & 0 & 4 \end{bmatrix} \tag{2.42}$$

Thus, the variation of Eq. (2.41) is:

$$\delta\varepsilon_x = \delta u_0' + \frac{1}{30}\boldsymbol{\Theta}_n^T\mathbf{X}\delta\boldsymbol{\Theta}_n - y(\delta v_0'' + \phi\delta w_0'' + w_0''\delta\phi) + z(\phi\delta v_0'' - \delta w_0'' + v_0''\delta\phi) + (y^2 + z^2)\phi'\delta\phi' - \omega\delta\phi'' - \psi\delta\phi' \tag{2.43}$$

Therefore, the corresponding form of the **Q** matrix from Eq. (2.12) is:

$$\mathbf{Q} = \begin{bmatrix} 1 & \frac{1}{30}\boldsymbol{\Theta}_n^T\mathbf{X} & 0 & 0 & 0 & 0 & 0 & 0 \\ 0 & 0 & 0 & 1 & \phi & w_0'' & 0 & 0 \\ 0 & 0 & 0 & \phi & -1 & v_0'' & 0 & 0 \\ 0 & 0 & 0 & 0 & 0 & 0 & \phi' & 0 \\ 0 & 0 & 0 & 0 & 0 & 0 & 0 & 1 \\ 0 & 0 & 0 & 0 & 0 & 0 & 1 & 0 \end{bmatrix} \tag{2.44}$$

and the **B** matrix in Eq. (2.21) becomes:

$$\mathbf{B} = \begin{bmatrix} 0 & 0 & 0 & 0 & 0 & 0 & 0 & 0 & N_u' \\ 1 & 0 & 0 & 0 & 0 & 0 & 0 & 0 & 0 \\ 0 & 1 & 0 & 0 & 0 & 0 & 0 & 0 & 0 \\ 0 & 0 & 1 & 0 & 0 & 0 & 0 & 0 & 0 \\ 0 & 0 & 0 & 0 & 1 & 0 & 0 & 0 & 0 \\ 0 & 0 & 0 & 0 & 0 & 1 & 0 & 0 & 0 \\ 0 & 0 & 0 & 0 & 0 & 0 & 1 & 0 & 0 \\ 0 & N_{v1}'' & 0 & 0 & 0 & N_{v2}'' & 0 & 0 & 0 \\ 0 & 0 & -N_{w1}'' & 0 & 0 & 0 & -N_{w2}'' & 0 & 0 \\ N_{\phi 1} & 0 & 0 & N_{\phi 2} & N_{\phi 3} & 0 & 0 & N_{\phi 4} & 0 \\ N_{\phi 1}' & 0 & 0 & N_{\phi 2}' & N_{\phi 3}' & 0 & 0 & N_{\phi 4}' & 0 \\ N_{\phi 1}'' & 0 & 0 & N_{\phi 2}'' & N_{\phi 3}'' & 0 & 0 & N_{\phi 4}'' & 0 \end{bmatrix} \tag{2.45}$$

Subsequent procedures for the element formulation remain the same as the previous formulation from Eqs. (2.23) through (2.29). With smoothing effects, the geometric stiffness matrix, **G**, is updated to give the form:

$$\mathbf{G} = \begin{bmatrix} 0 & & & & & & & & & & & \\ 0 & 0 & & & & & & & & & & \\ 0 & 0 & \frac{4}{30}P & & & & & & & & & \\ 0 & 0 & 0 & \frac{4}{30}P & & & & & & & & \\ 0 & 0 & 0 & 0 & 0 & & & & & & & \\ 0 & 0 & -\frac{1}{30}P & 0 & 0 & \frac{4}{30}P & & & & & & \\ 0 & 0 & 0 & -\frac{1}{30}P & 0 & 0 & \frac{4}{30}P & & & & & \\ 0 & 0 & 0 & 0 & 0 & 0 & 0 & 0 & & & & \\ 0 & 0 & 0 & 0 & 0 & 0 & 0 & 0 & 0 & & & \\ 0 & 0 & 0 & 0 & 0 & 0 & 0 & M_y & M_z & 0 & & \\ 0 & 0 & 0 & 0 & 0 & 0 & 0 & 0 & 0 & 0 & W & \\ 0 & 0 & 0 & 0 & 0 & 0 & 0 & 0 & 0 & 0 & 0 & 0 \end{bmatrix} \quad sym. \tag{2.46}$$

3 OPENSEES IMPLEMENTATION AND INCORPORATION

3.1 General

OpenSees is an open source object oriented program which is commonly used by researchers and practicing engineers throughout the world (McKenna et al. 2000). Although its main goal is for numerical simulations of structural and geotechnical systems subjected to earthquakes, the software also offers other capability and functionality for various types of analysis. For instance, such applications involve non-seismic analyses including pseudo-static pushovers and modal analysis. Due to its open source nature, OpenSees continues to progress with new development as researchers contribute their own studies and work into the software through future packages.

With numerous utilities constantly being updated throughout its library, the functionality of OpenSees as an analysis tool shows great appeal and potential. Among the various element formulations that are accessible within the library, a category of beam-column elements can be found. In its current form, however, the existing beam-column element neglect consideration of non-uniform warping torsion and non-prismatic effects. Because thin-walled open section members are commonly used in metal building industry, the functionality and usability of adding a beam-column element which incorporates such warping effects, to capture cases of buckling, would be highly desirable.

3.2 Current OpenSees Framework

Foundation of the OpenSees framework relies on the concept of classes and objects. Objects can be thought of as a final product and representation of a certain entity. However, in order for that entity to be complete, certain aspects and variables which distinguish it

from any other type of entity must be defined. The need for these entity definitions result in the topic of a class, which is essentially a building block and blueprint for an object.

The purpose of a class is to capture characteristics of the object and its behavior. For example, an instance of an element can show the simplicity of the relations of objects and classes. A single element by itself would be considered to be the object. However, this generalization does not yield much meaning as it stands by itself. In order to distinguish what type of element is being referred to is based on the class which defines the element. A class for a truss element, for instance, will require attributes such as the element length, cross-sectional area, and modulus of elasticity.

Additionally, object oriented software utilizes the idea of modular programming. In essence, this technique allows the separation of various functions and tasks into different categories known as modules. A module can be thought of as a collection of functions which accomplish a certain purpose. As a result of this configuration, researchers and developers are able to incorporate and modify their studies without the need to understand the package as a whole.

Although each module in OpenSees is essential in ensuring proper finite element procedures, knowledge of how each module functions and interacts with one another is unnecessary. Because of this loose coupling of modules, researchers and developers are able to put emphasis and focus on incorporating their particular studies.

Within OpenSees, there are four main modules which are essential for any type of analysis being modeled: ModelBuilder, Domain, Analysis, and Recorder. Visualization of how these various modules are interlaced with one another is depicted through the tree diagram in Figure 3.1. The ModelBuilder module is responsible for handling and

processing necessary inputs of the finite element model which includes, but is not limited to, objects such as nodes, material models, and elements. The Domain and Analysis modules work together once a model is established. The Analysis module updates the model from a converged state to a new one. At the same time the Domain module updates and stores all necessary stresses and constitutive relations. As a model converges to a state of equilibrium, the Recorder module is then called to gather and save information from the Domain such that data post-processing can be done once the analysis is finished.

Among the various classes found within the Domain module, the Element class is of main focus when implementing a new element. Throughout this Element class, the existing beam-column element as well as other formulations are collected together for use in an analysis. Depiction of this hierarchy is shown in a tree diagram in Figure 3.2.

The beam-column element also relies on another object class which deals with the element's cross-sectional attributes and is referred to as FiberSection3d. Through the use of this class, a cross-sectional fiber's strain, stress, tangent modulus, and stiffness contribution can be determined.

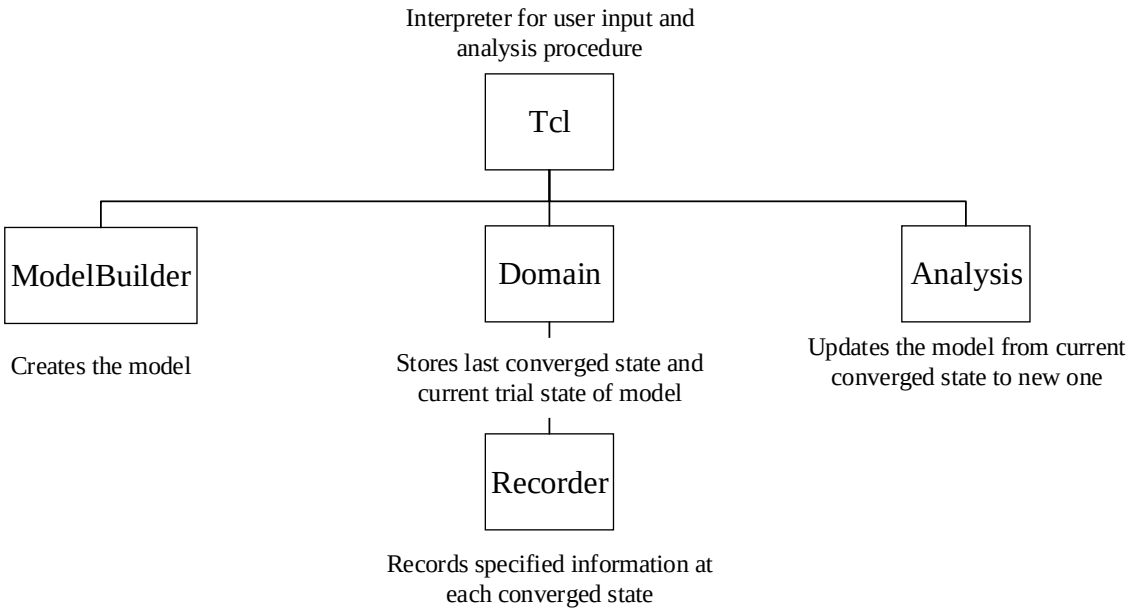

Figure 3.1 High Level Tree Diagram of OpenSees Modules (Fenves 2004)

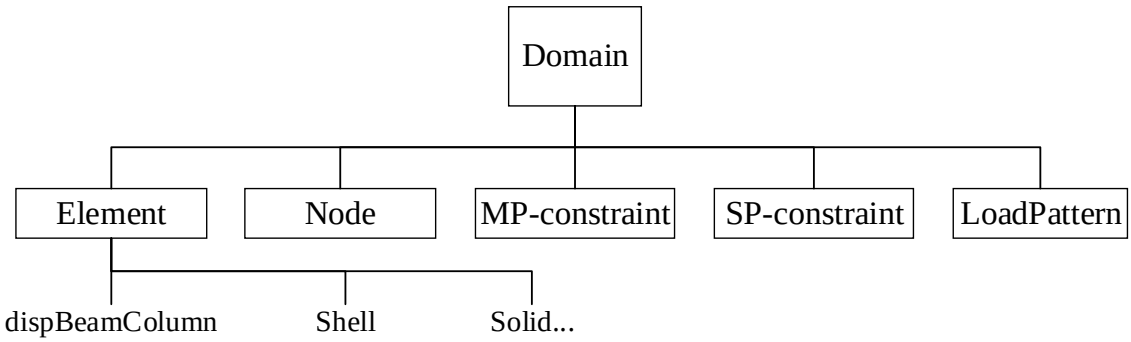

Figure 3.2 Tree Diagram of Domain Module in OpenSees (Fenves 2004)

3.3 Incorporation of Beam-Column Element With Warping Effects

Unlike commercial finite element software, OpenSees is limited in aspects of a graphical user interface (GUI) which allows a user to create a model. Instead, the string-based Tool Command Language (Tcl) acts as an interpreter for input files containing keywords, which are then read and processed by the ModelBuilder module of OpenSees.

Tcl has full scripting capability and can handle variable substitutions and manipulation. Because of this, configurations of large repetitive systems and convergence studies of a structure are easily managed and executed.

3.3.1 Framework Modification

Prior to the incorporation of the proposed beam-column element into OpenSees, adjustments to the Tcl interpreter were required. In a typical three-dimensional analysis consisting of conventional beam-column elements, nodal displacement is defined by six DOFs. Since warping was added as a seventh DOF in the proposed beam-column element, the interpreter was altered to allow the seventh DOF value within a three-dimensional analysis.

Due to the use of a single layer of fibers for each plate, formulation of the proposed element relies on plate thicknesses throughout the cross-sectional discretization process. Incorporation of additional keywords and parameters for plate thicknesses, shear modulus, and rate of web-taper was handled in a similar manner to accommodation of the extra DOF and will be described more in depth in the following sections.

3.3.2 Incorporating Tapered Element A into OpenSees Modification

The displacement-based beam-column element is a subclass of the Element class in OpenSees. The proposed displacement-based beam-column element will carry similar attributes and definitions as the existing implementation.

Within an analysis, strains and stresses are constantly updated to account for plasticity. The Element class and subclass FiberSection3D have to interact with one another so that necessary constitutive relations are updated and stored. A fiber's Young's

modulus is updated to take the tangent value of a stress-strain relation from the material model assigned by the user based on an updated fibers strain from the analysis. Once fiber stresses are updated, cross-sectional forces are computed at selected numerical integration points along the element's length. Numerical integration is performed using Gauss-Lobatto weights with a maximum of 10 integration points along the element.

The existing displacement-based beam-column element in OpenSees is formulated simply on linear strains. Because of this, axial strains are obtained solely based on elongation and bending. Consideration of torsional shear strain is based on uniform torsion and handled separately as mentioned in Section 2.3. Throughout the implementation of the proposed element, nonlinear terms of the Green-Lagrange strain are used to yield the strain in Eq. (2.6). These nonlinear second-order terms lead to the derivation of the updated element tangent stiffness matrix in Eq. (2.29).

In order to avoid overwriting the existing displacement-based beam-column element (dispBeamColumn3d), the Tapered Element A is defined under the class name TaperedDispBeamColumnSmoothing3d to denote the capability of web-taper effects as well as incorporation of the ad-hoc smoothing effects discussed in Section 2.7. Since the OpenSees library provides utilities for vector and matrix manipulation, computation of expressions similar to Eq. (2.29) can easily be performed.

3.3.3 Fiber Section Class Modification

To account for distributed plasticity of nonlinear material response, force-deformation responses of the cross-sections are required. From constitutive relations, internal section forces (or stress resultants) may be determined given the section's

corresponding deformations. The existing beam-column element implemented in OpenSees computes a section's uniaxial strain from:

$$\varepsilon_x = u_0' - yv_0'' - zw_0'' \tag{3.1}$$

Due to the simplicity of this equation, insufficient results for cases involving LTB will result. These insufficiencies arise because other terms in Eq. (2.6), which contribute to warping effects, are neglected.

As previously stated, the fiber discretization process (Figure 2.4) was used to evaluate the integration of a given cross-section. Since the main focus of the proposed beam-column element was on thin walled open section members, use of a single row of fibers for a given plate was judged to be sufficient. Each fiber's strain is computed and used to obtain the corresponding uniaxial stress and torsional stress.

In order to obtain the uniaxial strain and stress of a cross-section, certain attributes of the section level were defined. Since a section was discretized through finite amount of fibers, these fibers must contain information which will collectively hold true for the whole cross-section. Such attributes involved the fiber's area, coordinates, and material properties. Additionally, the cross-sectional parameters require an additional attribute which took into consideration a fiber's plate thickness.

Handling updates through the fiber discretization method and use of constitutive relations were processed within the class FiberSection3d. Similar to the alterations made to the dispBeamColumn3D class, the fiber class was also modified to accommodate a plate thickness, updated uniaxial strain equation, stress resultant vector, and section stiffness matrix. Therefore, a new class called TaperedFiberSection3D was incorporated to compliment the proposed displacement-based beam-column element.

4 CORRELATION STUDIES: MONOTONIC LOADING

4.1 General

In order to validate the beam-column element presented in Chapter 2 (Tapered Element A), numerous monotonic pushover analyses were modeled and compared to published results. These simulations involved varying parameters including web-taper, cross-sectional symmetry, boundary conditions, and material properties, both elastic and inelastic cases were included. Based on the results of these simulations, it was concluded that the buckling loads obtained from the use of the proposed beam-column element shows great promise for analysis of flexural and beam-column members involving lateral-torsional buckling.

4.2 Flexural Members with Elastic Lateral-Torsional Buckling

4.2.1 Member Imperfections

In any numerical modeling case involving buckling, instances of imperfections need to be incorporated to trigger a buckling effect. Although geometrical imperfections were not imposed in the following, alternative use of load imperfections were applied. With cases involving elastic buckling, a force-displacement plot yields a typical bifurcation figure. Bifurcation results show a constant increase in applied force up to the event where a critical load is reached. However, introduction of any type of imperfection applied to the model of a structure will induce a pure bifurcation result. Due to this, minimization of the imperfection is highly desirable in order to initiate buckling and at the same time preserve as much of a bifurcation trend as possible.

Alemdar's (2001) study of a simply supported prismatic beam consisted of a moment load imperfection which was applied at the roller boundary condition along the minor axis. This imperfection was established to be a hundredth of the moment magnitude applied about the major axis at the beam ends.

Unlike the Alemdar benchmark, Andrade's (2007) set of cases showed no implication of geometrical or load imperfections. Due to this, in this research the numerical modeling implemented in OpenSees for the following models were applied with a torsional load imperfection with magnitude of one thousandth of the applied member load. However, several cases showed that this load imperfection was insufficient. Therefore, for these particular instances, one hundredth of the applied load was used instead.

4.2.2 Alemdar (2001) Benchmark Configuration

Alemdar (2001) had several numerical examples which were used to validate his displacement-based element in the FEA framework of FE++. Among these examples, a simulation of LTB of a prismatic I-beam was performed. This benchmark problem helps in the verification of the validity of the OpenSees proposed element implementation for an elastic model. The cross-sectional dimensions are of a W10×100 beam with member length of 240 in. and is configured as a simply supported beam. The Young's modulus (E) was 29,000 ksi with a Poisson ration (v) of 0.3.

Configuration of the model problem is seen in Figure 4.1. As seen in the figure, all lateral displacements of the pin-end are restrained while the lateral displacements, except along the x-axis, is restrained of the roller-end. In addition to these boundary conditions, the twist about the x-axis is prevented at both ends. In order to study the behavior of how

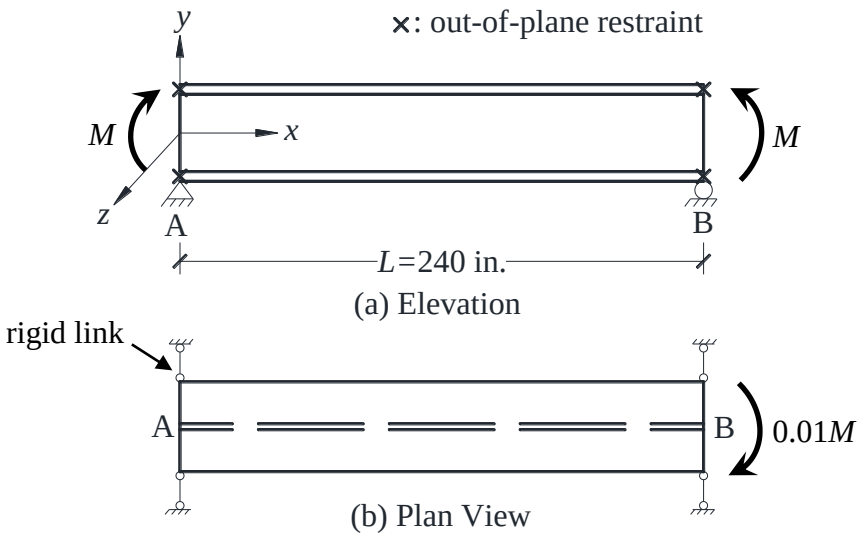

Figure 4.1 Simply Supported Prismatic Beam Model

warping affects overall critical buckling loads, both cases where warping is restrained and unrestrained were modeled using Tapered Element A.

The beam was loaded by concentrated moments about the major axis of the beam such that a uniform moment diagram is obtained. Additionally, a moment load imperfection about the minor axis of the roller end was applied with a hundredth magnitude to the applied moment about the major axis.

Modeling of the benchmark problem through OpenSees using Tapered Element A was easily achieved due to the prismatic geometry of the member. Origin of the *x*-axis coincided at the web mid-height of the pin boundary condition and continued along the member to the roller boundary condition. Cross-section discretization using fibers is similar to that shown in Figure 2.4 with a row of 20 fibers along the flange width and a row of 20 fibers along the web-height. Meshing of the member span using Tapered Element A consisted of 6 equal length beam-column elements from the pin-end to roller-end of the model. Both concentrated moments and the moment imperfection were simultaneously

applied to the OpenSees analysis using a total of 500 load control steps until a total concentrated moment of 25,000 kip-in at each member end was reached.

Closed-form solution of the critical moment for prismatic members under uniform moment is provided through AISC-360 Sect. F2.2 (AISC 2010a) of the user note as:

$$M_{cr} = \frac{\pi}{L_b}\sqrt{EI_yGJ + \left(\frac{\pi E}{L_b}\right)^2 I_y C_w} \tag{4.1}$$

However, application of Eq. (4.1) is strictly limited to situations where boundary conditions of the member ends allow warping to occur. An alternative and more general form of Eq. (4.1) is required when boundary conditions vary, such as restrained warping, at a member's ends (Chen and Lui 1987). This alternative equation for beams under uniform moment is:

$$M_{cr} = \left(\frac{\pi}{K_b L_b}\right)\sqrt{EI_yGJ\left(1 + \frac{\pi^2 E C_w}{(K_t L_b)^2 GJ}\right)} \tag{4.2}$$

where K_b is the effective length factor of the beam that corresponds to lateral bending, and K_t is the effective length factor of the beam that corresponds to twisting. The values for the factors K_b and K_t when warping is restrained at the beam ends are 0.883 and 0.492, respectively (Chen and Lui 1987). Analytical results of critical moments for the model problem when warping boundary conditions are varied are tabulated in Table 4.1.

Results of the force-displacement plots of the OpenSees analyses with warping unrestrained and warping restrained are seen in Figure 4.2 and Figure 4.3, respectively. Responses of both applied moment against in-plane rotation at the end and applied moment against midspan out-of-plane displacement are shown for both cases. Based on these results using Tapered Element A, it can be seen that buckling takes place relatively close to the calculated analytical solutions.

Table 4.1 Analytical Critical Moments of Model Problem

Warping Boundary Condition	M_{cr} (kip-in.)
Unrestrained	12,303
Restrained	17,316

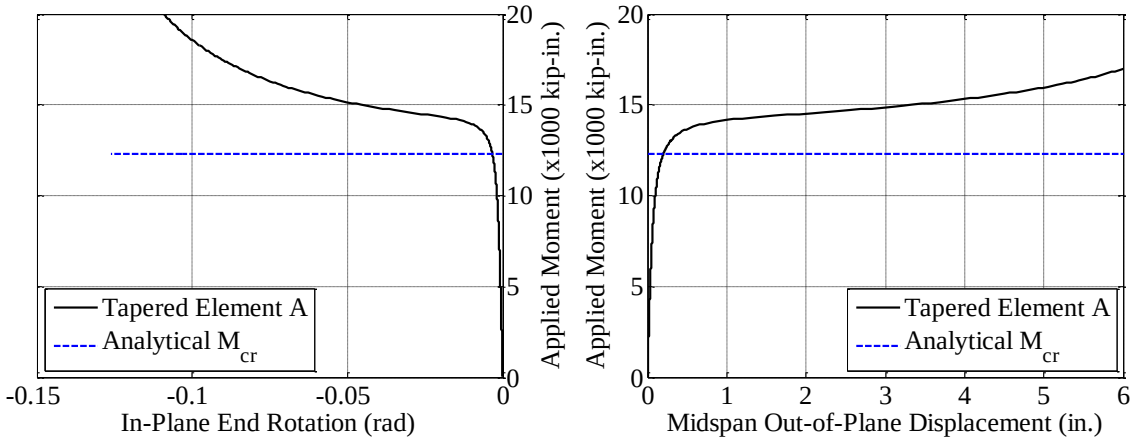

(a) In-Plane Response (b) Out-of-Plane Response

Figure 4.2 Lateral Buckling of W10×100 I-beam with Unrestrained Warping

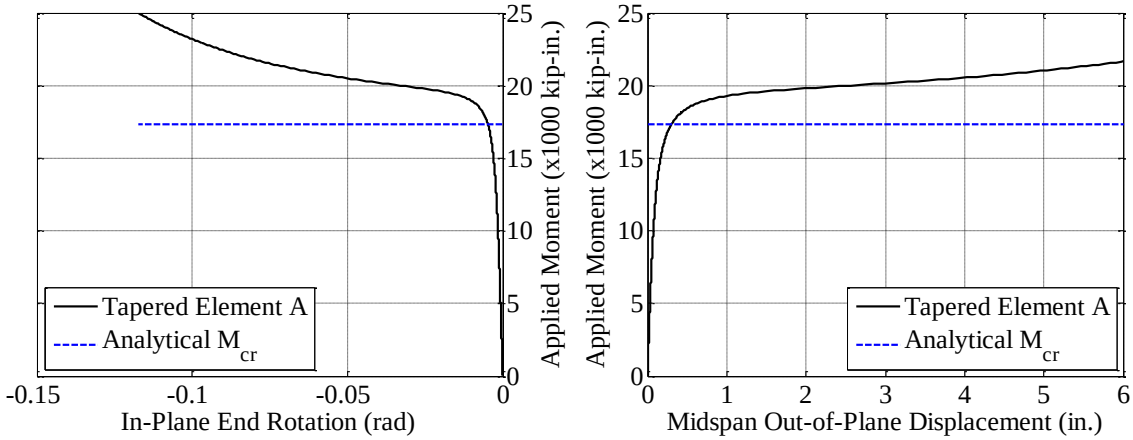

(a) In-Plane Response (b) Out-of-Plane Response

Figure 4.3 Lateral Buckling of W10×100 I-beam with Restrained Warping

4.2.3 Andrade et al. (2007) Benchmark Configurations

A significant amount of numerical modeling problems published by Andrade et al. (2007) focused on elastic buckling using FEA software, ABAQUS. These benchmark problems are seen in Figure 4.4 where the total set of test cases are broken into three subset categories. As seen from the figure, these benchmark cases consists of many variations of configurations and parameters. Because of this, Tapered Element A underwent thorough analyses and investigation which produced results that were comparable to those obtained with shell elements used by Andrade et al. in ABAQUS software. Modeling these problems through OpenSees consisted of element nodes passing through the mid-height of the member's cross-section as well as selected convergence studies of element meshing to ensure accurate solutions.

In order to ensure proper simulation of top flange and bottom flange loading, a rigid element was used to ensure correct load transfer from either the top or bottom flange to the mid-height of the cross section where an element node is located. Point loads which were loaded directly at the cross-sections mid-height required no use of such element as it could be applied directly to the node.

As seen in Figure 4.4, the configurations used throughout the benchmark problems consist of cantilever and simply supported boundary conditions. Although lateral bracings were not imposed on the cantilever simulations, the warping DOF at the fixed end was also restrained. In cases of simply supported beam simulations, lateral bracings as well as twist restraints were imposed at the beam ends but no restraints were imposed for warping. Due to member symmetry about the longitudinal axis, applying these constraints at the cross-sectional mid-height where the element nodes lay was sufficient.

Length variation for all the benchmark sets were analyzed in order to determine the versatility of Tapered Element A. Although it is rather difficult to determine analytical elastic buckling values of a non-prismatic member, results of OpenSees numerical modeling can be used to establish force-displacement relations which gives a relative idea of the load range when elastic buckling occurs. These results were compared to elastic buckling loads Andrade et al. determined using shell elements in ABAQUS. Thorough configuration and description of each member's modeling is detailed in subsequent sections for each of the three sets.

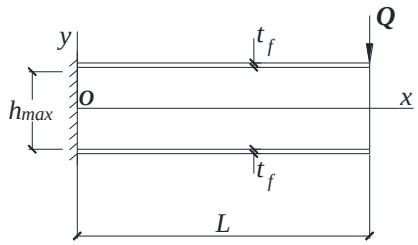

(1a)

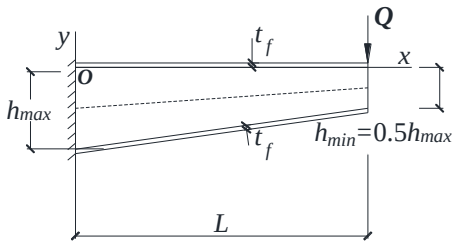

(1b)

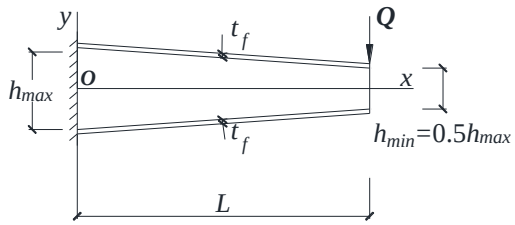

(1c)

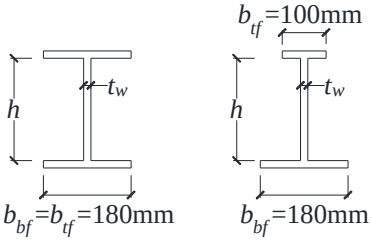

E=210 GPa

ν=0.3

h_{max}=600 mm

t_f=10 mm

t_w=8 mm

L=2.0 - 10.0 m

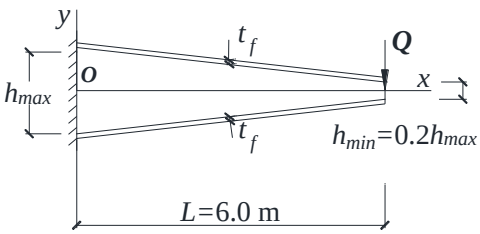

(2a)

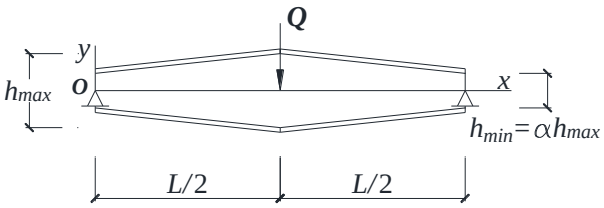

L=6.0 m; 9.0 m; 12.0 m α=1.0-0.4

(2b)

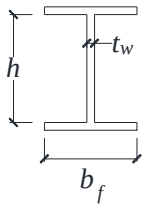

E=210 GPa ν=0.3

h_{max}=600 mm b_f=150 mm

t_f=10 mm t_w=8 mm

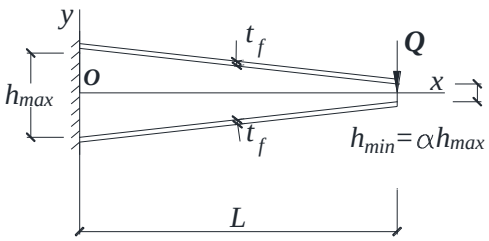

α=1.0; 0.5

(3a)

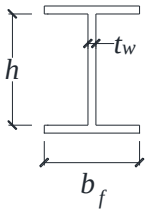

E=210 GPa

ν=0.3

h_{max}=300 mm

b_f=150 mm

t_f=10 mm

t_w=6 mm

L=4.0 - 8.0 m

Figure 4.4 Configurations and Material Properties (Andrade et al. 2007)

4.2.3.1 Set 1 Models and Results

The first set of models are depicted through Figure 4.4: (1a), (1b), and (1c). In addition to consistent material properties of $E = 210$ GPa and $\nu = 0.3$, variables of Set 1 which remained constant were:

- maximum web-height: $h_{max} = 600$ mm
- flange thickness: $t_f = 10$ mm
- web thickness: $t_w = 8$ mm
- loading location: top flange

Parameter variation for Set 1 involved:

- web-taper: prismatic, single web-taper, double web-taper
- member length: $L = 2.0 - 10.0$ m
- cross-section geometry:
  - doubly-symmetric: $b_{bf} = b_{tf} = 180$ mm
  - singly-symmetric: $b_{bf} = 180$ mm, $b_{tf} = 100$ mm

Numerical modeling of the configurations described for Set 1 involved fiber discretization, element meshing, and torsional load imperfections. Cross-section discretization using fibers is similar to that shown in Figure 2.4 with a row of 10 fibers along the flange width and a row of 20 fibers along the web-height. Each member modeled from Set 1 had a consistent element meshing using Tapered Element A of 10 elements along the member span. Load imperfections were imposed on the models such that members could numerically buckle under LTB. These load imperfections were imposed at the free end of the cantilevers with a torsional force magnitude of a thousandth of the

reported critical load obtained by Andrade et al. These load imperfections were applied to the members prior to beginning the analysis involving the transverse load.

Location of element nodes for the models of Set 1 coincide along a member's web mid-height throughout the member length. For cases such as (1a) and (1c), these nodal locations coincide along the *x*-axis due to the member geometry about this axis. Cases relating to (1b) required a shift of the *x*-axis to coincide with the top flange and web plate intersection due to the single web-taper of the member. Reference of node locations for these models were based off this new axis to the web's mid-height (depicted as the dashed lines in Figure 4.4 (1b)). Element meshing with Tapered Element A spanned from the fixed boundary condition to the free end using consistent element lengths throughout the member.

Models associated with Set 1 involved transverse loading applied at the top flange of a cantilever's free end. In order to simulate this type of loading in OpenSees, use of a rigid element is needed. The rigid element is connected from the node located at the free end to a node designated at the top flange directly vertical of the previously mentioned node.

Force-displacement plots corresponding to the results of both doubly symmetric sections and singly symmetric sections of models in case (1a) are seen in Figure 4.6 and Figure 4.7, respectively. Responses of these force-displacement plots are based off the end node of each cantilever beam's free end. Overall assessment of the models results suggest that Tapered Element A captures effects of critical buckling very well in both types of cross-sections with the exception where the member length of L = 2.0 m. Models corresponding with these member lengths are shown to be substantially stronger than those

reported by ABAQUS analysis of shell elements. Explanation of this high discrepancy is due to other effects of member buckling which is able to be captured with shell elements but not beam-column elements. Specifically, it was reported by Andrade that the governing failure mode of these shorter beams involve a localized buckling of the web due to the large h/L ratio (Andrade et al. 2007). Results associated with member lengths greater than 2.0 m showed to match very close to the critical load reported from shell models.

Force-displacement plots corresponding to the results of both doubly symmetric sections and singly symmetric sections of models in case (1b) are seen in Figure 4.8 and Figure 4.9, respectively. Responses of these force-displacement plots are based off the end node of each cantilever beam's free end. Similar to results seen from case (1a), models with member lengths $L \leq 4.0$ m showed to have a higher critical load to that obtained from the shell elements in ABAQUS. Although web buckling was not observed within the cases of shorter member lengths as it was in (1a), Andrade reported an increase of web distortion at the free end of the cantilever beam as the length decreased (Andrade et al. 2007). Prevention of web local buckling in these cases are most likely due to a 50% decrease in web height at the free end to that of models in (1.a).

Nodal displacement response of model (1b) with member length $L = 8.0$ m is seen in Figure 4.5. Figure 4.5 (a) shows the out-of-plane displacement response of the member at critical load as well as the undeformed state. The response seen in Figure 4.5 (b) gives the corresponding twists along the member at critical load. Response of the cross-sectional twist throughout the member span shows a clear representation of non-uniform torsion as the model experiences LTB. Although it is ideal to clearly see a three-dimensional buckled response of the cantilever beam after LTB, graphically rendering a 3-D model of the

member's buckled geometry is difficult with beam-column elements than it is with shell elements.

Force-displacement plots corresponding to the results of both doubly symmetric sections and singly symmetric sections of models in case (1c) are seen in Figure 4.10 and Figure 4.11, respectively. Responses of these force-displacement plots are based off the end node of each cantilever beam's free end. Similar conclusions for models of (1c) are made to those mentioned in models of case (1b). Although case (1c) models have the same decrease of web height at the member's free end by 50% like in case (1b), double web-taper spans along the member length of (1c). Effects of this model configuration resulted in a less substantial over-strength of critical load to the counterpart models of (1b).

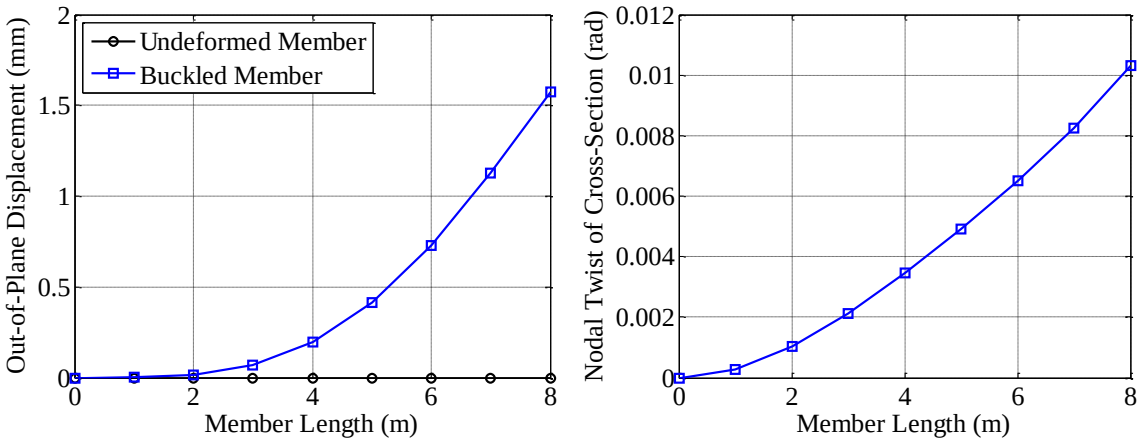

(a) Top View Profile of Model (b) Twist Response of Element Nodes

Figure 4.5 Case 1b Doubly Symmetric Deformations at Critical Load (L = 8.0 m)

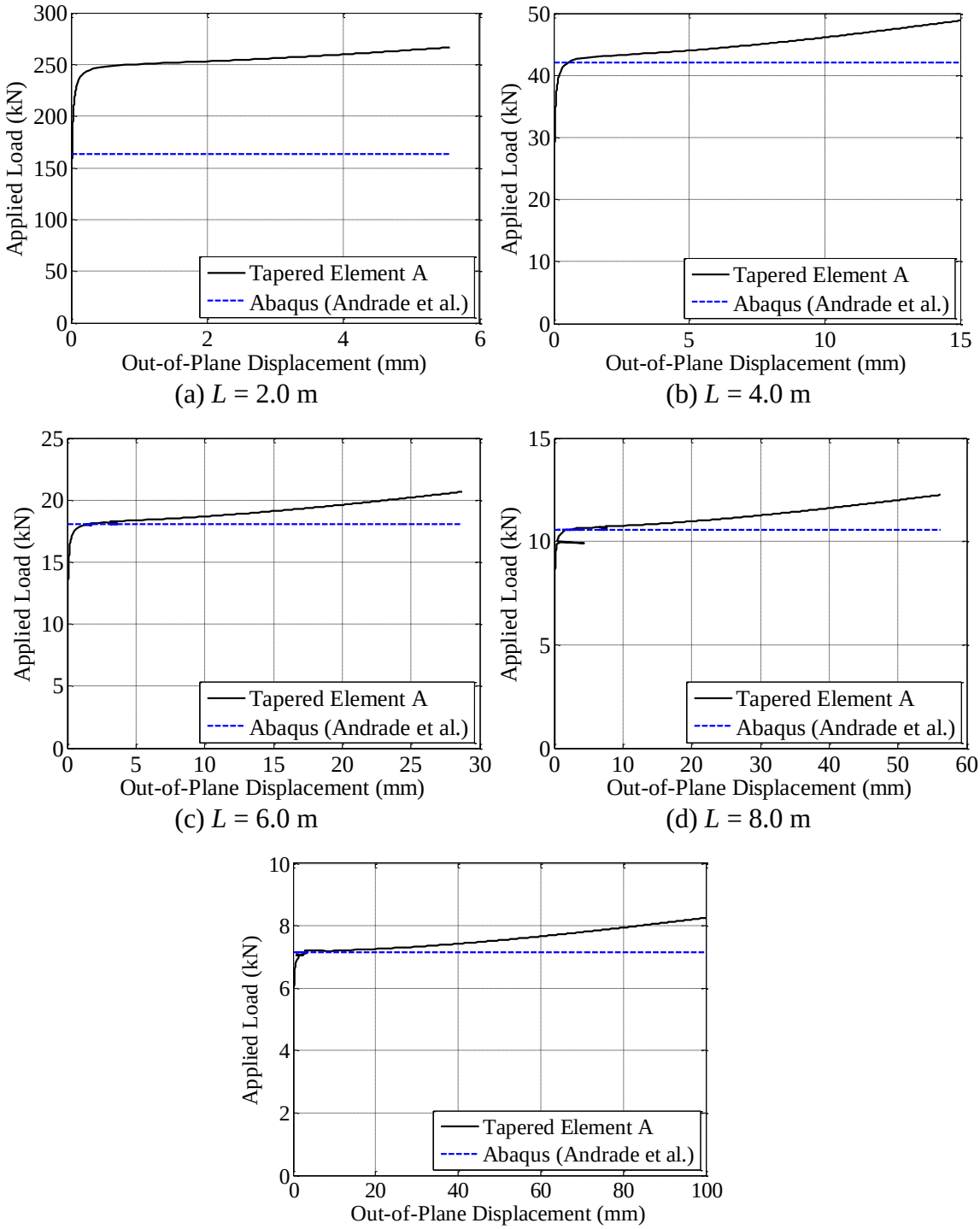

Figure 4.6 Set 1: Doubly Symmetric Prismatic Cantilever Beam

(See Figure 4.4 (1a))

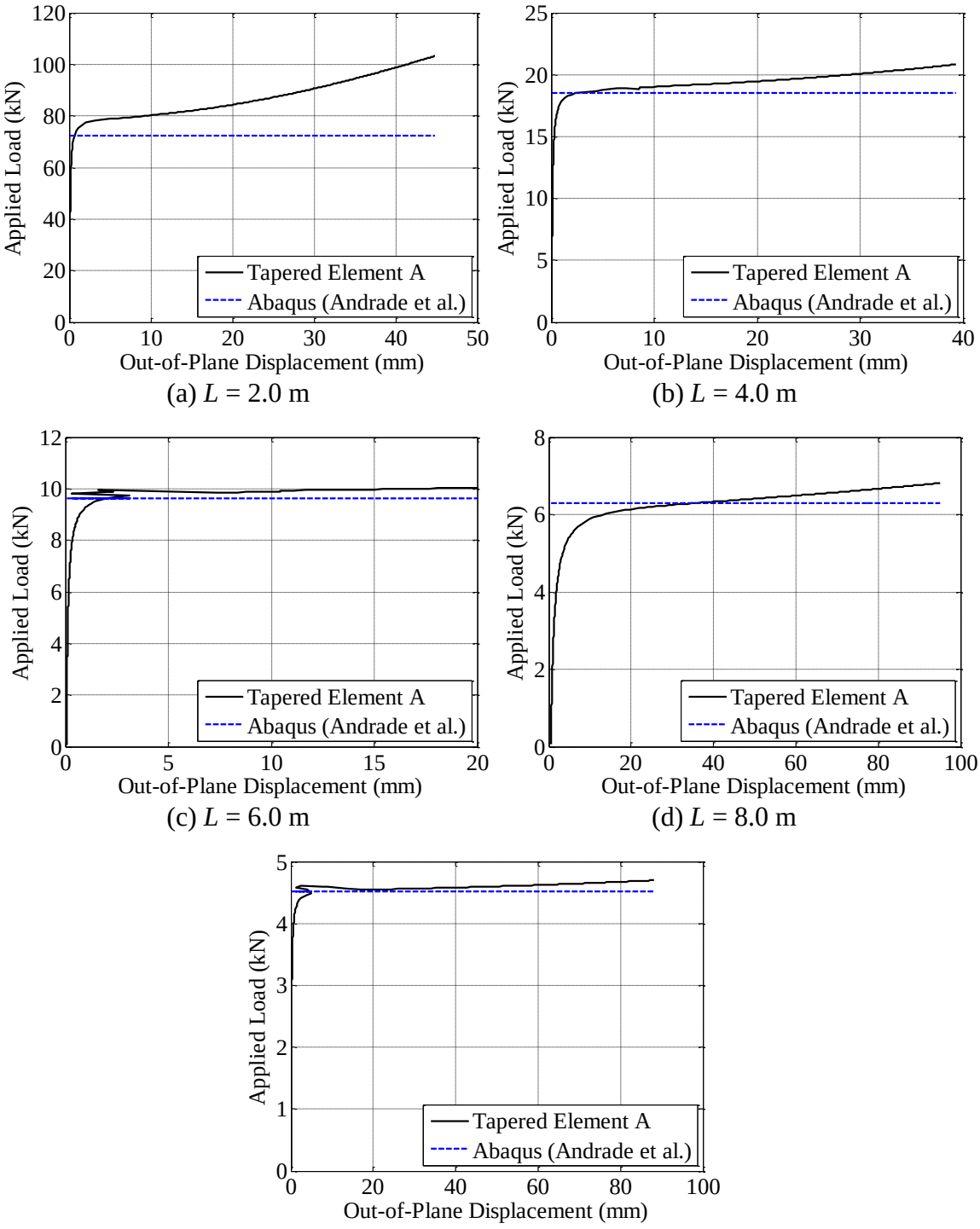

Figure 4.7 Set 1: Singly Symmetric Prismatic Cantilever Beam

(See Figure 4.4 (1a))

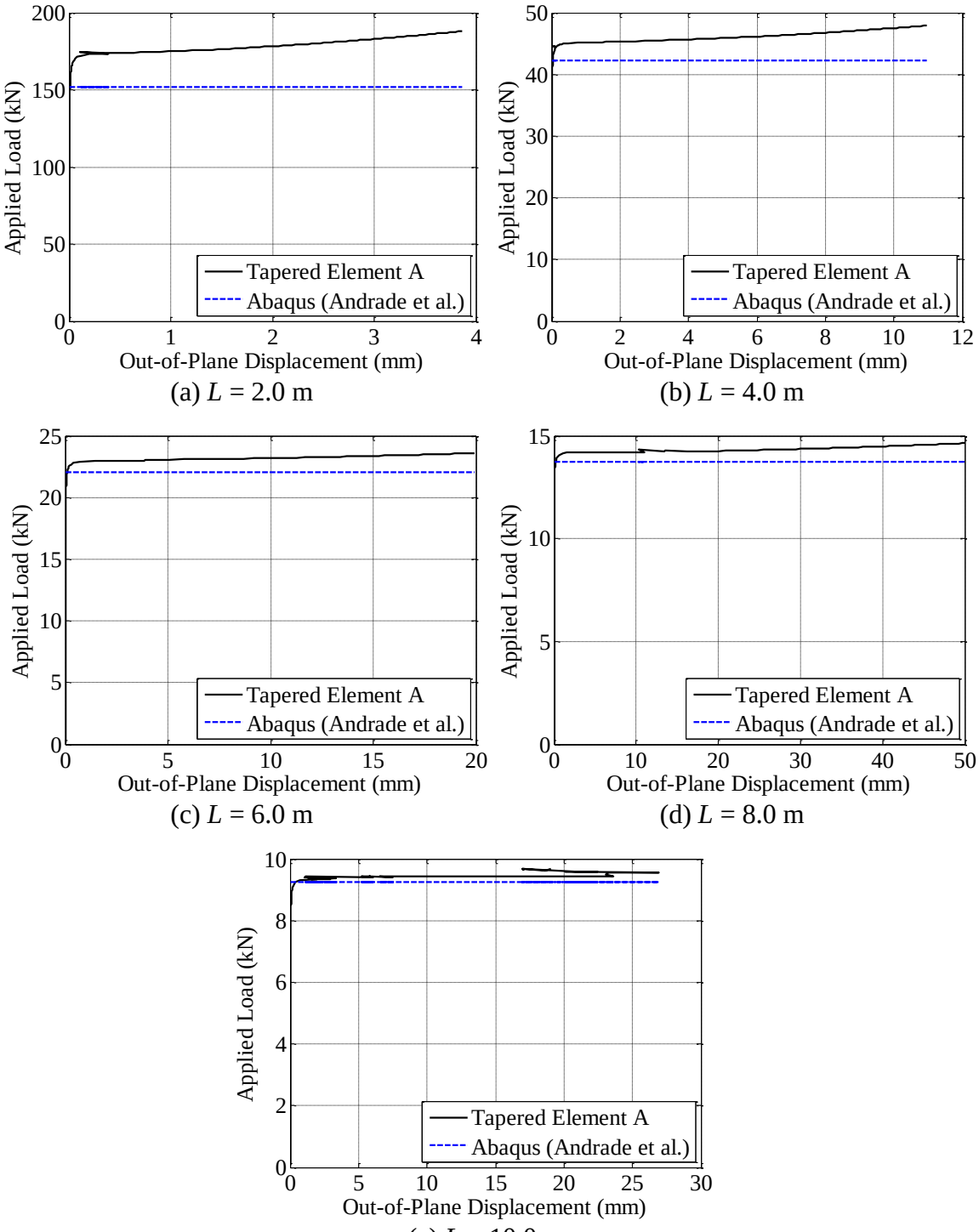

Figure 4.8 Set 1: Doubly Symmetric Single Web-Tapered Cantilever Beam

(See Figure 4.4 (1b))

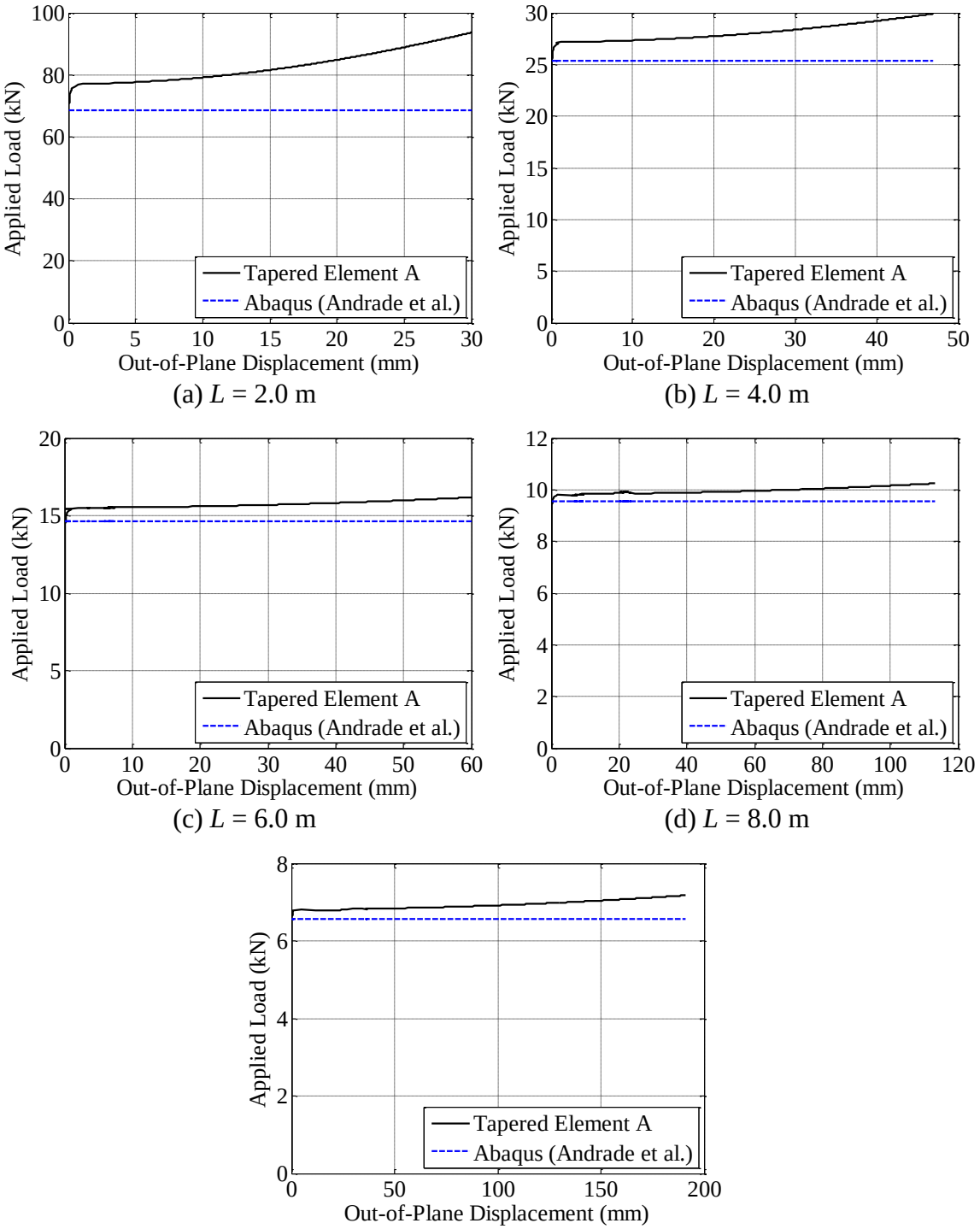

Figure 4.9 Set 1: Singly Symmetric Single Web-Tapered Cantilever Beam

(See Figure 4.4 (1b))

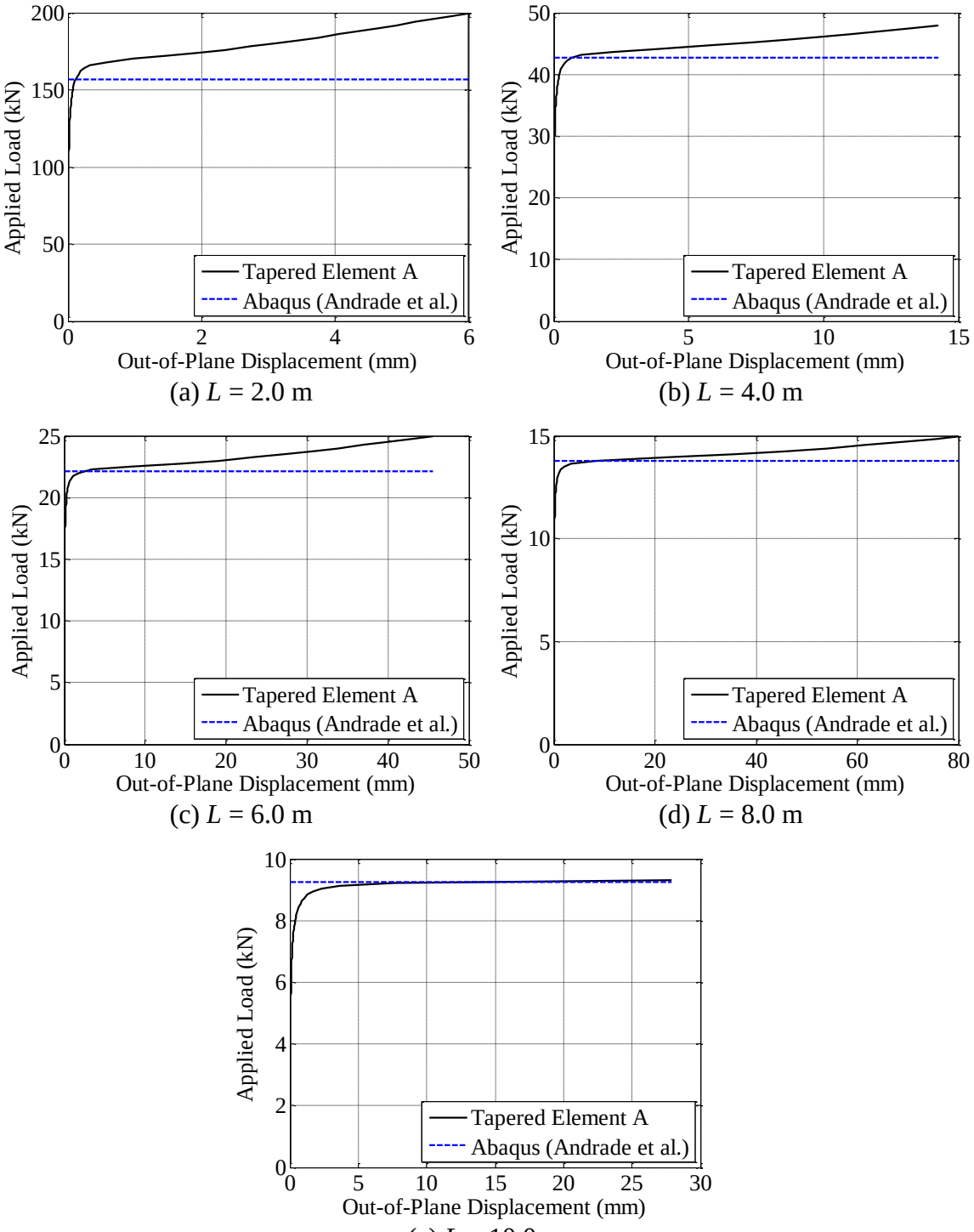

Figure 4.10 Set 1: Doubly Symmetric Double Web-Tapered Cantilever Beam

(See Figure 4.4 (1c))

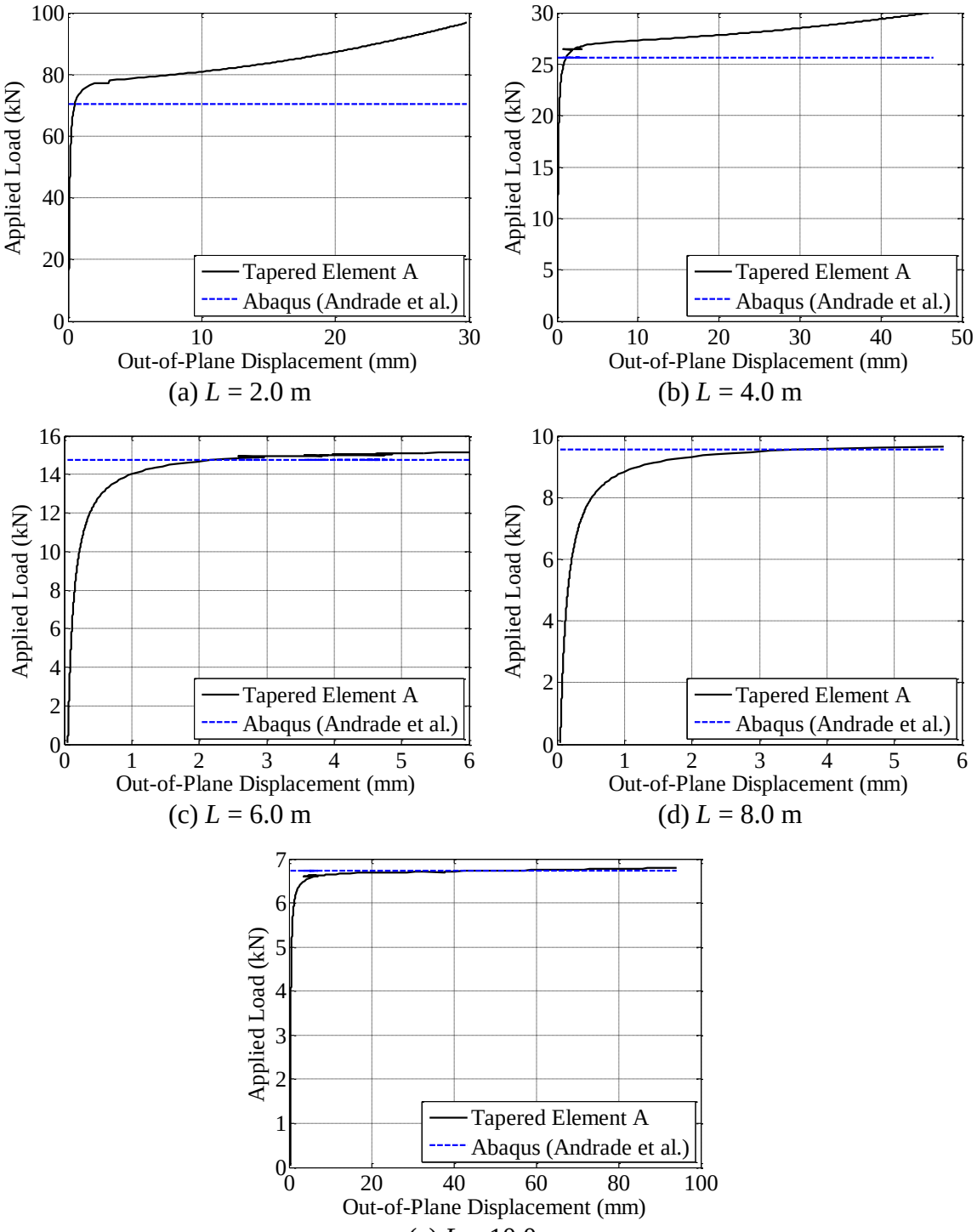

Figure 4.11 Set 1: Singly Symmetric Double Web-Tapered Cantilever Beam

(See Figure 4.4 (1c))

4.2.3.2 Set 2 Models and Results

The second set of models consist of cantilever members and simply supported members and are referred through Figure 4.4: (2a) and (2b). Models referred to (2a) involve cantilever members while models referred to Figure 4.4(2.b) involve models of simply supported beams. Both cases of (2a) and (2b) have consistent material properties of $E = 210$ GPa and $\nu = 0.3$ as well as constant variables of:

- maximum web-height: $h_{max} = 600$ mm
- flange thickness: $t_f = 10$ mm
- web thickness: $t_w = 8$ mm
- cross-section geometry: $b_{bf} = b_{tf} = 150$ mm

In addition to these variables, models of (2a) also have a fixed member length of $L = 6.0$ m and fixed web-taper such that $h_{min} = 0.2h_{max}$.

Parameter variation of models of Set 2 are as follow:

- (2a) models:
  - loading location: top flange, web mid-height, bottom flange
- (2b) models:
  - member length: $L = 6.0$ m, 9.0 m, 12.0 m
  - web-taper from midspan to B.C.: $h_{min} = \alpha h_{max}$ where $\alpha = 1.0 - 0.4$
  - loading location: top flange, web mid-height

Numerical modeling of the configurations described for Set 2 involved fiber discretization, element meshing, and torsional load imperfections. Cross-section discretization using fibers is similar to that shown in Figure 2.4 with a row of 10 fibers

along the flange width and a row of 20 fibers along the web-height. Each member modeled from Set 2 had a consistent element meshing using Tapered Element A of 10 elements along the member span. Load imperfections were imposed on the models such that members could numerically buckle under LTB. These load imperfections were imposed at the free end of the cantilevers and at the midspan of the simply supported beams with a torsional force magnitude of a thousandth of the reported critical load obtained by Andrade et al. These load imperfections were applied to the members prior to beginning the analysis involving the transverse load.

Location of element nodes for the models of Set 2 coincide along a member's web mid-height throughout the member length. Due to member symmetry about the *x*-axis, node locations for models relating to (2a) and (2b) coincide directly along the *x*-axis. Element meshing with Tapered Element A spanned from the fixed boundary condition to the free end using consistent element lengths throughout the member.

Models associated with Set 2 involved transverse loading applied at either the top flange, web mid-height, or bottom flange dependent of the case being modeled. Unlike top flange or bottom flange loading, transverse loads being applied at the web mid-height can be directly applied to the element end node of the free end of a cantilever or midspan of a simply supported beam. In order to simulate top flange or bottom flange loading, use of a rigid element is needed. For cases of (2a), the rigid element is connected from the node located at the free end to a node designated at either the top flange or bottom flange directly vertical of the previously mentioned node. Application of a rigid element to the simply supported beams of (2b) require a similar method to that mentioned of (2a) except the top flange node is located directly vertical to the node at the midspan of the member.

Force-displacement plots corresponding to the results of models in case (2a) are seen in Figure 4.13. Responses of these force-displacement plots are based off the end node of each cantilever beam's free end. Models of case (2a) involved a very sharp web-taper which involved a 80% web height decrease at the free end with respect to the fixed end's web height. The overall force-displacement responses of transverse loading applied at the top flange, mid-height of the web, and bottom flange show a very nice correlation to the ABAQUS critical load using shell elements. Conclusions made from the results of (2a) show great promise for Tapered Element A in use of models involving any rate of web-taper.

Nodal displacement response of model (2a) with mid-height loading is seen in Figure 4.12. Figure 4.12(a) shows the out-of-plane displacement response of the member at critical load as well as the undeformed state. The response seen in Figure 4.12(b) gives the corresponding twists along the member at critical load. Response of the cross-sectional twist along the member span shows clear non-uniform torsion as the model undergoes LTB.

Force-displacement plots corresponding to the results of models in case (2b) are seen in Figure 4.14 through Figure 4.17. Responses of these force-displacement plots are based off the midspan node of each simply supported beam. Overall responses of the force-displacement plots for models of case (2b) show to yield similar critical loads to the FEA analysis using shell elements. It is seen that responses for both mid-height loading and top flange loading for the prismatic beams show the least deviation of critical loads compared to the counterparts involving web-taper from the midspan to the pin and roller boundary

conditions. As the taper ratio, α, is decreased, results obtained from Tapered Element A generally show a lower critical load to the shell FEA counterpart.

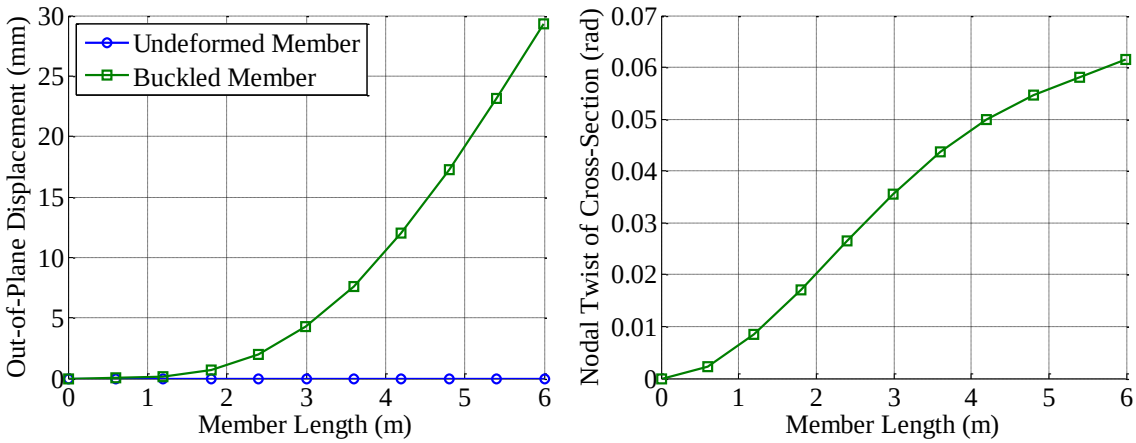

(a) Top View Profile of Model (b) Twist Response of Element Nodes

Figure 4.12 Case 2a Member Deformations at Critical Load (Mid-Height Loading)

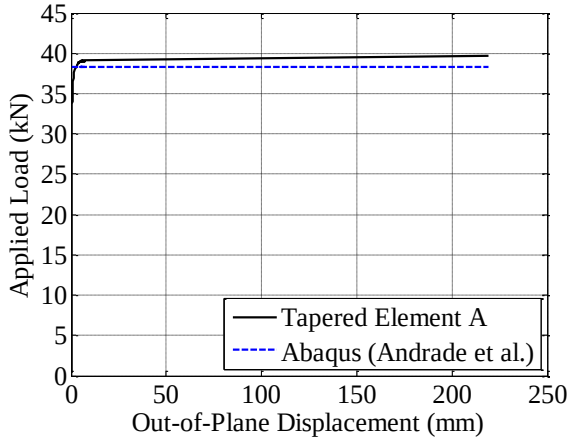

(a) Top Flange Loading

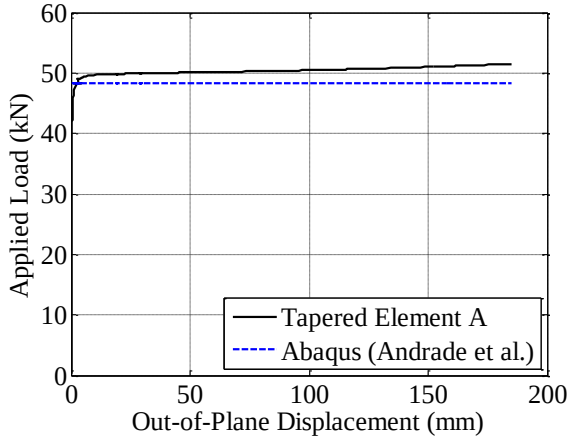

(b) Bottom Flange Loading

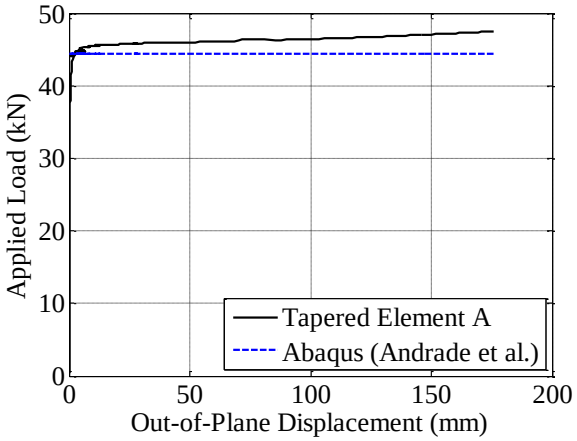

(c) Mid-Height Loading

Figure 4.13 Set 2: Double Web-Tapered Cantilever Beam (*L* = 6.0 m)

(See Figure 4.4 (2a))

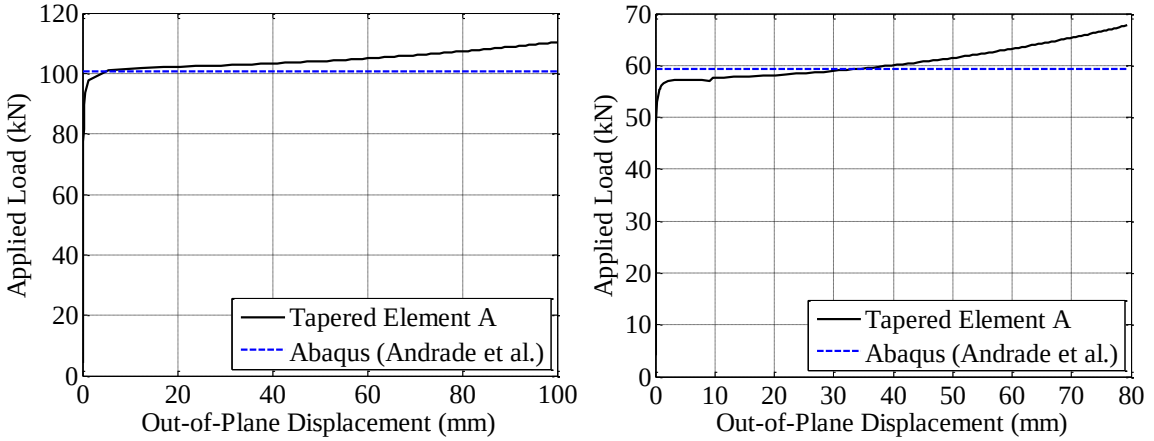

(a) L = 6.0 m, Mid-Height Loading (b) L = 6.0 m, Top Flange Loading

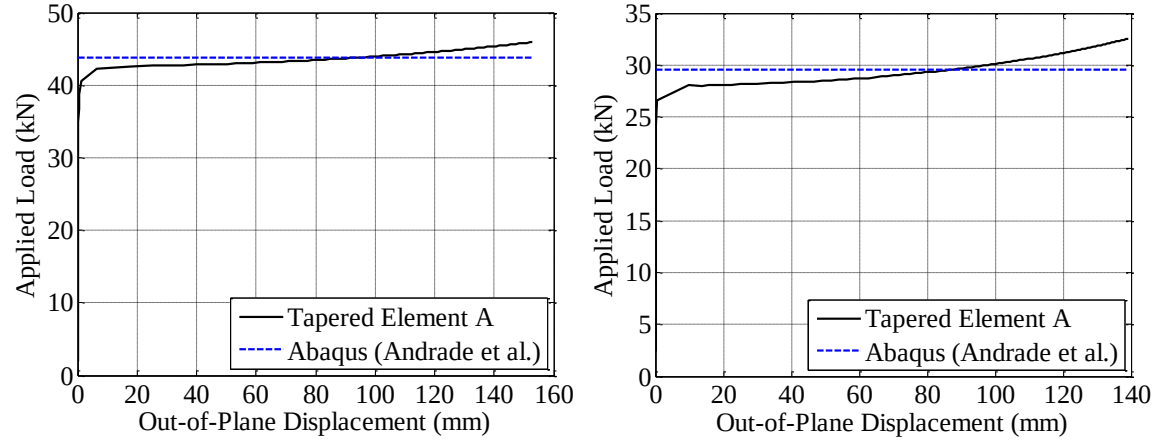

(c) L = 9.0 m, Mid-Height Loading (d) L = 9.0 m, Top Flange Loading

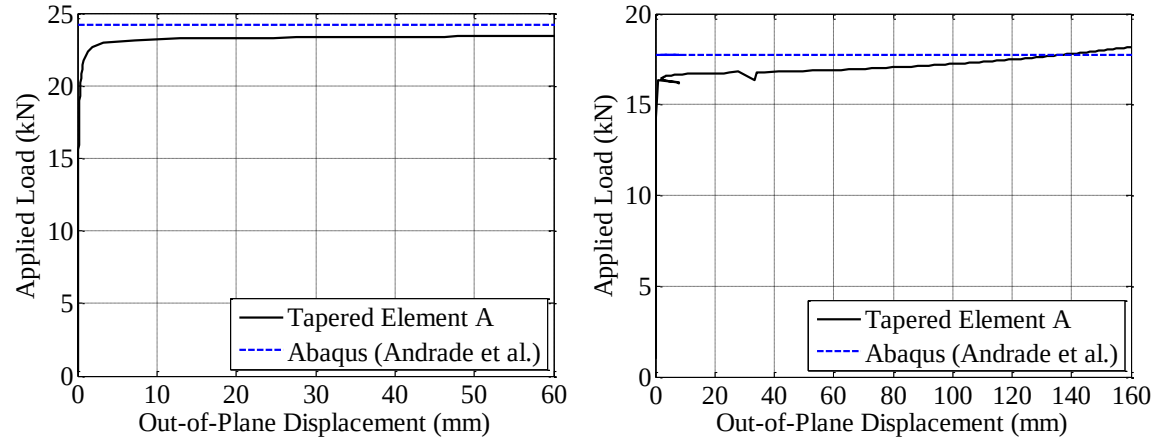

(e) L = 12.0 m, Mid-Height Loading (f) L = 12.0 m, Top Flange Loading

Figure 4.14 Set 2: Simply Supported Double Web-Tapered Beam (α = 0.4)

(See Figure 4.4 (2b))

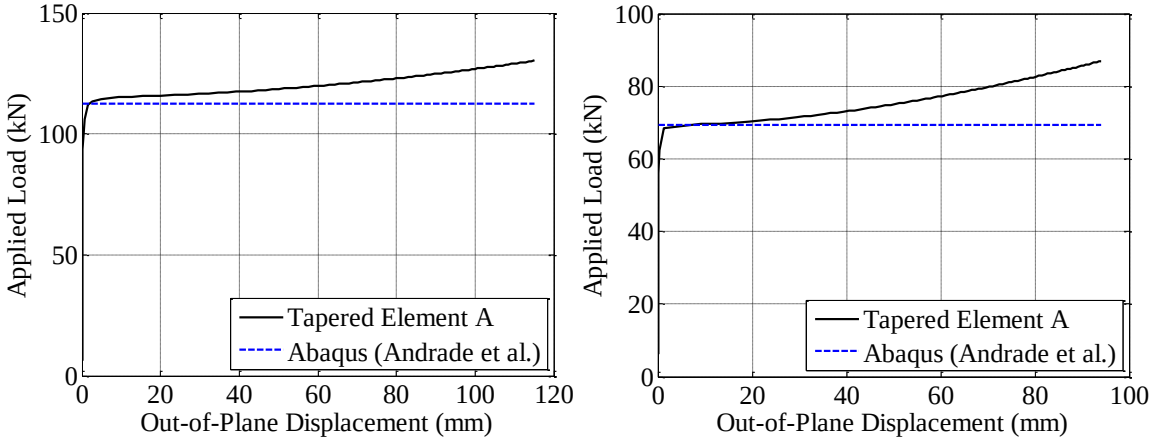

(a) L = 6.0 m, Mid-Height Loading (b) L = 6.0 m, Top Flange Loading

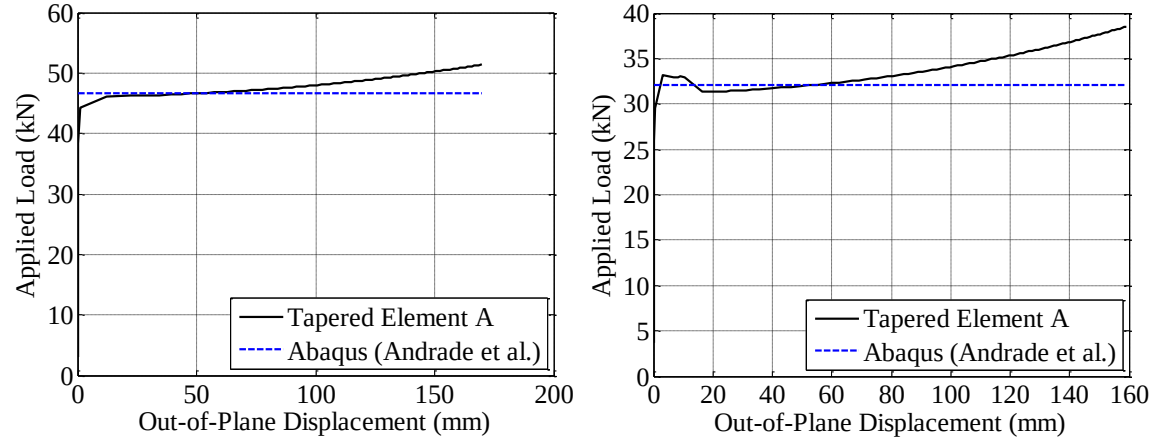

(c) L = 9.0 m, Mid-Height Loading (d) L = 9.0 m, Top Flange Loading

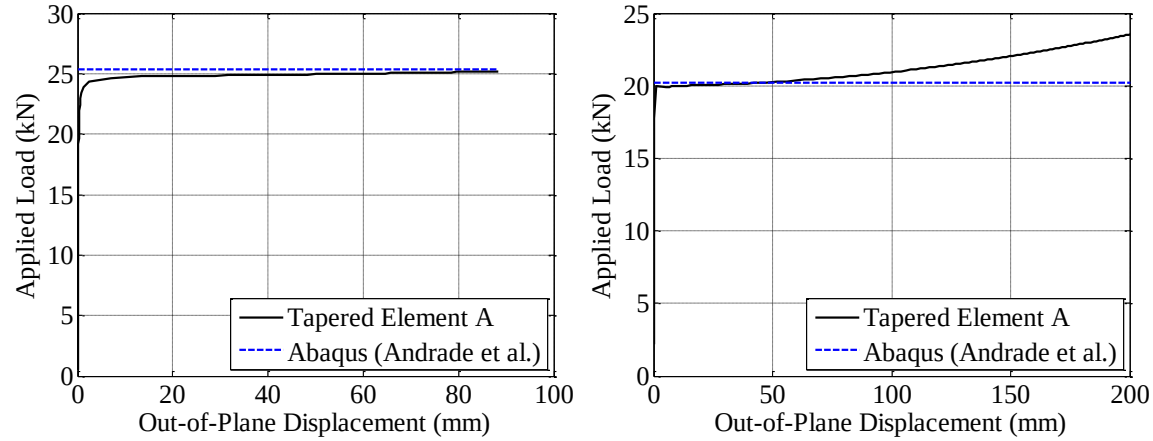

(e) L = 12.0 m, Mid-Height Loading (f) L = 12.0 m, Top Flange Loading

Figure 4.15 Set 2: Simply Supported Double Web-Tapered Beam (α = 0.6)

(See Figure 4.4 (2b))

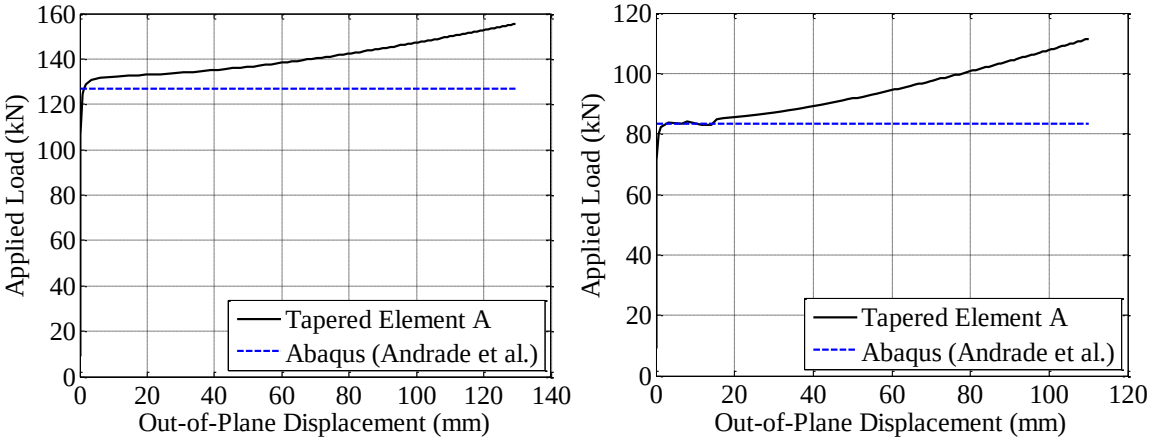

(a) L = 6.0 m, Mid-Height Loading (b) L = 6.0 m, Top Flange Loading

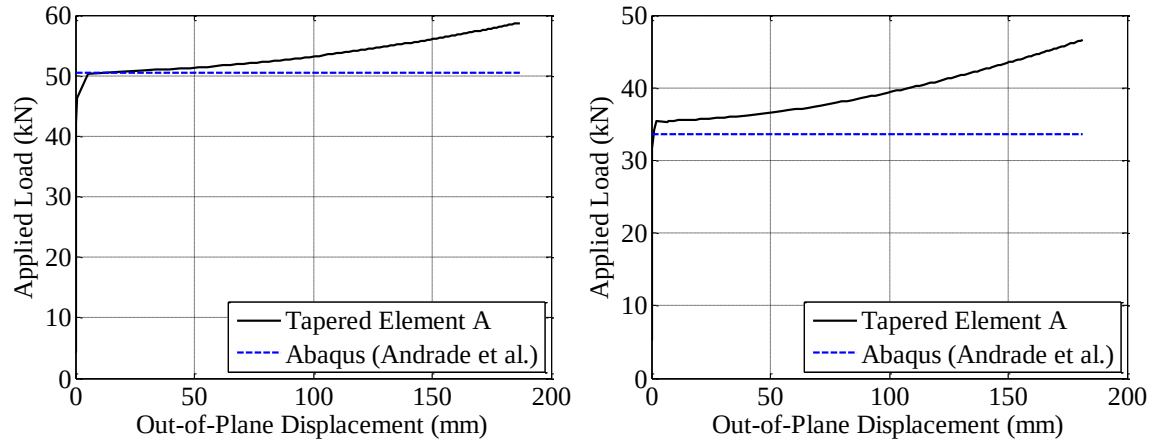

(c) L = 9.0 m, Mid-Height Loading (d) L = 9.0 m, Top Flange Loading

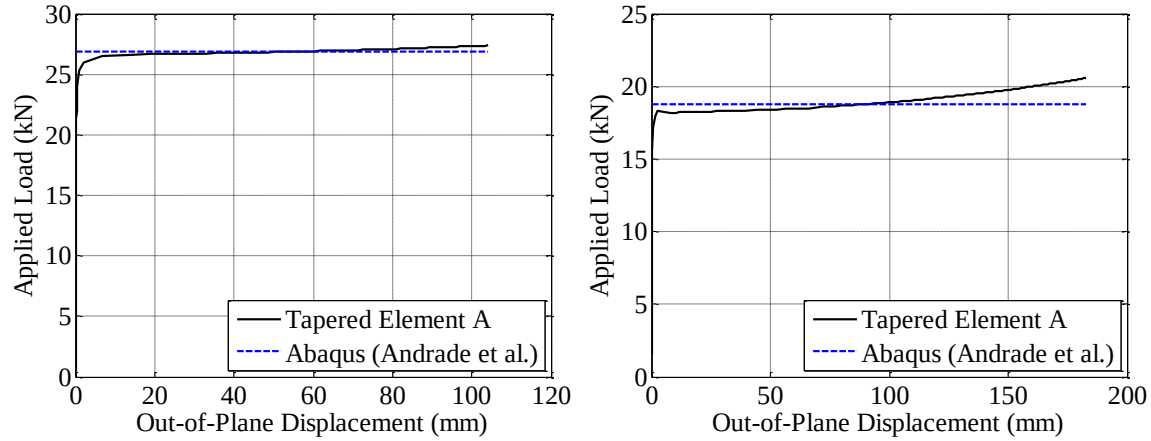

(e) L = 12.0 m, Mid-Height Loading (f) L = 12.0 m, Top Flange Loading

Figure 4.16 Set 2: Simply Supported Double Web-Tapered Beam (α = 0.8)

(See Figure 4.4 (2b))

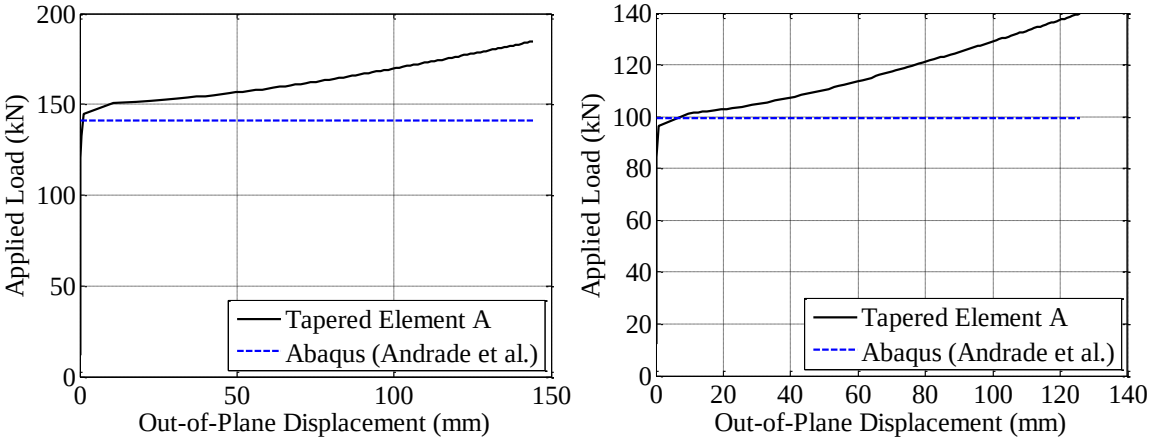

(a) L = 6.0 m, Mid-Height Loading (b) L = 6.0 m, Top Flange Loading

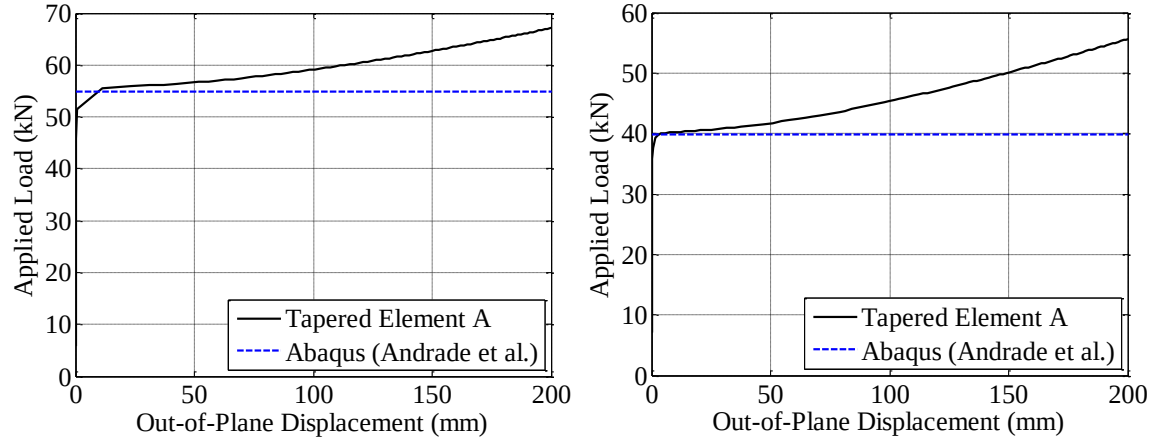

(c) L = 9.0 m, Mid-Height Loading (d) L = 9.0 m, Top Flange Loading

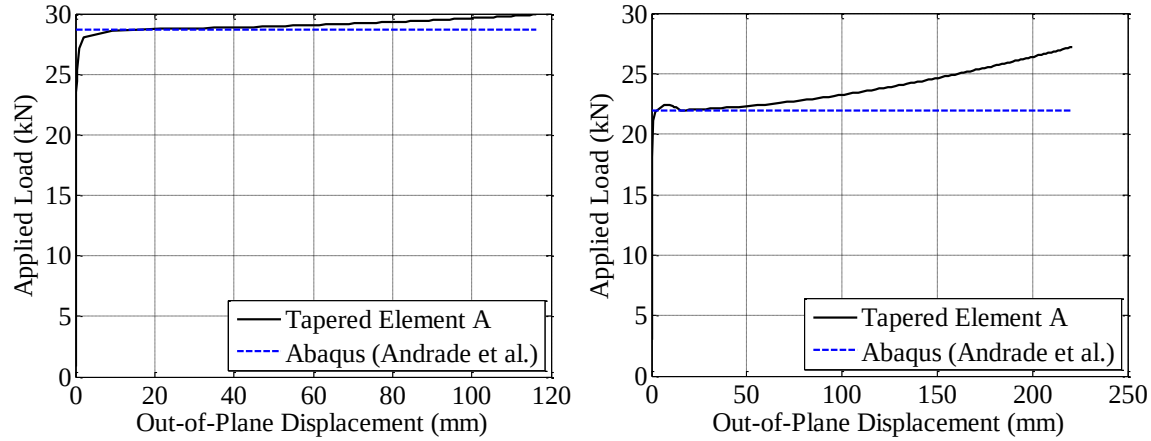

(e) L = 12.0 m, Mid-Height Loading (f) L = 12.0 m, Top Flange Loading

Figure 4.17 Set 2: Prismatic Simply Supported Beam

(See Figure 4.4 (2b))

4.2.3.3 Set 3 Models and Results

The third set of models are depicted through Figure 4.4: (3a). In addition to consistent material properties of $E = 210$ GPa and $\nu = 0.3$, variables of Set 3 which remained constant were:

- maximum web-height: $h_{max} = 300$ mm
- flange thickness: $t_f = 10$ mm
- web thickness: $t_w = 6$ mm

Parameter variation for Set 3 involved:

- web-taper: $h_{min} = \alpha h_{max}$ where $\alpha = 1.0; 0.5$
- member length: $L = 3.0 - 8.0$ m
- loading location: top flange, web mid-height, bottom flange

Numerical modeling of the configurations described for Set 3 involved fiber discretization, element meshing, and torsional load imperfections. Cross-section discretization using fibers is similar to that shown in Figure 2.4 with a row of 10 fibers along the flange width and a row of 20 fibers along the web-height. Each member modeled from Set 3 had a consistent element meshing using Tapered Element A of 10 elements along the member span. Load imperfections were imposed on the models such that members could numerically buckle under LTB. These load imperfections were imposed at the free end of the cantilevers with a torsional force magnitude of a thousandth of the reported critical load obtained by Andrade et al. These load imperfections were applied to the members prior to beginning the analysis involving the transverse load.

Location of element nodes for the models of Set 3 coincide along a member's web mid-height throughout the member length. These nodal locations coincide along the *x*-axis

due to the member symmetry about this axis. Element meshing with Tapered Element A spanned from the fixed boundary condition to the free end using consistent element lengths throughout the member.

Models associated with Set 3 involved transverse loading applied at either the top flange, web mid-height, or bottom flange of a cantilever's free end. Transverse loads being applied at the web mid-height can be directly applied to the element end node of the free end of the cantilever. To simulate top flange or bottom flange loading, use of a rigid element is needed. The rigid element is connected from the node located at the free end to a node designated at either the top flange or bottom flange directly vertical of the previously mentioned node.

Force-displacement plots corresponding to the results of models in case (3a) are seen in Figure 4.18 through Figure 4.23. Responses of these force-displacement plots are based off the end node of each cantilever beam's free end. Overview and comparison of the responses suggest that Tapered Element A slightly under predicts the critical load to the shell FEA. Loading applied at the web mid-height of the prismatic cantilever beam with L = 4.0 m shows to have a substantial amount of overstrength prior to buckling with Tapered Element A with respect to the corresponding member with double web-taper. Although it is not mentioned in the Andrade text, this explanation of load overstrength is most likely due to web buckling at the section of the free end which Tapered Element A is unable to capture.

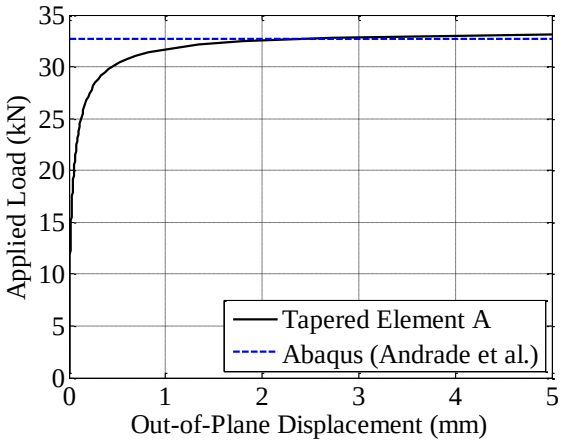

(a) Top Flange Loading

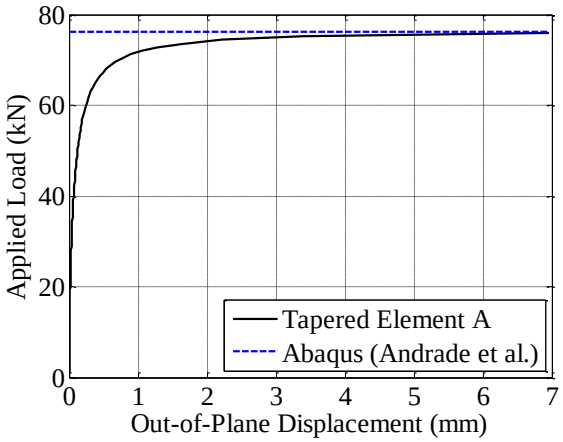

(b) Bottom Flange Loading

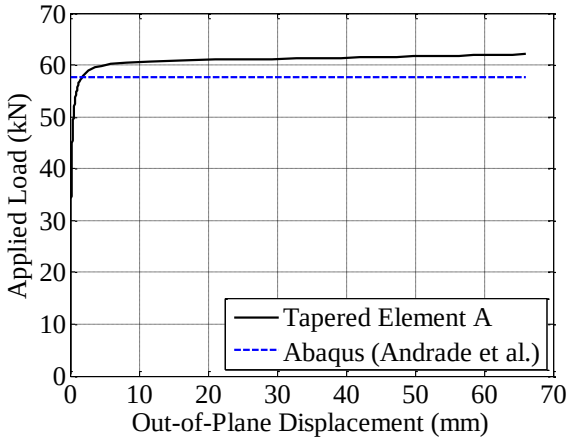

(c) Mid-Height Loading

Figure 4.18 Set 3: Double Web-Tapered Cantilever Beam (L = 4.0 m, α = 0.5)

(See Figure 4.4 (3a))

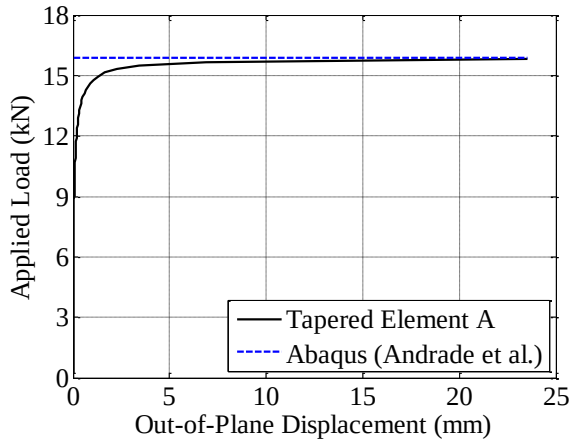

(a) Top Flange Loading

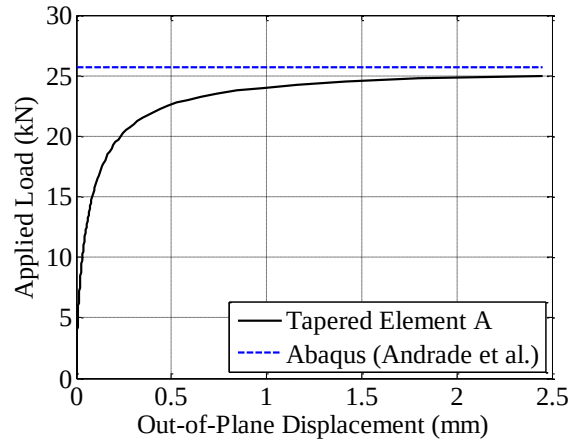

(b) Bottom Flange Loading

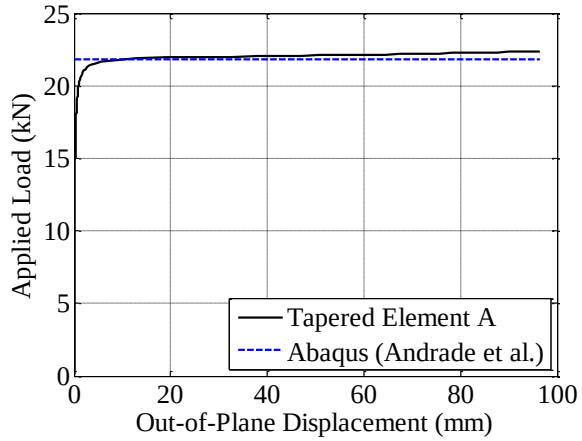

(c) Mid-Height Loading

Figure 4.19 Set 3: Double Web-Tapered Cantilever Beam (L = 6.0 m, α = 0.5)

(See Figure 4.4 (3a))

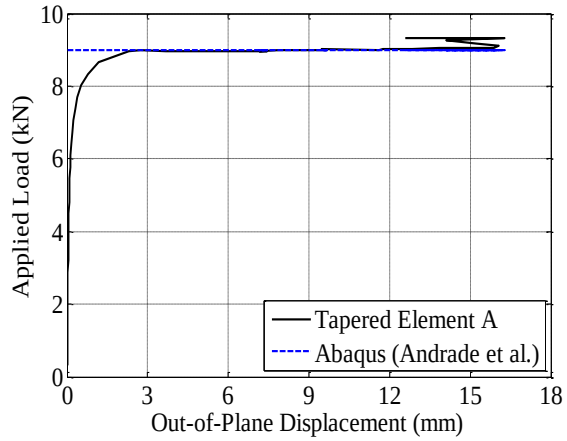

(a) Top Flange Loading

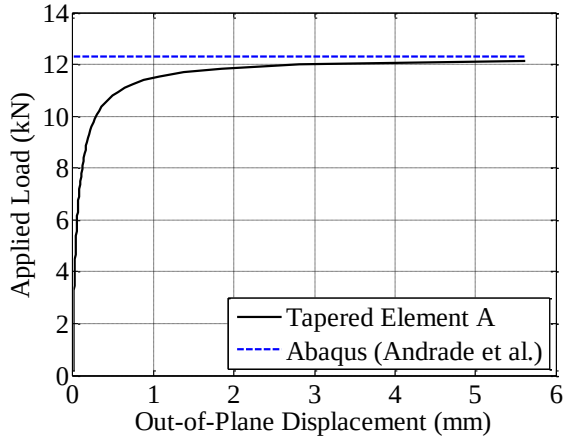

(b) Bottom Flange Loading

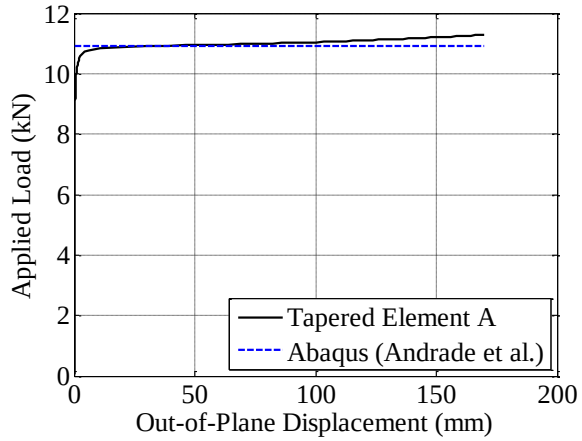

(c) Mid-Height Loading

Figure 4.20 Set 3: Double Web-Tapered Cantilever Beam (L = 8.0 m, α = 0.5)

(See Figure 4.4 (3a))

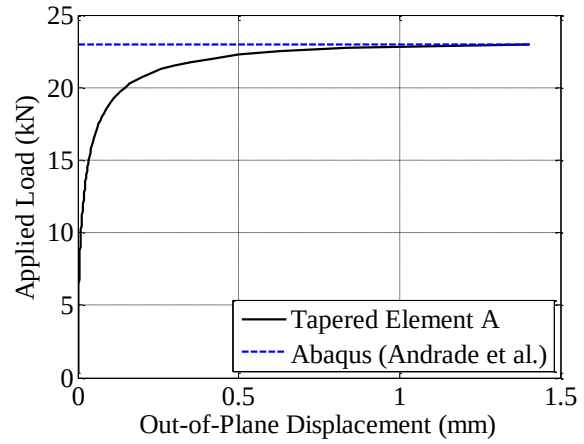

(a) Top Flange Loading

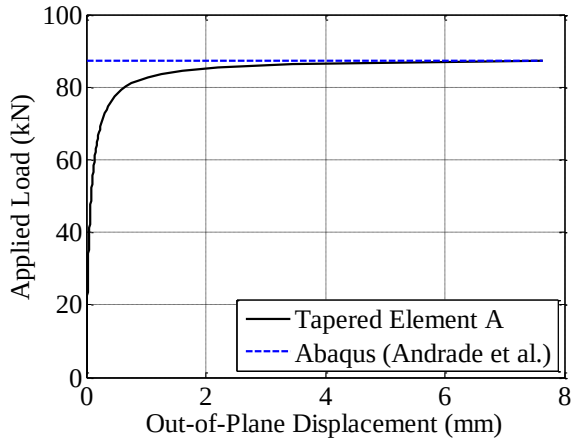

(b) Bottom Flange Loading

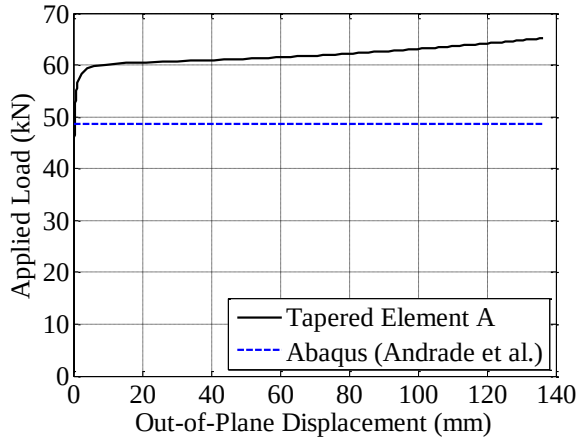

(b) Mid-Height Loading

Figure 4.21 Set 3: Prismatic Cantilever Beam (*L* = 4.0 m)

(See Figure 4.4 (3a))

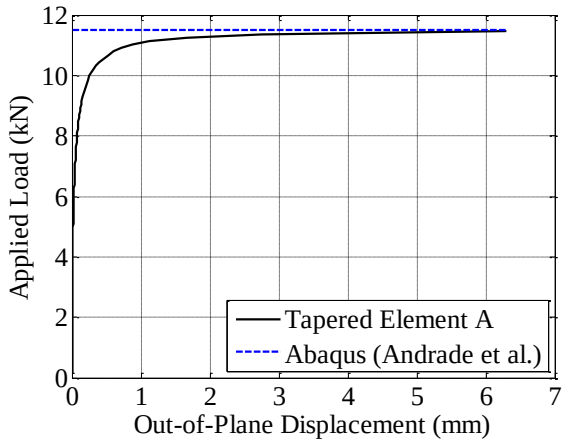

(a) Top Flange Loading

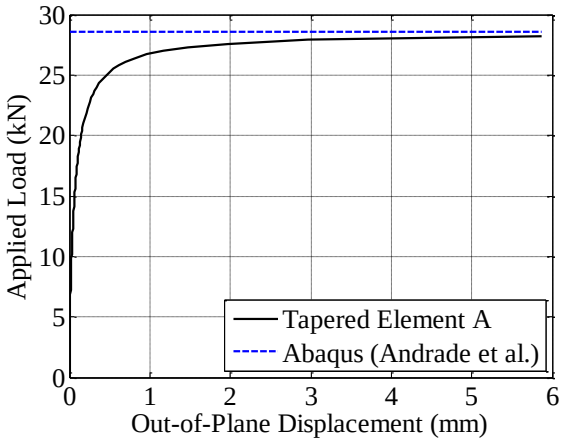

(b) Bottom Flange Loading

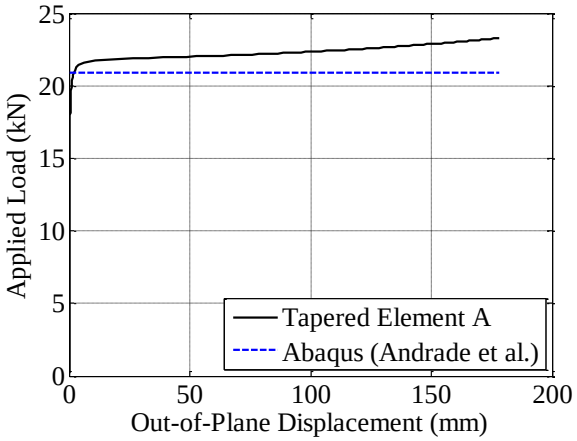

(b) Mid-Height Loading

Figure 4.22 Set 3: Prismatic Cantilever Beam (L = 6.0 m)

(See Figure 4.4 (3a))

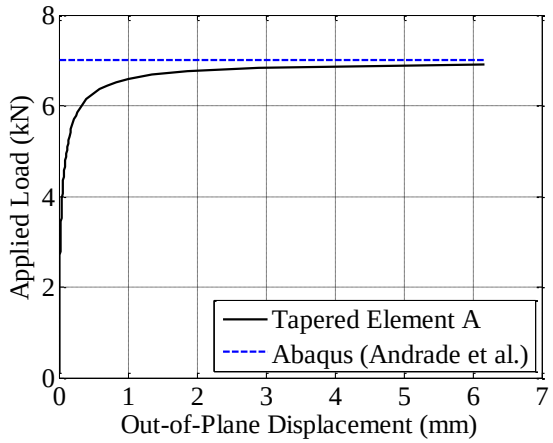

(a) Top Flange Loading

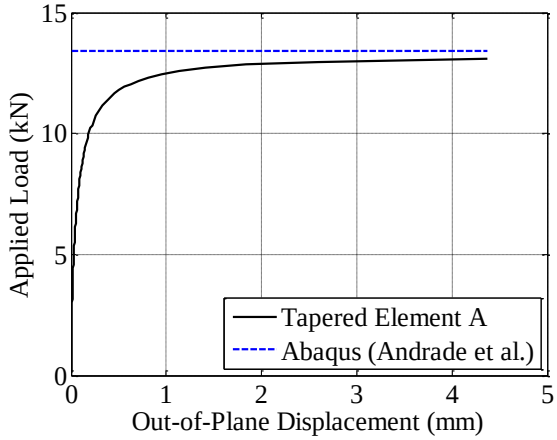

(b) Bottom Flange Loading

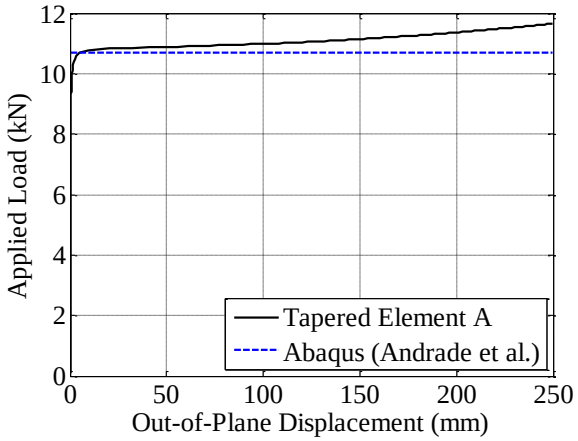

(b) Mid-Height Loading

Figure 4.23 Set 3: Prismatic Cantilever Beam (L = 8.0 m)

(See Figure 4.4 (3a))

4.2.4 Andrade et al. (2007) Convergence Studies

The analyses modeled in the previous section underwent various mesh sizes using Tapered Element A. Although mesh generation varies with each model due to boundary conditions and test configurations, a general idea of elements needed for web-tapered analyses can be determined. Use of insufficient number of elements to model a web-tapered member results in inaccurate displacement fields while an excessive amount of elements can lead into unnecessary computation effort. In order to avoid these issues, several convergence studies on selected models were performed in order to obtain the least residual to the shell element results documented from Andrade's ABAQUS studies. Results of these selected studies are seen in Figure 4.24 through Figure 4.27.

Overall errors seen from these convergence studies suggest reasonable discrepancies that are 10% of the critical load from shell elements modeled in ABAQUS. The cases used for these convergence studies consisted of variation of member lengths, boundary conditions, and loading conditions. It is seen that members of the longest member span of L = 12.0 m yield exceptional results with a meshing of 10 Tapered Element A beam-columns. In cases of mid-height loading, meshing of 8 elements yield discrepancy that is about 2.6% while use of 6 elements of the same model with top flange loading yield 3.2% discrepancy. From these results, conclusion can be made that using 10 Tapered Element A beam-columns is sufficient in capturing elastic LTB response in cases where the member span does not exceed 12.0 m.

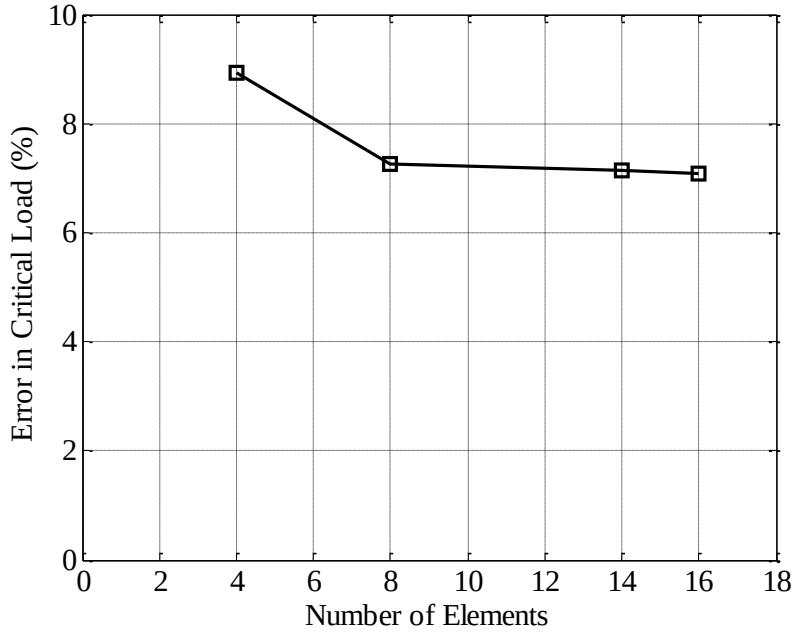

Figure 4.24 Convergence Plot of Case (1b): *L* = 4.0 m Single Symmetry

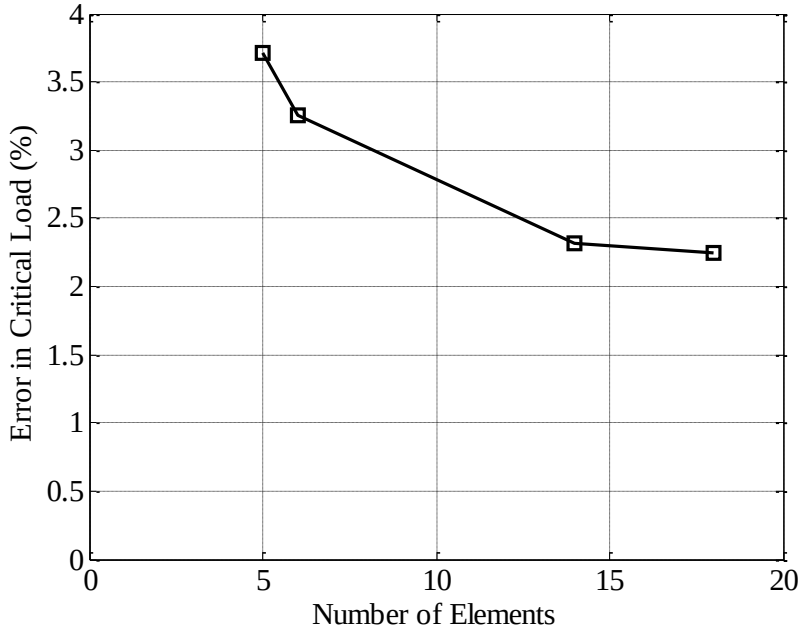

Figure 4.25 Convergence Plot of Case (2a): Top Flange Loading

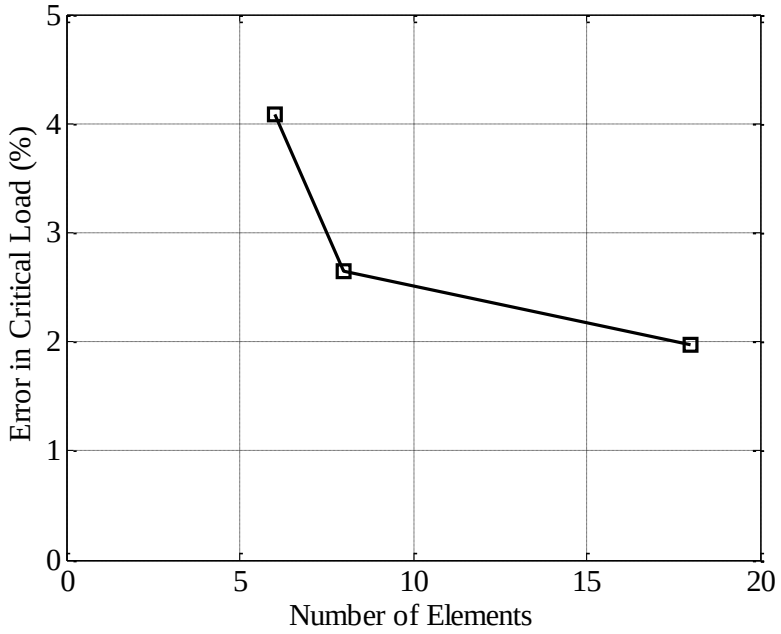

Figure 4.26 Convergence Study of Case (2a): Mid-Height Loading

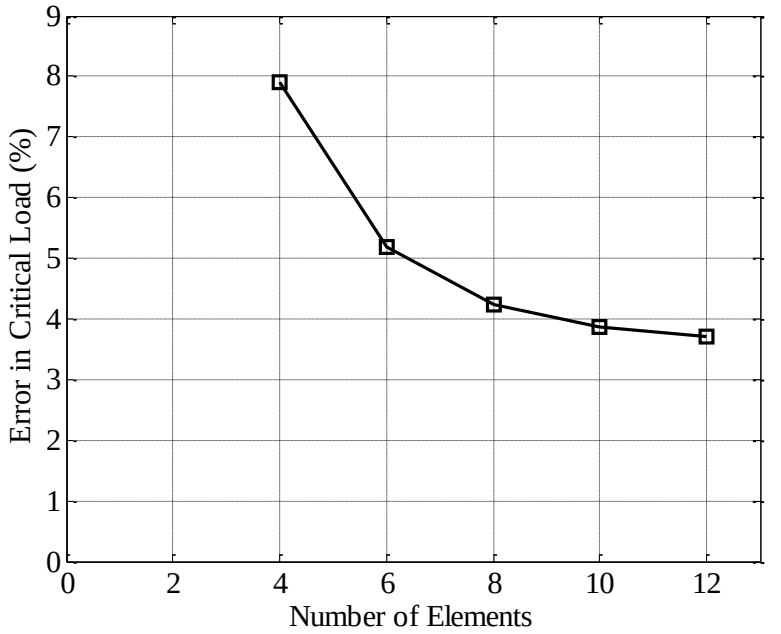

Figure 4.27 Convergence Study of Case (2b): Mid-Height Loading (*L* = 12m, α = 0.4)

4.3 Members with Inelastic Lateral-Torsional Buckling

In order to establish that Tapered Element A works sufficiently for web-tapered members beyond yield, inelastic models and analyses were carried out. Kim (2010) referenced several web-tapered experimental studies which were compared with her numerical results obtained from ABAQUS. A selection of these studies were chosen in this research as a set of benchmark cases. The models consisted of variations of parameters such as use of residual stresses, inelastic material, initial imperfections, and boundary conditions. Throughout the discussion of this section, reference to the total section depth at the shallow and deep ends of a member are d_s and d_L, respectively.

4.3.1 Prawel et al. (1974)

4.3.1.1 Test Configuration

Prawel et al. (1974) executed experimental testing of a total of 15 specimens: three being web-tapered simply supported beams and twelve being web-tapered beam-columns. It was determined that all three beams were slender members while the beam-columns had a variety of slender, noncompact, and compact members. Assembly of the specimens discussed in the Prawel et al. studies involved built-up I-sections of either shear cut plate and oxygen cut plates. These plates were then assembled to form the web-tapered members through a continuous fillet weld applied only on one side of the web-flange plate intersection.

All members of the beam and beam-column specimens consisted of a single web-taper geometry along the longitudinal span. This single web-taper was fabricated such that the top flange of a beam would run parallel to the longitudinal axis. Same fabrication was

done for the beam-column specimens with the varying incline angle (or pitch), α, of the specimen is varied with respect to the top flange. The web-taper rate, β, is varied with each specimens and is referenced from the bottom flange to the longitudinal axis for both beams and beam-columns. Dimensions of the flange plate's width and thickness and web plate's thickness remained constant throughout the entire length of the specimens. Testing configuration of the beams and beam-columns are seen in Figure 4.28 and Figure 4.29, respectively.

For the beam specimens, member loads consisted of two transverse concentrated loads applied at the top flange of locations B and C such that the load at C is either 28% of the load at B or non-existent. In the former case, the loading, in the elastic range, created a uniform stress distribution across the flange between the unbraced segment BC. By neglecting a vertical load at location C, a more significant flange stress gradient between the unbraced segment BD would be observed (Prawel et al. 1974). Web-taper angle for the beam specimens, β, was measured as the angle from the horizontal plane to the bottom flange of the beam as seen in Figure 4.28.

Beam-column specimens also consisted of linearly web-tapered members with prismatic flanges and doubly symmetric I-sections. Variation of the angle, α, designates the orientation of how the cantilever is inclined with respect from the horizontal to the top flange as depicted in Figure 4.29. The web-taper angle for the cantilever beams were measured in the same way as the simply supported beams mentioned previously. Loading sequence of the beam-column specimens consisted of both axial and moment loads applied to the system simultaneously and equivalently as seen in Figure 4.29.

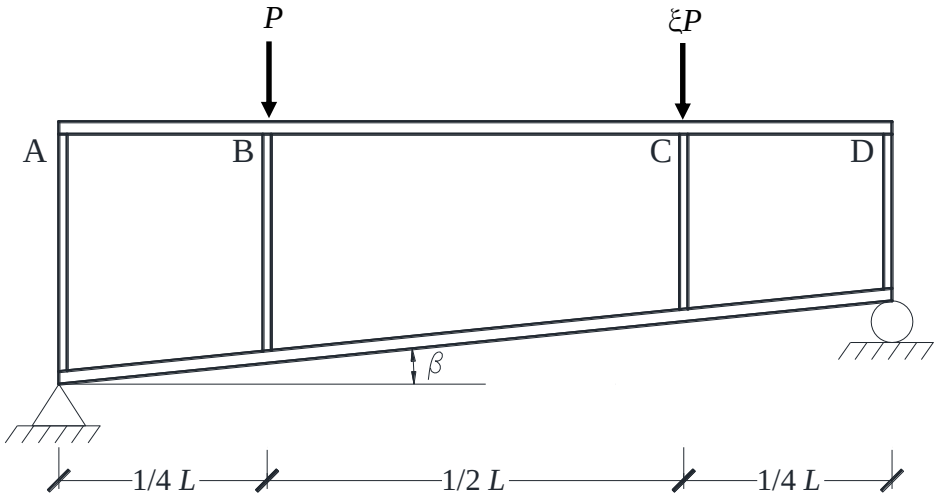

Figure 4.28 Beam Test Configuration of Prawel et al. (1974)

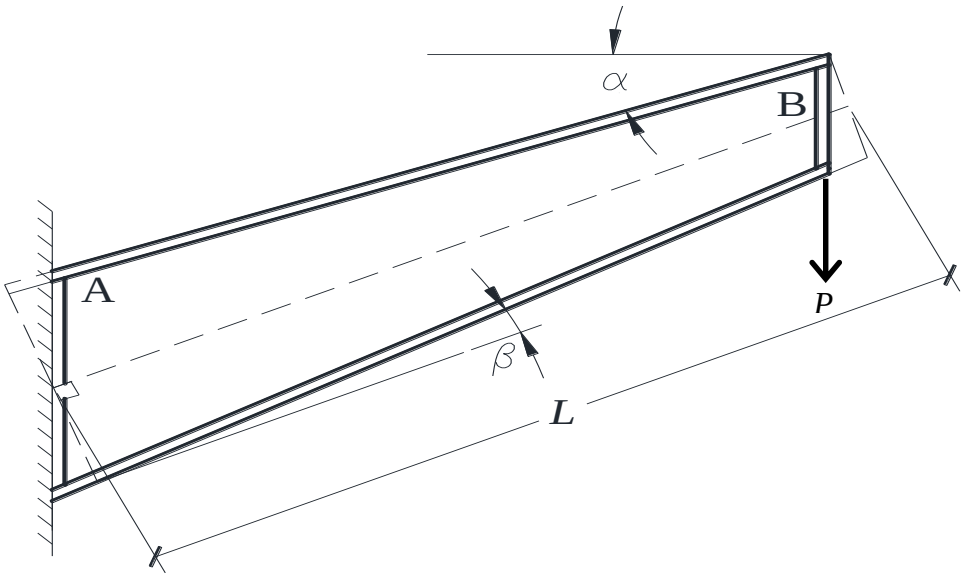

Figure 4.29 Beam-Column Test Configuration of Prawel et al. (1974)

4.3.1.2 Boundary Conditions

The simply supported beams of the test configurations consisted of lateral bracings provided at the supports as well as the quarter points. These lateral restraints were placed at each of the four flange tips of location. Due to the configuration of these lateral bracings, the possibility of twisting at these locations are also constrained while warping could still occur.

In addition to the typical constraints imposed at the fixed end of a cantilever beam, the beam-column specimens had lateral bracings similar to that described for the simply supported beams. Lateral bracings imposed on the free-end consequently prevents any twisting which may incur during the testing.

4.3.1.3 Material Properties

Material properties used for the following inelastic models are based on a true stress-strain curve discussed by Kim (2010) and depicted in Figure 4.30 for a yield stress of 55 ksi and an ultimate strength of 70 ksi of A572 Gr. 55 steel as an example. The true stress-strain relation is derived from the engineering stress-strain points as follows (Ugural and Fenster 2012):

$$\sigma_{true} = \sigma_{eng}(1 + \varepsilon_{eng}) \tag{4.3}$$

$$\varepsilon_{true} = ln(1 + \varepsilon_{eng}) \tag{4.4}$$

As stated by Kim, an assumption is made for the strain hardening strain, ε_{st}, to be ten times the yield strain, ε_y, with a corresponding strain hardening modulus, E_{st}, of 700 ksi. The strain hardening stress, σ_{st}, is assumed as:

$$\sigma_{st} = \sigma_y + \frac{2}{3}(\sigma_u - \sigma_y) \tag{4.5}$$

The corresponding engineering strain at this material's ultimate strength, ε_u, is assumed as (see the dashed stress-strain curve in Figure 4.30):

$$\varepsilon_u = 70\varepsilon_y \tag{4.6}$$

Based on the previous relations, the true stress-strain relations is shown as the solid line in Figure 4.30 and is tabulated in Table 4.2. Any strain value exceeding the ultimate strain is assumed to be limited by the ultimate stress value (Kim 2010).

Table 4.2 Engineering and True Stress-Strain Data for A572 Grade 55 Steel

Engineering		True	
Stress (ksi)	Strain (in./in.)	Stress (ksi)	Strain (in./in.)
55.0	0.0019	55.1	0.0019
55.0	0.0190	56.0	0.0188
65.0	0.0333	67.1	0.0327
70.0	0.1328	79.2	0.1247

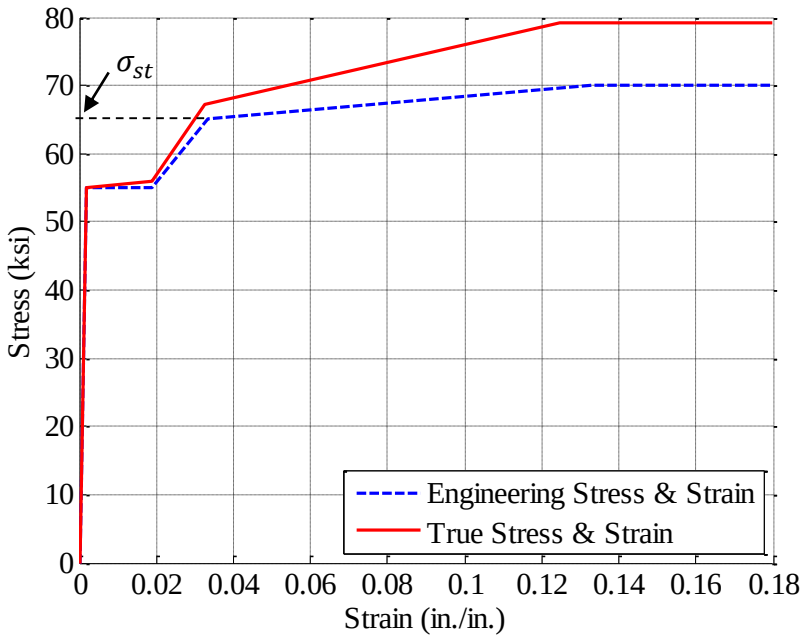

Figure 4.30 Typical Stress-Strain Curve for F_y = 55 ksi

Specimens tested by Prawel et al. were fabricated from ASTM A242 steel with nominal yield strength of 42 ksi and had reported measured yield stress being 52 ksi. Corresponding specified minimum ultimate tensile strength is 70 ksi. As the stress-strain relationship was not provided in Prawel et al., similar methods mentioned in this section was applied in order to determine the true stress-strain relation that is seen in Figure 4.31. A tabulated summary of the key points are referred to in Table 4.3.

Table 4.3 Stress-Strain Values for Prawel et al. (1974) Models

Engineering		True	
Stress (ksi)	Strain (in./in)	Stress (ksi)	Strain (in./in)
52.0	0.0018	52.0	0.0018
52.0	0.0179	52.9	0.0178
59.3	0.0284	61.0	0.0280
63.0	0.1255	70.9	0.1182

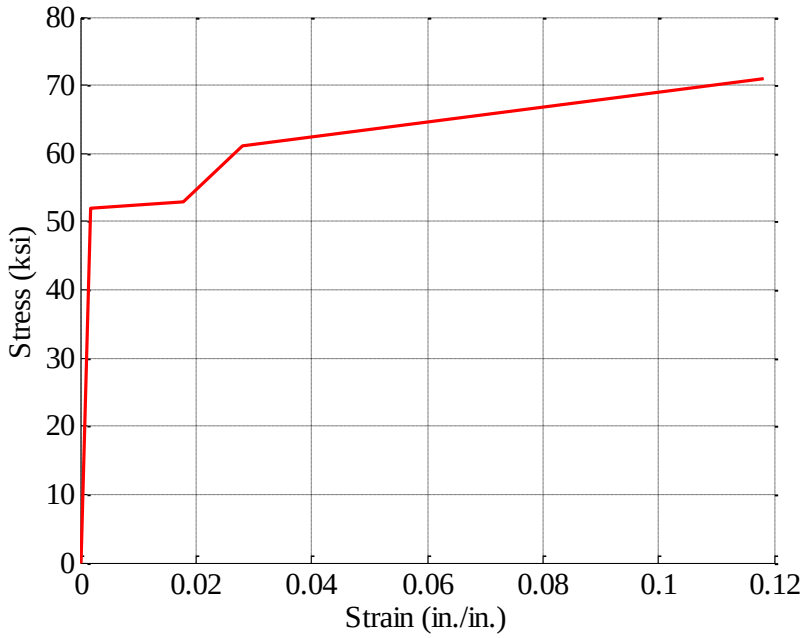

Figure 4.31 Steel Stress-Strain Curve for F_y = 52 ksi

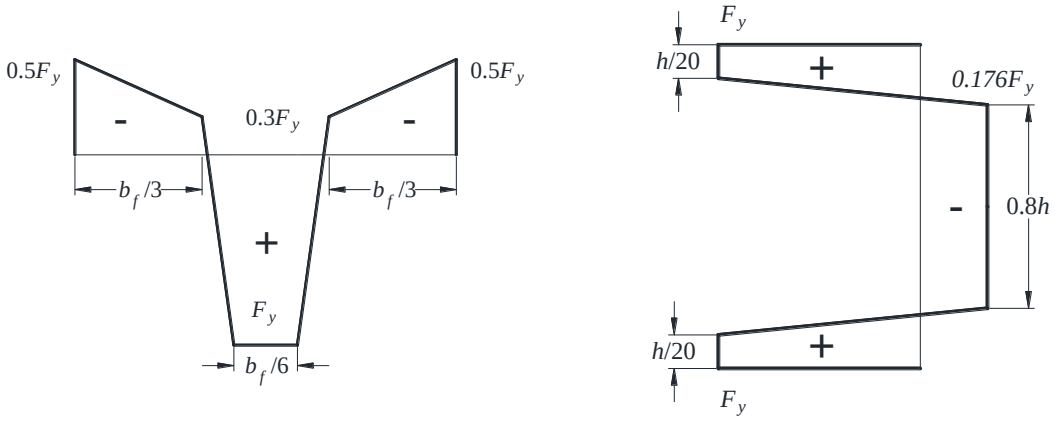

(a) Flange Distribution (b) Web Distribution

Figure 4.32 Residual Stress Pattern (Prawel et al. 1974)

4.3.1.4 Residual Stresses

Depending on how a plate was cut (i.e., oxygen cutting versus shear cutting), residual stresses for the specimens tested by Prawel et al. would vary. Plates involved with oxygen cutting resulted with tension at the flange tips while plates involved with shear cutting resulted with compression at the flange tips. Because the specimens tested by Prawel et al. consisted of the web and flange welded longitudinally on only one side of each specimen, measured residual stresses showed to be un-symmetric about the web height. Residual stress patterns based off shear cuts were made to be symmetric for the purpose of numerical studies and seen in Figure 4.32.

4.3.1.5 Numerical Modeling in OpenSees

All three simply supported beam specimens were numerically modeled using the proposed element through OpenSees. Specimen geometry of each specimen for this set are referred to Table 4.1. Nodes associated with the beam restraints and quarter points were imposed with constraints that prevented lateral displacement, longitudinal direction

of the roller end excluded, as well as fixing the twist displacement field. All models consisted of 20 proposed beam-column elements spanning the member length which ran along the web mid-height. Because the test protocol involved top flange loading, rigid beam-beam column elements were integrated with the proposed elements in a similar fashion to that describe with the Andrade et al. (2007) sets.

Beam-column specimens involved with shear cut edge preparation were selected for the second set of numerical models using the proposed element. Geometry of these selected specimens are tabulated in Table 4.5. Nodal configuration was established in a similar fashion to the simply supported beams by running along the web mid-height along the span. All DOFs associated with the fixed end were constrained whereas the node associated at the free end had constraints from lateral displacements and twisting while warping remained unrestrained. Each model consisted of 20 beam-column elements that were connected through the nodal configuration which was mentioned. Loading of each specimen was taken to be a downward vertical force applied at the free end of the specimen in order to simulate a simultaneous axial and flexural force.

Cross-section discretization of each integration point along a proposed element for both sets consisted of 21 fibers across each flange and 21 fibers along the web height. Use of a trilinear material model described in Section 4.3.1.3 was applied to each fiber of the cross-sections based off F_y = 52 ksi and F_u = 70 ksi. Residual stress patterns based off the shear cut method (see Figure 4.32) were also considered in each model. Because initial imperfections were not reported by Prawel et al., all models were treated to have an out-of-plane initial imperfection along each specimen with a peak value of L_b/1000 at a specimen's mid-span length.

Table 4.4 Prawel et al. (1974) Beam Test Properties and Configurations

Specimen No.	d_s (in.)	d_L (in.)	t_w (in.)	b_f (in.)	t_f (in.)	L (in.)	ξ	h_L/t_w	$b_f/2t_f$	Compactness
LB-3	6.0	16.0	0.105	4.0	0.25	144.0	0.28	147.6	8.0	slender
LB-5	6.0	16.0	0.105	4.0	0.25	96.0	0.28	147.6	8.0	slender
LB-6	6.0	16.0	0.105	4.0	0.25	96.0	0.0	147.6	8.0	slender

Table 4.5 Prawel et al. (1974) Beam-Column Test Configurations

Specimen No.	d_s (in.)	d_L (in.)	L (in.)	α (°)	β (°)	h_L/t_w	$b_f/2t_f$	Compactness
LB-C-5	6.0	16.0	112.8	30	5.72	161.9	12.0	slender
LB-C-10	6.0	18.0	114.0	20	5.71			
LB-C-1	6.0	12.0	120.0	0	2.77	107.6	12.0	noncompact
LB-C-9	6.0	12.0	115.4	20	2.83			
LB-C-3	6.0	6.0	116.5	30	0.0	52.4	12.0	compact
LB-C-7	6.0	6.0	116.5	20	0.0			

4.3.1.6 Assessment of Results

Numerical modeling of the simply supported beams showed to correlate fairly well to the results documented by Prawel et al. Comparison of total loads applied to the specimens based off testing and the proposed element are referred to Table 4.6. With the exception of LB-3, the other two beams (LB-5 and LB-6) were governed by local buckling in the flange. Because effects of local buckling are neglected in the proposed element, maximum strength observed from analyses will deviate. Specimen LB-5, for instance, shows a stronger predicted total load than testing by almost 8%. Although Specimen LB-6 invovled local buckling, analysis suggests the total load prior to global buckling is slightly less than observed by Prawel et al. This under predicted value is possibly related to the moment gradient between segment BD since lateral bracing is omitted at location C and the only load applied was at location B.

Specimen LB-3 was observed to be the only specimen out of all the beams and beam-columns where lateral buckling was the governing mode. Soon after this buckling mode, it was reported that buckling of the flange soon followed. Prawel et al. observed lateral buckling occurred when the total load on the system was 32 kips (P_{total} = 32 kips) whereas the analysis predicted a maximum strength of 29.8 kips (P_{total} = 29.8 kips). In addition to the reported maximum load, Prawel et al. provided a force-displacement plot of the test data for LB-3 for the midspan in-plane deflection. A composite plot of the analysis and test results are seen in Figure 4.3. Comparison of the two data sets show a very well defined correlation between numerical simulation and experimental testing.

Table 4.6 Experimental and Simulated Beam Results for Prawel et al. (1974)

Specimen No.	P_{total} (kips)		Error (%)
	Test	OpenSees	
LB-3	32.0	29.8	6.8
LB-5	50.0	53.9	7.8
LB-6	46.0	45.3	1.5

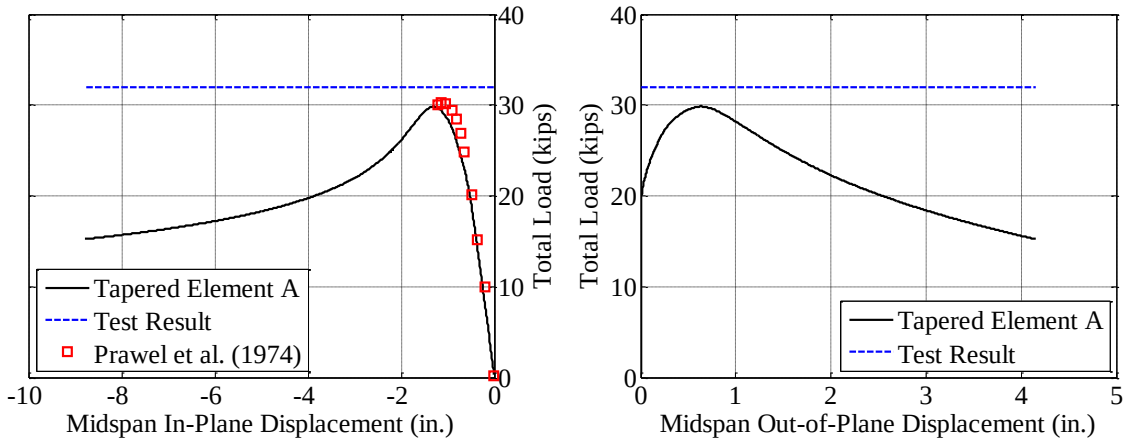

(a) In-Plane Response (b) Out-of-Plane Response

Figure 4.33 Specimen LB-3 Analysis Response

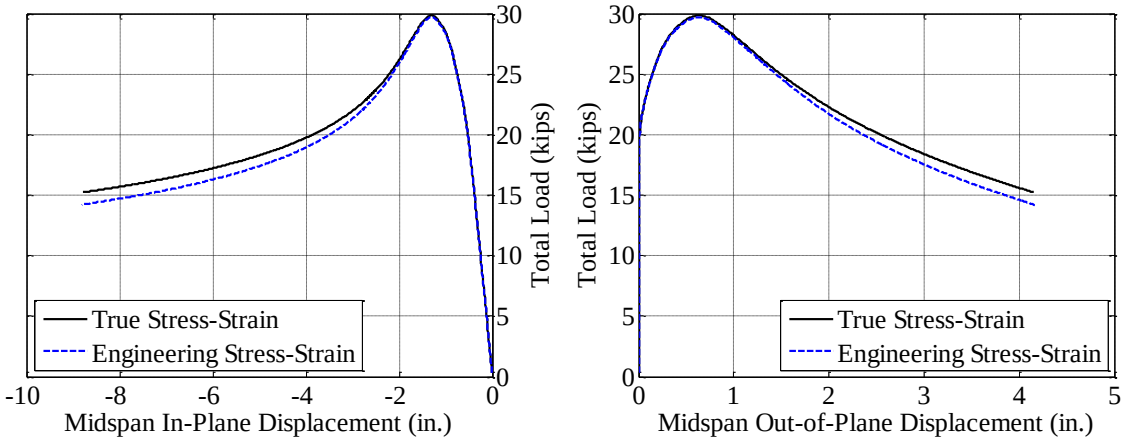

(a) In-Plane Response (b) Out-of-Plane Response

Figure 4.34 Analysis of LB-3 with True and Engineering Stress-Strain

In addition to the analyses of the simply supported beam specimens, behavior response of using true stress-strain opposed to engineering stress-strain relations was assessed. Specifically, analysis of specimen LB-3 was modeled with the engineering stress-strain relation and compared to the results obtained using the true stress-strain points. Response of out-of-plane and in-plane displacements of the member midspan is seen in Figure 4.34. Comparison of using the two stress-strain sets show responses prior to buckling match exactly with one another. Peak load of the specimen yields the same value of P_{total} = 29.7 kips. Deviation of results become apparent during the post-buckling response of the two sets as the model using the engineering stress-strain relations yield less strength than when using the true stress-strain material relation. This suggests that analysis obtained using material models based on engineering stress-strain relations yield slightly more conservative results than the true engineering stress-strain model. Because use of beam-column elements assume constant cross-sectional area in an analysis, it is highly recommended that the engineering stress-strain relation be used for these elements.

Table 4.7 Comparison of Beam-Column Results for Prawel et al. (1974)

Specimen No.	P_{max} (kips)		Error (%)
	Test	OpenSees	
LB-C-1	8.7	8.2	5.7
LB-C-3	4.3	5.0	16.2
LB-C-5	15.0	14.6	2.6
LB-C-7	4.1	4.8	17.0
LB-C-9	9.3	9.0	3.2
LB-C-10	14.3	13.4	6.2

Results of beam-column analyses involved with shear cuts are compared to reported test data in Table 4.7. The set of specimens consisted of various parameters involving angle orientation of the cantilever, member web-taper, and compactness classification.

Similar to LB-5 and LB-6, all beam-column specimens tested by Prawel et al. were limited by an occurrence of flange buckling. Because the proposed element is unable to capture this local buckling mode, most, if not all, of the analysis results should show higher strength capacities than their tested counterparts. However, all but two specimens (i.e., LB-C-3 and LB-C-7) show to underestimate the maximum strength from analyses opposed to overestimating.

Out of the six selected beam-column specimens, LB-C-3 and LB-C-7 were classified as compact. These specimens also were prismatic members whereas the remaining specimens had various web-tapers. Both of these compact members predicted peak load strengths higher than the experimental results, albeit they were not significantly higher. An overview of the three classifications suggest that analyses involving compact sections will overestimate peak strength compared to those of slender and noncompact specimens.

4.3.2 Shiomi and Kurata (1984)

4.3.2.1 Test Configuration

Shiomi and Kurata (1984) tested a total of 24 full-scale, simply supported beam-column specimens. As Figure 4.35 shows, each specimen is laterally braced at both the top and bottom flanges and tapers throughout the web such that the neutral axis of any given cross section is located at the web's center. Rate of the web-taper is determined by the angle, 0.5β, with reference between the horizontal plane and the bottom flange. Additional lateral bracing at the one-third location was provided to 5 specimens only. Fabrication of each specimen was done using double fillet welds to the web and flange connections along the longitudinal member span.

Specimens tested consisted of both axial loads and flexural loads being applied at the roller support as seen in Figure 4.35. Application of these loads were applied simultaneously throughout the tests opposed applying a constant axial load prior to applying the end-moment at the support.

4.3.2.2 Boundary Conditions

Configuration of each test specimen was established such that the section mid-height of the member ends correspond with the supports. The shorter end, d_s, of the specimen was braced by a pin support while the longer end, d_L, was constrained by a roller support. Constraints relating to twisting and warping at the ends of each specimen were not explicitly stated through the test arrangement. Based on the schematic test setup documented by Shiomi and Kurata, it was assumed that both of these displacements were restrained at both ends.

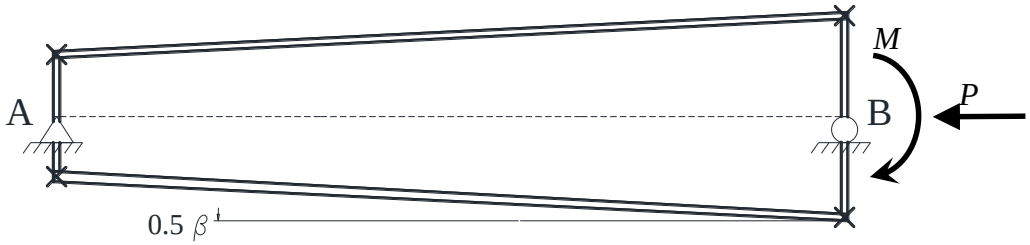

Figure 4.35 Schematic of Shiomi and Kurata Test Setup

4.3.2.3 Material Properties

Specimens tested by Shiomi and Kurata were fabricated from SS-41 grade (Japanese grade) steel with a specified yield stress of 34.1 ksi. Although measured material properties were not explicitly stated, ratio of the applied axial force to the yield force of the shorter cross-section and ratio of applied end-moment to the yield moment of the longer cross-section were provided. From these values, actual yield stresses of the web and flange plates can be determined through back calculation (Kim 2010).

Calculated yield stress values of the flange and web plates for two specimens (OT-1.6-1 and OT-2.0-3) are shown in Table 4.8. Although yield stress varied between the flange and web plates for each specimen, it was assumed that yielding of the flange plates would be predominant than that of the web for the numerical models. Yield strength of the flanges for each specimen are stated in Table 4.8. True stress-strain relation of the two specimens are obtained in a similar fashion described in Section 4.3.1.3. The determined stress-strain relations are found in Table 4.9 and represented in Figure 4.34.

Table 4.8 Yield Stresses of Specimens OT-1.6-1 and OT-2.0-3

Specimen	Yield Stress (ksi)	
	flange	web
OT-1.6-1	40.4	41.2
OT-2.0-3	42.6	40.1

Table 4.9 True Stress-Strain Values for Shiomi and Kurata (1984) Models

Specimen OT-1.6-1		Specimen OT-2.0-3	
F_y = 40.4 ksi		F_y = 42.6 ksi	
Stress (ksi)	Strain (in./in)	Stress (ksi)	Strain (in./in)
40.4	0.00139	42.5	0.00146
40.9	0.01339	43.1	0.01446
52.7	0.02839	55.5	0.03046
62.1	0.09239	65.7	0.09746

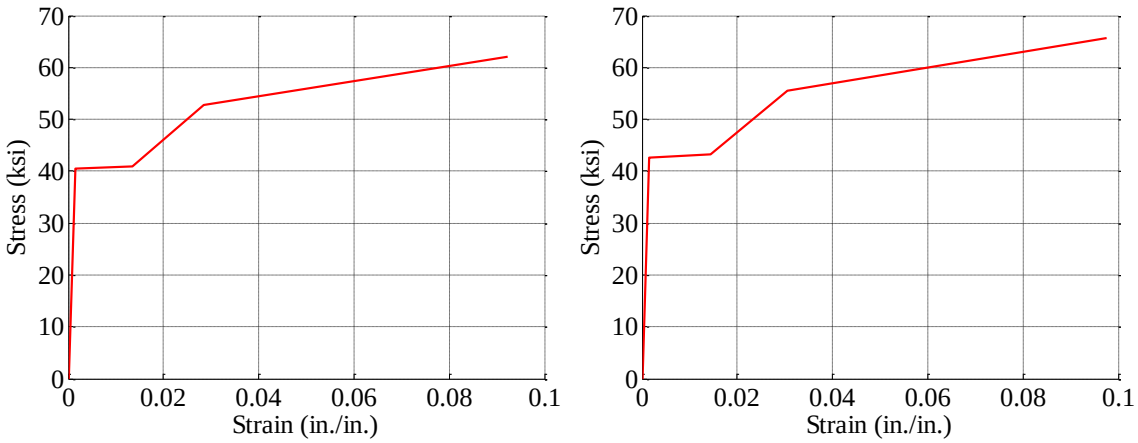

(a) F_y = 40.4 ksi (b) F_y = 42.6 ksi

Figure 4.36 Steel True Stress-Strain Curves

4.3.2.4 Residual Stresses

Residual stress patterns were also incorporated to the numerical models of the selected specimens. Although Shiomi and Kurata discussed and showed stress patterns of sections associated to one of the specimens, measured residual stress data were not provided. Residual stress patterns based on Prawel et al. (1974) residual stresses (see Figure 4.32) were used instead. However, Kim (2010) suggests modification to these residual stresses in order to avoid significant conservative. The modified residual stresses used was therefore taken to be 80% of that seen in Figure 4.32.

4.3.2.5 Numerical Modeling in OpenSees

Two of the 24 specimens were selected and modeled using the proposed beam element. The two specimens selected were OT-1.6-1 and OT-2.0-3, both of which are laterally braced at the supports only. A tabulated summary of essential properties for these two specimens are provided in Table 4.10. Like the remaining 22 specimens tested by Shiomi and Kurata, the two used for numerical modeling were classified as compact. Both models used 20 proposed beam-column elements which spanned the member length. Since the web mid-height was collinear to the longitudinal axis, equivalent spacing of the element nodes were placed along this axis.

Each cross-section associated with the integration points of the element used a discretization of 21 fibers across the flanges as well as along the web height. A trilinear material model based off the stress-strain relations from Table 4.9 were used for the corresponding specimen. In addition, use of the modified residual stress pattern discussed in Section 4.3.2.4 was integrated into the numerical models.

Table 4.10 Shiomi and Kurata (1984) Test Properties and Configurations

Specimen No.	d_s (in.)	d_L (in.)	t_w (in.)	b_f (in.)	t_f (in.)	L (in.)	h_L/t_w	$b_f/2t_f$
OT-1.6-1	6.57	10.13	0.24	3.20	0.32	118.11	39.5	5.0
OT-2.0-3	5.88	10.87	0.24	3.95	0.31	98.43	42.7	6.3

Measured initial imperfections were determined from Shiomi and Kurata and were measured to be $L_b/2000$ and $L_b/5000$ for specimens OT-1.6-1 and OT-2.0-3, respectively. These initial imperfections were imposed at the out-of-plane direction along the specimen length using half a sinusoidal wave pattern.

Loading protocol used during the experimental testing consisted of an axial load being simultaneously applied with an end-moment applied at the roller support. Reported ultimate axial load, P, and ultimate bending moment, M, for each specimen was as follows:

- OT-1.6-1: P = 17.9 kips and M = 415.9 kip-in.
- OT-2.0-3: P = 50.5 kips and M = 399.1 kip-in.

Because analyses of inelastic models are prone to having great difficulty solving for a corresponding displacement with a load control integrator near critical buckling loads, a displacement control method was used.

4.3.2.6 Assessment of Results

Experimental data obtained by Shiomi and Kurata reported peak axial load as well as corresponding end moment of each specimen. Peak moments for Specimens OT-1.6-1 and OT-2.0-3 are reported and compared to the experimental counterparts in Table 4.11. Both of the specimens were classified compact but had different lengths and web-tapers as noted in Table 4.10. Specimen OT-1.6-1 had the longer span of the two members and

yielded a significant discrepancy compared to the peak moment seen from testing. Specimen OT-2.0-3 was 10 in. shorter than the former member but involved a steeper web-taper. Peak moment determined from analysis for OT-2.0-3 was slightly less than the testing equivalent.

Pushover responses from analysis of both specimens were produced to assess the predicted post-buckling path. Force-displacement plots of both in-plane and out-of-plane displacements at the midspan of each specimen are seen in Figure 4.37 and Figure 4.38 for OT-1.6-1 and OT-2.0-3, respectively. Comparison of the post-buckling responses of these two specimens show significant differences. Specimen OT-1.6-1, for instance, experiences an instant loss of strength soon after buckling occurs while OT-2.0-3 has a gradual loss of strength as loading is increased. Similar conclusions are made when comparing the out-of-plane displacements of OT-1.6-1 and OT-2.0-3.

Although beam-columns occasionally experience varying axial forces dependent on certain loading schemes, common occurrences of beam-column members experience constant axial loads. Column members, for example, experience gravity loads from a structure's dead weight and HVAC systems. Since this constant axial pattern is very common, it is beneficial to assess behavior and response of the proposed element with an end moment and constant axial load.

Peak moments determined from analysis for specimens OT-1.6-1 and OT-2.0-3 with incremental and constant axial loads is reported in Table 4.12. Both specimens show to have a noticeable decrease of moment capacity when loading scheme of the axial load was applied prior to the concentrated end moment. Peak moment prior to buckling with

Table 4.11 Experimental and Simulated Results for Shiomi and Kurata (1984)

Specimen No.	Maximum Moment (kip-in.)		Error (%)
	Test	Analysis	
OT-1.6-1	416.0	361.4	13.1
OT-2.0-3	399.0	388.1	2.7

Table 4.12 Analysis Results of Alternative Axial Load Application

Specimen No.	Maximum Moment (kip-in.)		Difference in M_u (%)
	Incremental Axial Load	Constant Axial Load	
OT-1.6-1	361.4	343.5	5.0
OT-2.0-3	388.1	375.0	3.4

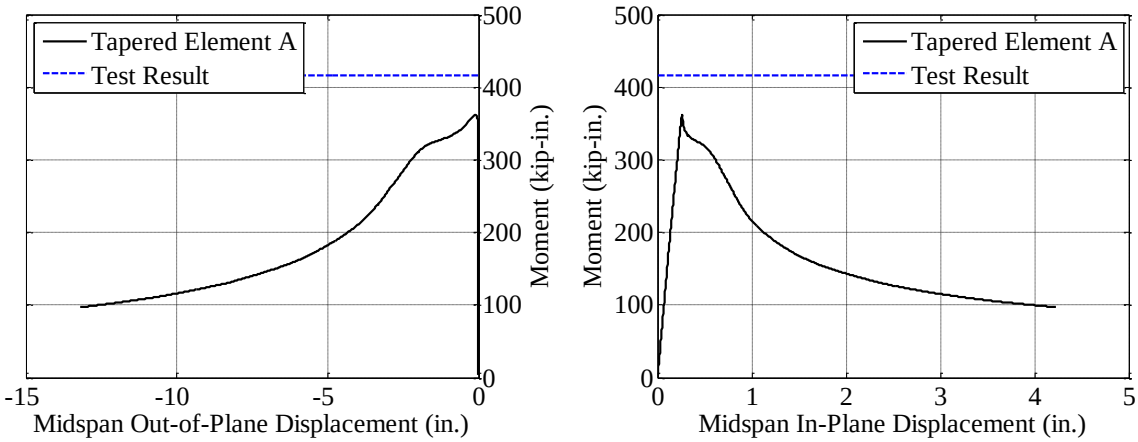

(a) Out-of-Plane Response (b) In-Plane Response

Figure 4.37 Specimen OT-1.6-1 Analysis Response

the constant axial load resulted in a 5% strength loss for OT-1.6-1 and a 3.4% strength loss for OT-2.0-3.

Response plots of the vertical displacements occurring at specimen midspan with the both cases of axial load application is seen in Figure 4.39. Elastic and post-buckling response for both specimens show to match up in a similar trend for both type of loading schemes.

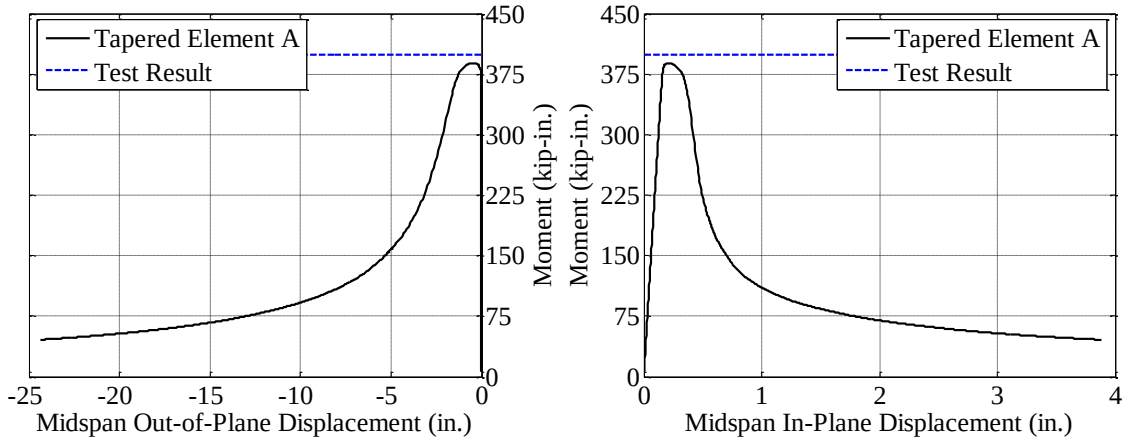

(a) Out-of-Plane Response (b) In-Plane Response

Figure 4.38 Specimen OT-2.0-3 Analysis Response

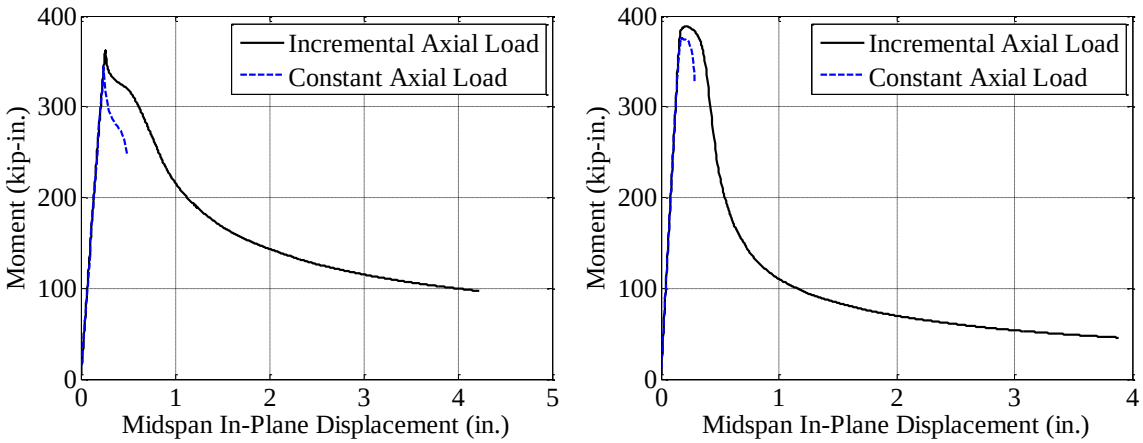

(a) OT-1.6-1 (b) OT-2.0-3

Figure 4.39 Response of Axial Load Application

5 CORRELATION STUDIES: CYCLIC LOADING

5.1 General

Validation of the proposed beam-column element with cyclic test data of Smith et al. (2013) is presented in this chapter. A total of ten rafter specimens underwent experimental testing through cyclic loading (see Table 5.1). These specimens varied in geometries including, but not limited, to web-taper, unbraced Controlling Segments[a] (CS), and plate thickness variations. Although ten specimens were tested, only six of these ten were modeled and simulated using the proposed beam-column element. The remaining three specimens (PF1, CS2, CS3, and CS4) were omitted. Reasons for this omission were due to the fact that Specimen PF1 was the first one tested and determined that lateral bracing was not effective. The remaining three specimens consisted of variation of plate thicknesses throughout the flanges and webs and requires elaborate modeling to those of the selected six.

Experimental configuration and system loading are depicted in Figure 5.1. Each rafter specimen was tested in an upside-down position such that the top flange, which was laterally more closely braced by simulated purlins, represented the outer flange in a real building. By adjusting the bracing locations of the inner flange, a controlling segment resulted. Each rafter was bolted to a reusable loading column through an end-plate moment connection. OpenSees simulation with the proposed beam-column element was based on the same configuration. The corresponding elevation views and geometry for the

[a] Controlling segment refers to the unbraced segment which is intentionally designed to experience lateral-torsional buckling in seismic design.

specimens are seen in Figure 5.2 through Figure 5.2 along with their specimen designation. It is seen that Specimens CF1, CF2, and CF2-A have CS within the first unbraced length from the loading column, while Specimens CS1, CS1-A, and CS2 have CS within the second unbraced length from the end-plate moment connection.

Each specimen was built up from three separate plates, each of which carried individual material properties (see Table 5.2 & Table 5.3). For simplicity, modeling of these varying material properties were not taken into consideration in the OpenSees modeling. Since these specimens were designed to experience LTB in the controlling segment of the inner flange, properties corresponding to the inner flange of the rafters were assumed for all three plates of each specimen. Yielding and ultimate strengths obtained through tensile testing of steel coupons were then used to form a bilinear material model required for the OpenSees simulations. Values of yielding and ultimate strength of each specimen's inner flange plate is tabulated on Table 5.2.

Initial out-of-plane geometric imperfections were incorporated for the numerical models which were obtained through measurements prior to experimental testing. Half of a sine wave pattern was assumed throughout the CS of a rafter such that the maximum imperfection value would be located at the mid-span of the CS. Values of these imperfections are tabulated in Table 5.4. Additional to imperfections, residual stresses were also incorporated to the numerical models. Although true residual stress patterns were unknown for the specimens, residual stress patterns found in Prawel et al. (1974) were assumed. Representation of this stress pattern is seen in Figure 4.32.

Testing consisted of cyclic loading up to and beyond buckling and often until rupture or tearing of the rafter through the loading sequence found in Section K2.4b of AISC-341 (AISC 2010b) as a base template. Each test began with a series of introductory loading cycles categorized by the displacement ratio:

$$\mathrm{DR} = \frac{\Delta}{120 \text{ in.}} \tag{5.1}$$

where Δ was the displacement measurement of D1. The beginning portion of the loading protocol consisted of:

- 6 cycles at $\pm$0.375% DR
- 6 cycles at $\pm$0.5% DR
- 6 cycles at $\pm$0.75% DR
- 4 cycles at $\pm$1.0% DR
- 2 cycles at $\pm$1.5% DR

Table 5.1 Test Matrix

Specimen	Taper Angle	CS[a,b]		Notes:
		Flange	Web	
CF1	4.60°	C	S	constant taper, no transitions, full CS 2-sided weld, CS = 1st unbraced length, welded brace clips
CF2	4.60°	C	S	constant taper, no transitions, CS = 1st unbraced length, welded brace clips, slot in web
CF2-A	4.60°	C	S	constant taper, no transitions, axial load, CS = 1st unbraced length, welded brace clips, slot in web
PF1	9.59°	C	S	pinch point at end of CS, CS = 1st unbraced length, welded brace clips
PF2	14.48°	C/N	S	pinch point within CS, CS = 1st unbraced length, welded brace clips
CS1	5.62°	N	N	constant taper, no transitions, CS = 2nd unbraced length, bolted brace clips
CS1-A	5.62°	N	N	constant taper, no transitions, axial load, CS = 2nd unbraced length, bolted brace clips
CS2	4.60°	N	S	constant taper, flange splice, CS = 2nd unbraced length, bolted brace clips
CS3	4.60°	C/N	S	constant taper, flange splice and thickness change, CS = 2nd unbraced length, welded brace clips
CS4	4.60°	N	S	constant taper, shear stiffeners, CS = 2nd unbraced length, welded brace clips

a CS = Controlling Segment
b C = Compact, N = Non-Compact, S = Slender

Table 5.2 Mechanical Characteristic of Steel

Coupon ID	Specification	Thickness (in.)	F_y (ksi)	F_u (ksi)	Elong. (%)
A	A529 Gr. 55	0.498 (0.500)[a]	60.0 (62.5)[b]	87.3 (87.3)	31.5[c]
B	A529 Gr. 55	0.318 (0.313)	69.7 (72.4)	94.4 (94.3)	27.4
C	A529 Gr. 55	0.257 (0.250)	69.8 (75.0)	98.3 (97.8)	23.4
D	A529 Gr. 55	0.370 (0.375)	57.6 (62.7)	86.0 (84.9)	29.0
E	A1018 HSLAS Gr. 55	0.307 (0.313)	54.5 (60.0)	80.8 (75.9)	30.4
F	A529 Gr. 55	0.254 (0.250)	61.6 (66.2)	87.8 (86.0)	27.7
G	A529 Gr. 55	0.318 (0.313)	67.0 (72.4)	95.4 (94.3)	26.1
H	A529 Gr. 55	0.244 (0.250)	67.9 (70.6)	95.1 (91.7)	23.3
I	A529 Gr. 55	0.310 (0.313)	55.6 (59.3)	83.6 (91.6)	28.0
J	A529 Gr. 55	0.369 (0.375)	62.5 (64.0)	88.9 (85.0)	28.6
K	A1011SS Gr. 55	0.186 (0.188)	71.9 (58.2)	80.7 (87.0)	26.8
L	A1011SS Gr. 55	0.185 (0.188)	61.9 (59.5)	87.8 (89.5)	24.8
M	Not Specified	0.166 (0.164)	66.7	81.2	24.8
N	A1011SS Gr. 55	0.150 (0.150)	58.1 (59.0)	85.0 (87.8)	23.3
O	A572/A1018 HSLAS Gr. 55	0.245 (0.250)	62.1 (62.7)	73.4 (76.0)	31.2
P	A1011SS Gr. 55	0.184 (0.188)	57.4 (62.4)	85.9 (91.0)	25.5

a Values in parentheses are nominal plate thicknesses from design drawings
b Values in parentheses are based on mill certified test reports.
c Elongation values are based on test results of coupons with 2 in. gage length.

Table 5.3 Rafter Material Index

Rafter ID	Inner Flange 1	Inner Flange 2	Outer Flange 1	Outer Flange 2	Web 1	Web 2
CF1	J	-	A	-	L	-
CF2	D	-	D	-	K	-
CF2-A	D	-	D	-	K	-
PF1	J	-	J	-	L	-
PF2	I	H	H	-	P	N
CS1	F	-	F	-	O	-
CS1-A	F	-	F	-	O	-
CS2	C	-	C	-	L	-
CS3	J	B	J	G	L	-
CS4	E	-	E	-	K	M

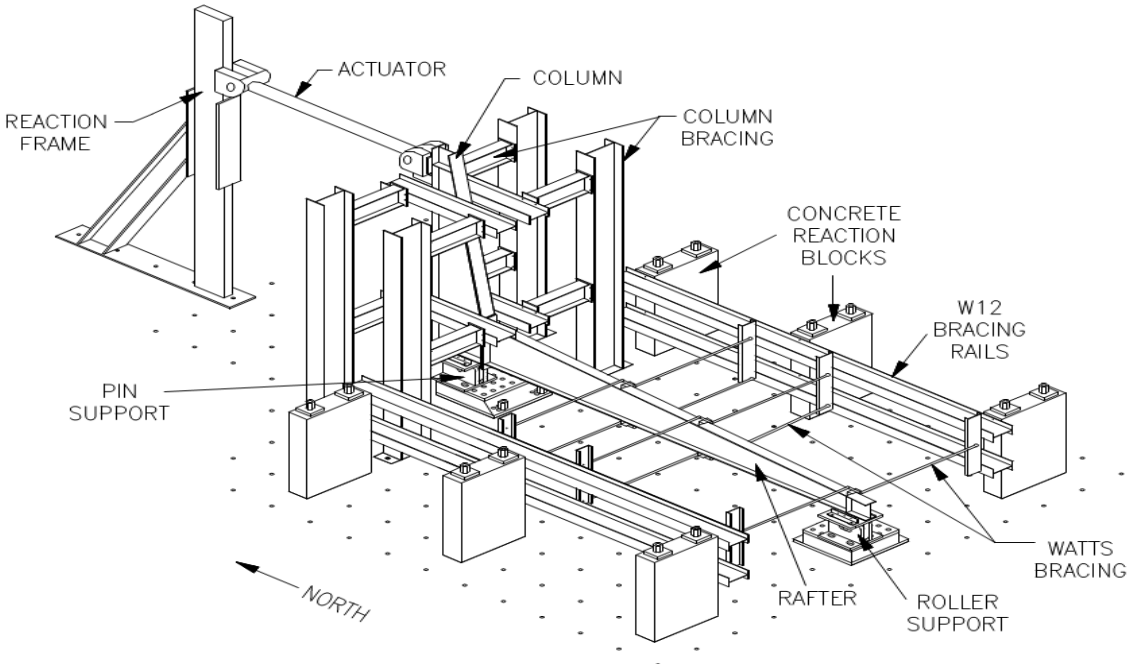

(a) Isometric View

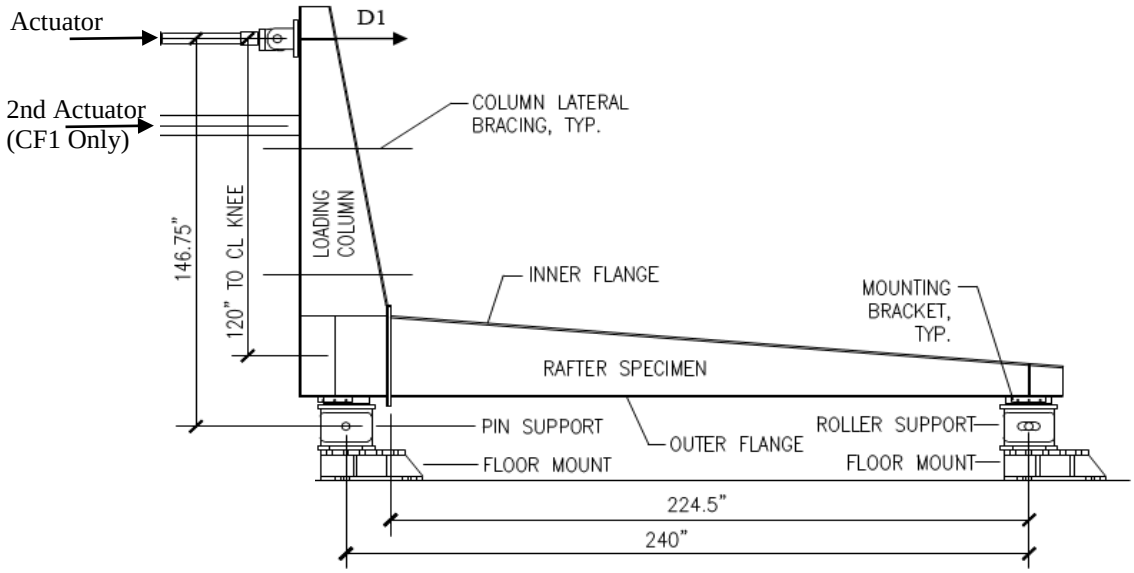

(b) Elevation

Figure 5.1 Test Setup Configuration

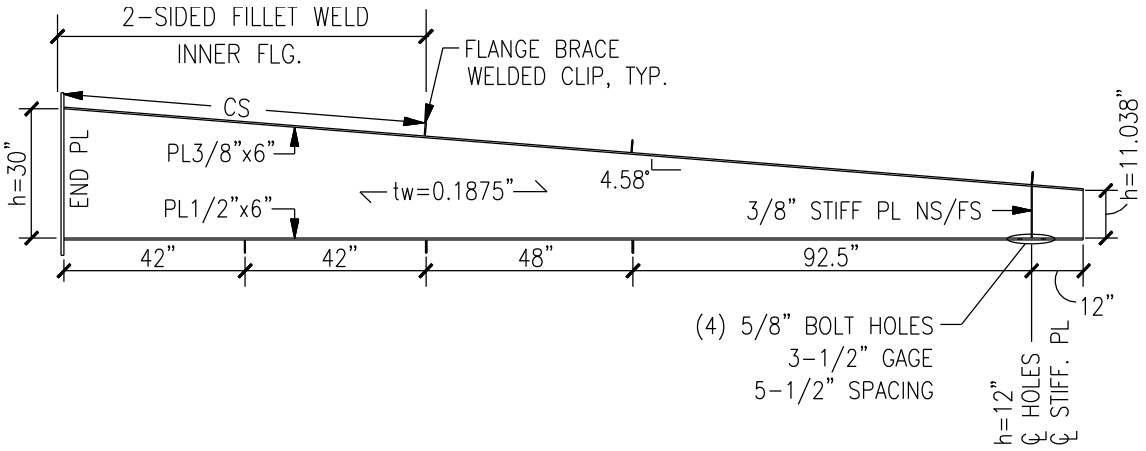

(a) Specimen CF1

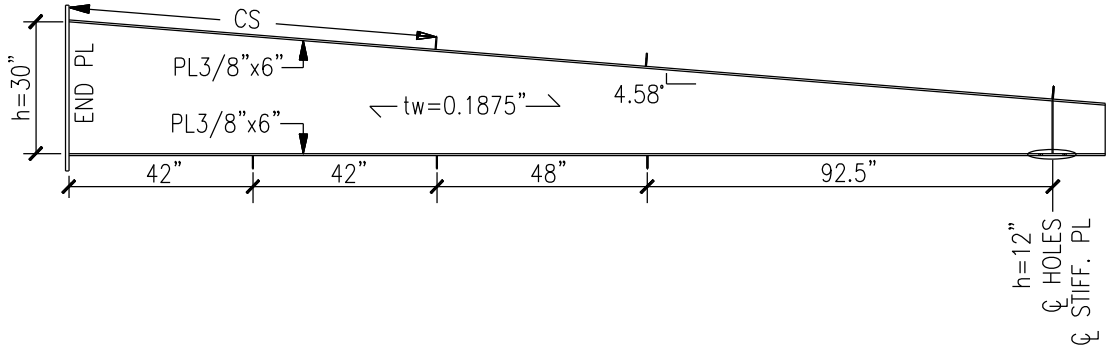

(b) Specimens CF2 & CF2-A

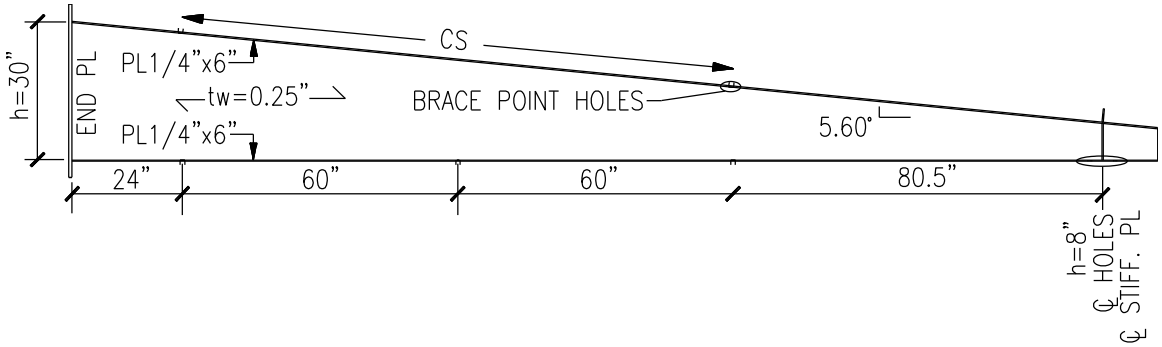

(c) Specimens CS1 and CS1-A

Figure 5.2 Specimen Geometry of CF1, CF2, CF2-A, CS1, CS1-A, and CS2

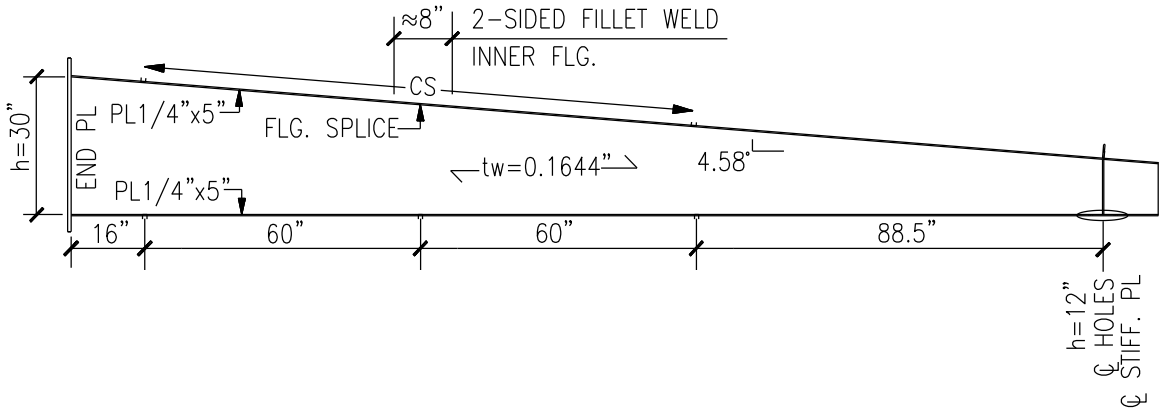

(d) Specimen CS2

Figure 5.2 Specimen Geometry of CF1, CF2, CF2-A, CS1, CS1-A, and CS2, continued

Table 5.4 Specimen Peak Imperfection Values

Specimen	Δ_0 (in.)	Δ_0/L^*_{CS}
CF1	0.028	1/1024
CF2	0.064	1/1312
CF2-A	0.028	1/3000
CS1	0.060	1/2000
CS1-A	0.060	1/2000
CS2	0.075	1/1600

*L^*_{CS} = length of controlling segment

5.2 Specimen CF1

This specimen had the CS next to the column. The flanges and web were classified as compact and slender, respectively, in accordance with AISC 360 (AISC 2010a). The inner flange of the CS first experienced LTB during the +3.6 in. excursion. Flange local buckling (FLB) was visible during the +4.8 in. excursion (see Figure 5.5). upon load reversal, high-strength bolts connecting the rafter end-plate to the loading column ruptured during the -4.8 in. excursion. Figure 5.3(a) shows the measured response.

The global response predicted by using the proposed beam-column element is shown in Figure 5.3(b), and a composite plot showing the correlation to the experimental data is shown in Figure 5.3(c). It was observed that the elastic stiffness correlated very well with the test data. First LTB was observed to occur in testing during the +3.6 in. excursion, but such phenomenon was not predicted in the analysis. LTB was well predicted during the +4.8 in. excursion. The composite plot in Figure 5.3(c) shows a more significant strength degradation in the post-buckling region, probably due to the FLB which was not considered in the proposed element.

The same cyclic analysis for CF1 was simulated using the existing beam-column element implemented in OpenSees. Comparison of the load-displacement plots of these two elements are shown in Figure 5.4. Once LTB occurs, the existing element buckles pre-maturely with respect to the proposed element and experimental data. This is due to the lack of supplementary effects, such as the Wagner effect mentioned in Chapter 2. Thus, conclusion can be made that incorporation of the extra warping DOF is essential for instances of lateral-torsional buckling.

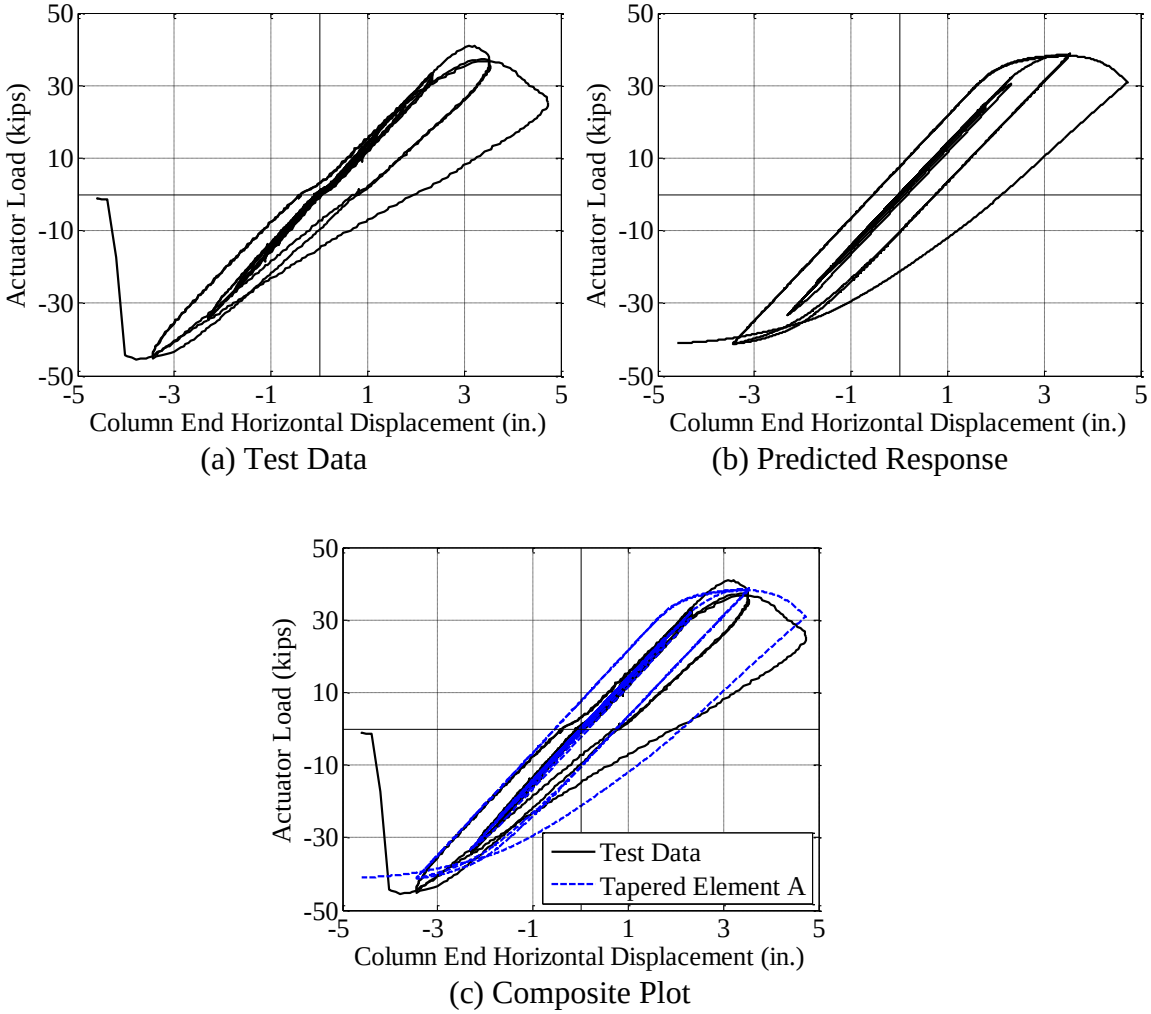

Figure 5.3 Specimen CF1: Load vs. Column End Horizontal Displacement

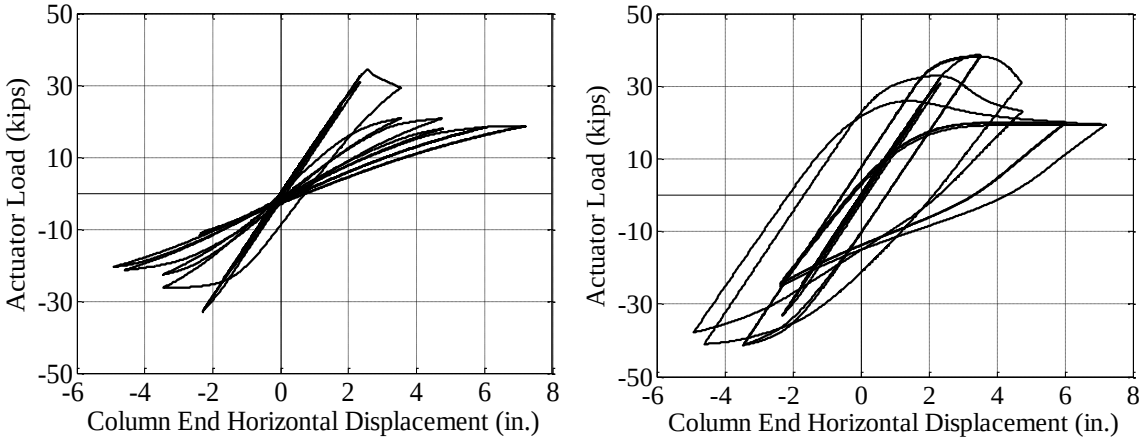

(a) Based on Existing Element (b) Predicted Response

Figure 5.4 Specimen CF1: 6 DOF vs. 7 DOF Beam-Column Element

(a) LTB (b) FLB

Figure 5.5 CF1 Post-LTB Flange Local Buckle in CS (+4.8 in.)

5.3 Specimen CF2

Geometry and configuration of Specimen CF2 was almost identical to that of Specimen CF1. Difference between the two specimens are seen in the use of plates for the outer flange as CF2 uses a thinner (3/8 in.) plate thickness opposed to 1/2 in. All except Specimen CF1 used one-sided fillet weld to connect the web to the flanges. Therefore, it was expected that the residual stress distribution and initial geometric imperfection would also be different (Prawel et al. 1974), although in the analysis the same residual stress pattern was used for the models.

A comparison of the experimental and predicted responses is presented in Figure 5.6[b]. The specimen experienced LTB during the first excursion to +4.8 in., which was predicted by the analysis. However, the strength degraded much faster upon the first LTB during the test, probably because of FLB which accompanied LTB (see Figure 5.8), yet FLB was not considered in the analysis. During the three excursions to +4.8 in., however, the analysis did reflect progressive strength degradation due to residual out-of-plane deformations from prior LTB.

A pushover analysis was also conducted, and the predicted response curve would overpredict response envelope of the cyclic response in the post-buckling region (see Figure 5.7). The specimen also experienced FLB when excursing to -3.6 in. and -4.8 in and caused a degradation in strength, which again was not reflected in the analysis.

[b] Additional loading which caused the web to separate from the inner flange at the first welded location was not included in the comparison.

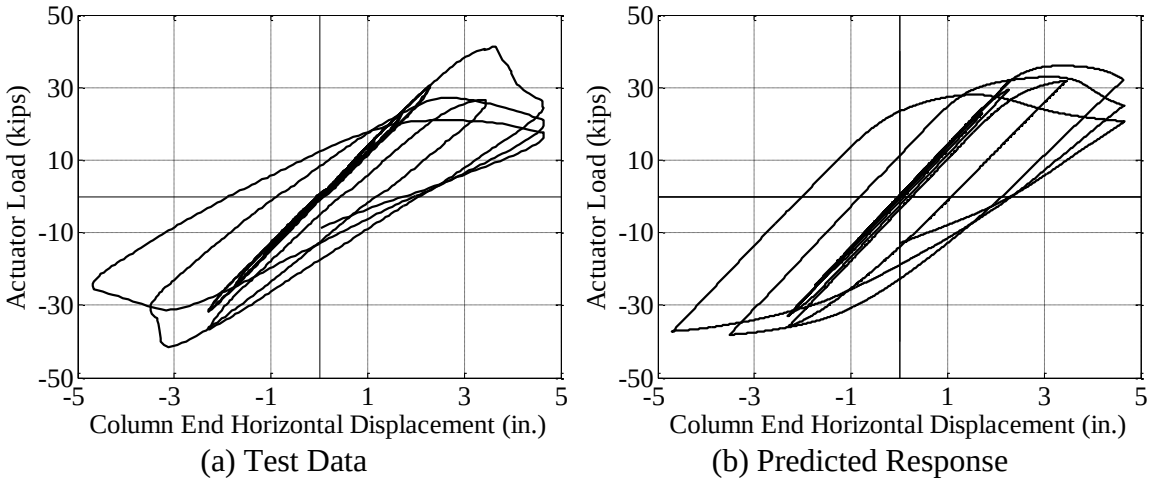

Figure 5.6 Specimen CF2: Load vs. Column End Horizontal Displacement

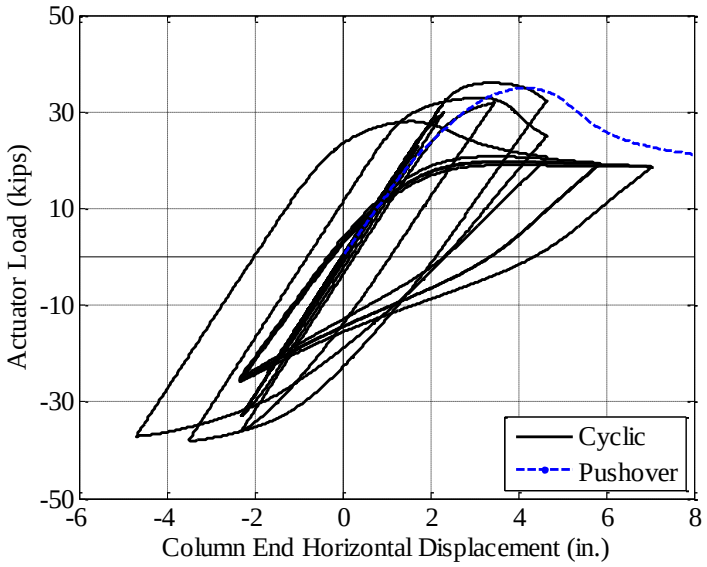

Figure 5.7 Predicted Responses of Cyclic and Pushover Analyses

(a) LTB

(b) FLB

Figure 5.8 CF2 Initial Buckling of Inner Flange (+4.8 in., 1st Cycle)

5.4 Specimen CF2-A

Specimen CF2-A was nominally identical to CF2, except that a constant axial load of 28.4 kips was applied collinear to the centroidal axis of the rafter prior to cyclic loading. The CS for this specimen was located at the first unbraced segment from the end-plate connection.

A comparison of the experimental and predicted responses is presented in Figure 5.9[c]. The specimen experienced LTB during the first excursion to +3.5 in. During the excursion of initial LTB, the CS displaced laterally by 1.4 in. at the midspan and also experienced two cases of FLB (see Figure 5.11). Event of this combined buckling mode resulted into a significant degradation in strength. Analysis results was able to capture occurrence of LTB during the first excursion of +3.5 in., although peak strength of the cycle yields less than that of the test. The analysis was unable to capture the loss of strength once LTB occurs since effects of local buckling are neglected. The second cycle of 3.5 in. is seen in the test to have a significant strength degradation compared to the first cycle, whereas analysis shows a small loss of strength after the first cycle.

During the excursion to -3.5 in. of the first cycle, occurrence of FLB at the outer flange took place during the test. Results obtained from analysis with the proposed element was unable to capture this mode of buckling.

A comparison of the test response of Specimen CF2 in Figure 5.6(a) and that of Specimen CF2-A in Figure 5.9(a) shows that the presence of an axial load produced a much

[c] Response after the second ±3.5 in. was excluded due to FLB rupture occurring at the outer flange of the specimen.

rapid strength degradation upon buckling; such degradation was caused by not only LTB but also simultaneous FLB. Although the proposed Tapered Element A cannot consider FLB, the effect of axial load on the global response was studied by comparing the predicted responses of three cases:

- Case 1: P = 0 kips (similar to CF2)
- Case 2: P = 28.4 kips (similar to CF2-A)
- Case 3: P = 56.8 kips

The response comparison of all these cases are seen in Figure 5.10. Global response of all three cases show that strength degradation after buckling becomes more significant as the axial load is increased. Although buckling is observed to occur even in the case of no axial load (Case 1), strength degradation does not show to be significant within the two cycles of 3.5 in. Analysis of CF2-A with the tested axial load (Case 2) is seen to have less peak strength during the second cycle of 3.5 in. on the positive excursion compared to Case 1. Although strength degradation is more apparent in this case, significant loss of strength is not established until the first excursion of +4.5 in.

When the axial load was doubled from that of Case 2, Specimen CF2-A showed a clear sign of buckling occurring within the first excursion of +3.5 in. The second cycle of 3.5 in. of Case 3 resulted in a significant drop of strength which is clearly distinguishes itself from the other two cases. Subsequent cycles of 4.5 in. displacement showed peak loads of these cycles were much lower after the second cycle of +3.5 in. Member strength at the second +4.5 in. excursion suggests minimal strength degradation, especially when compared to Case 2 where a substantial loss of strength is seen at this displacement.

Although both results of Case 2 and Case 3 show initial LTB occurring during the first excursion of +3.5 in., post-buckling responses throughout the remaining cycles show significant differences. The response behavior seen by Case 3 show to resemble similar trend of strength degradation as the first excursion of +3.5 in. of testing.

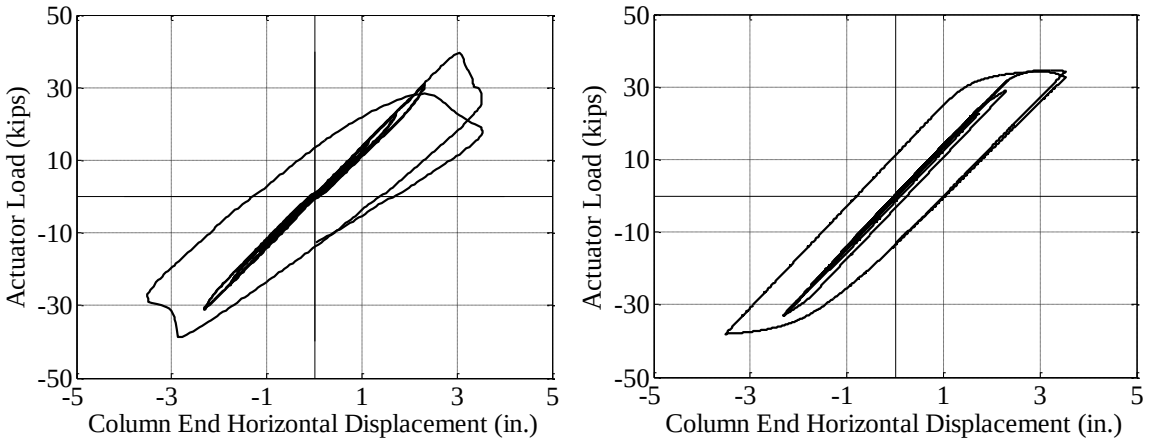

(a) Test Data (b) Predicted Response

Figure 5.9 Specimen CF2-A: Load vs. Column End Horizontal Displacement

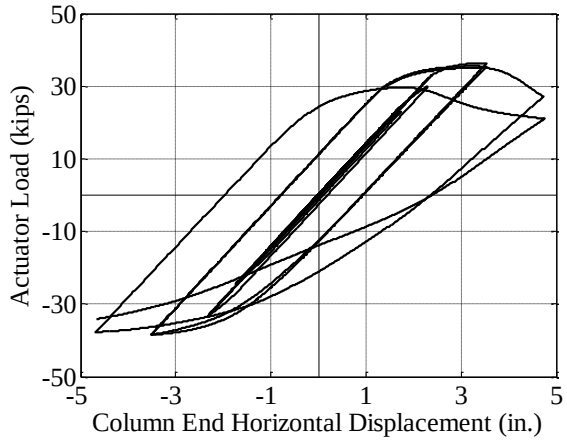

(a) Case 1: P = 0 kips

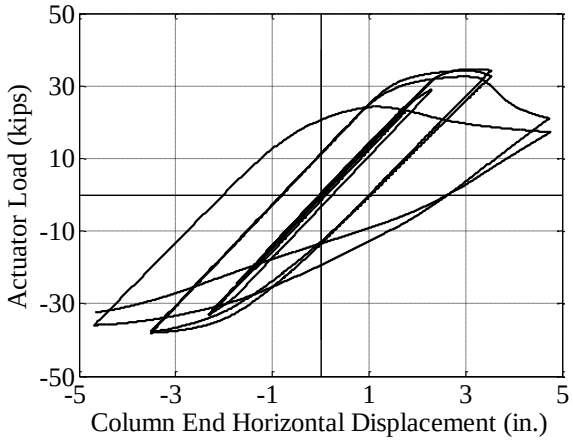

(b) Case 2: P = 28.4 kips

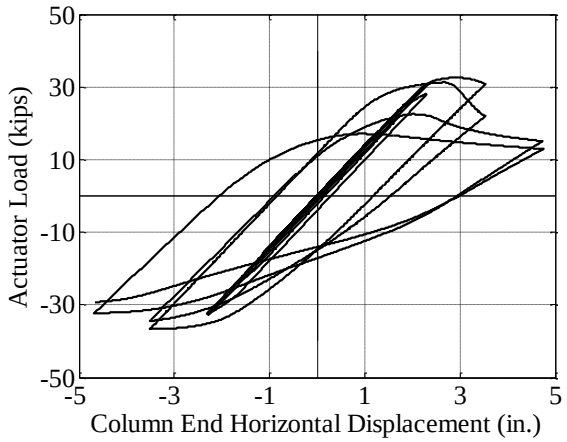

(c) Case 3: P = 56.8 kips

Figure 5.10 CF2-A Analysis Response of Varying Axial Loads

(a) LTB

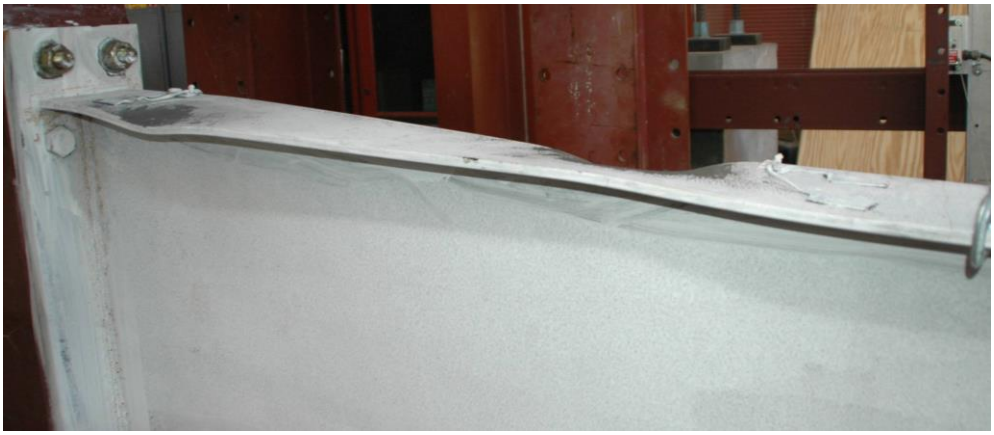

(b) FLB

Figure 5.11 CF2-A Initial LTB (+3.5 in., 1st Cycle)

5.5 Specimen CS1

Specimen CS1, consisted of a larger web-taper [Figure 5.2(c)] than any of the other five specimens. Unlike the previous specimens, the CS of this specimen began at the second unbraced segment (i.e., 24 in. away from the end-plate connection). This specimen, as well as the remaining two, had the longest unbraced length (L_{CS} = 120 in.) for the CS. Both the flanges and web of the specimen were classified as noncompact.

A comparison of the experimental and predicted responses is presented in Figure 5.12[d]. The specimen experienced LTB during the first excursion to +3.6 in. Figure 5.14 shows that the CS displaced laterally by 4 in. at the midspan, which also triggered FLB. This combined buckling mode resulted in a significant degradation in strength. The analysis showed that LTB occurred during the second, not first cycle. The load at which LTB developed was similar (30.6 kips from testing versus 32.2 kips from analysis). The specimen experienced combined FLB and WLB (web local buckling) modes during the excursion to -4.78 in (see Figure 5.15), which could not be simulated by the proposed element.

Although separation of the web from the flanges at the severely buckled location occurred after completing one cycle at 4.8 in. test, the analysis continued to $\pm$6.0 in. Figure 5.13 shows that, in the post-buckling region, for each of the 4.8 in. and 6.0 in. cycles, the strength degraded only slightly from the first to the second cycles for this long CS.

[d] Response after the first cycle at $\pm$4.8 in. was excluded due to the separation of web from the flanges at the severely local buckled region.

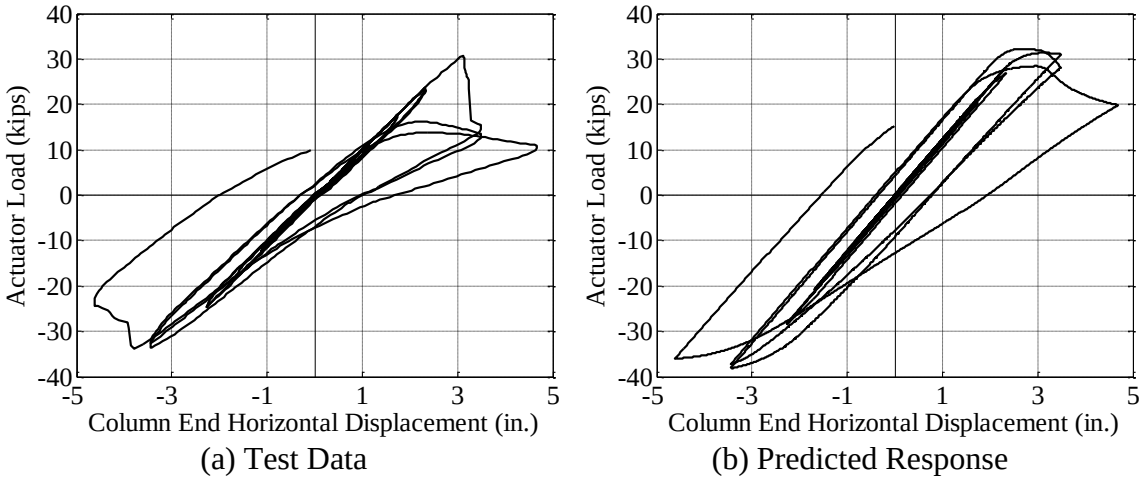

Figure 5.12 Specimen CS1: Load vs. Column End Horizontal Displacement

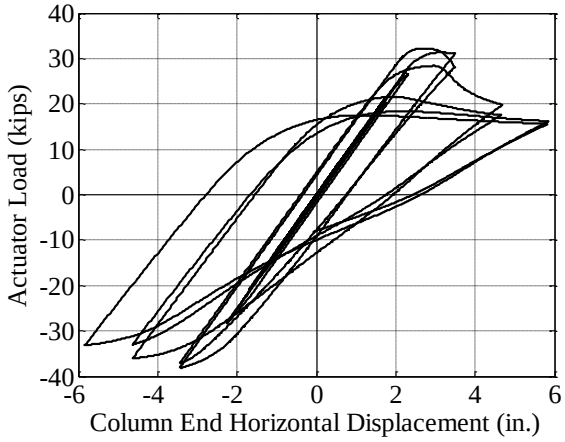

Figure 5.13 Predicted Analysis of Full Cyclic Behavior of CS1

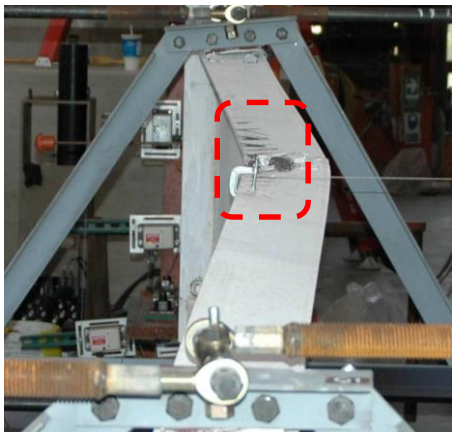

(a) LTB

(b) Inner Flange FLB at Mid-Length of CS

Figure 5.14 CS1 Initial LTB in CS (+3.6 in., 1st Cycle)

Figure 5.15 CS1 Outer Flange FLB and WLB (-4.8 in., 1st Cycle)

5.6 Specimen CS1-A

Geometry of CS1-A was nominally identical to CS1, except that a constant axial load of 41.7 kips was applied collinear to the centroidal axis of the rafter prior to cyclic loading. The test response in Figure 5.16(a) shows that the specimen experienced buckling during the first cycle at $\pm$3.5 in. The specimen first experienced LTB during the positive excursion. Figure 5.17 (a) shows the LTB as well as the accompanying FLB at the midspan of the CS. In addition, another FLB also occurred near the bracing point nearest to the end-plate connection as shown in Figure 5.17(b). Once the loading direction was reversed, the outer flange also buckled (see Figure 5.18). Once both the inner and outer flanges experienced LTB and FLB, the presence of an axial load triggered global flexural-type buckling during the second cycle (see Figure 5.19).

The analysis result in Figure 5.16(b) shows that LTB during the first excursion to +3.5 in. was simulated, but the amount of strength degradation, probably due to FLB at two locations, was significantly under-estimated. However, LTB that was observed during the -3.5 in. excursion was not predicted in the analysis. Also, the global flexural-type buckling observed during the second cycle at 3.5 in. was not predicted by the analysis.

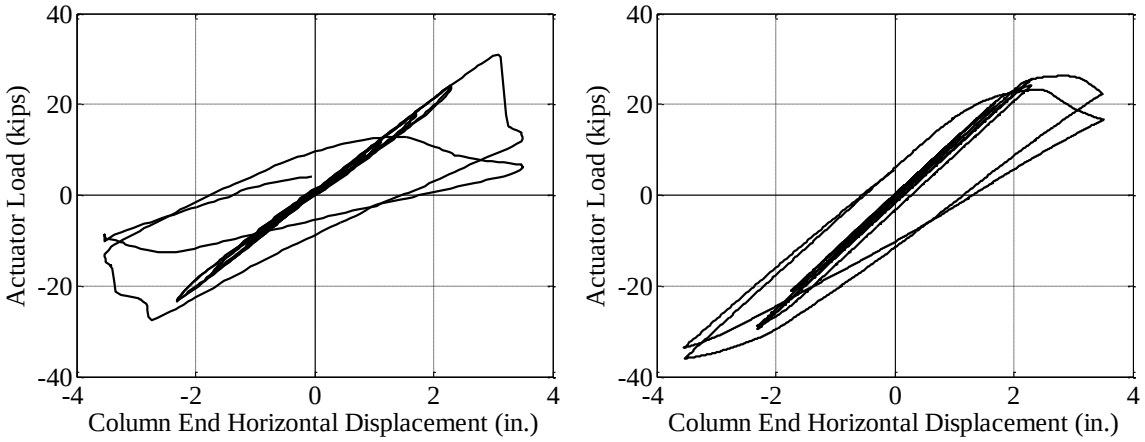

(a) Test Data (b) Predicted Response

Figure 5.16 Specimen CS1-A: Load vs. Column End Horizontal Displacement

(a) LTB (b) Initial FLB at Mid-Length of CS

Figure 5.17 CS1-A Initial LTB (+3.5 in., 1st Cycle)

(a) LTB (b) FLB at Mid-Length

Figure 5.18 CS1-A Outer Flange Buckling (-3.5 in, 1st Cycle)

(a) Inner Flange LTB (b) Outer Flange LTB

Figure 5.19 CS1-A LTB (3.5 in., 2nd Cycle)

5.7 Specimen CS2

Specimen CS2 has the same web-taper characteristics as the previously mentioned specimens, with the exception of CS1 and CS1-A. Construction of the specimen, however, involved an inner flange splice located at the mid-length of the CS and a web splice located at the small end of the CS. In addition to the CJP welds used for these splices, fillet welds were used on both sides of the web within the vicinity of the splice, while the rest of the specimen consisted of one-sided fillet weld between the web and flanges. The flanges and web of the rafter were classified to be noncompact and slender, respectively.

A comparison of the experimental and predicted responses is presented in Figure 5.20[e]. The specimen experienced LTB during the first excursion to +3.5 in. Along with initial LTB, formation of FLB at the mid-length of the CS was noticed. Figure 5.21 shows the out-of-plane displacement at the end of the first +3.5 in. excursion was 5 in. Soon after LTB occurred, significant strength degradation was noticed during the test. Response from the analysis overpredicted the initial LTB strength slightly (23.1 kips in test versus 25.3 kips in analysis). But it failed to capture the same rate of strength degradation, again because local buckling was not considered in the analysis.

During the first negative excursion of -3.5 in., combined WLB and FLB occurred in the outer flange at the second brace point (see Figure 5.22). This occurrence of local buckling caused a significant loss of strength, which was not captured by the proposed beam-column element in the analysis.

---

[e] Response after the second $\pm$3.5 in. cycle was excluded due to bolt hole rupture of the inner flange brace point at 4.8 in. cycle and a longitudinal separation of the inner flange at the brace later.

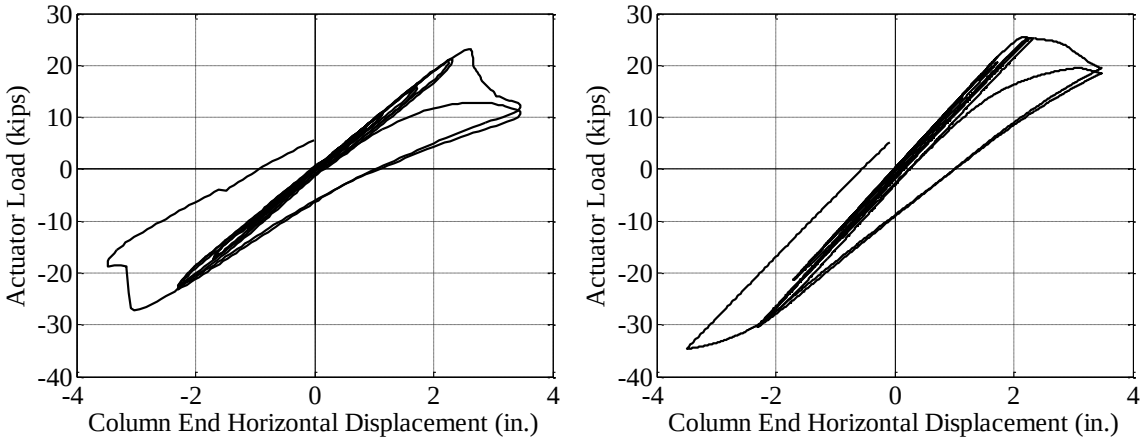

Figure 5.20 Specimen CS2: Load vs. Column End Horizontal Displacement

Figure 5.21 CS2 Initial Buckling of Inner Flange (+3.5 in., 1st Cycle)

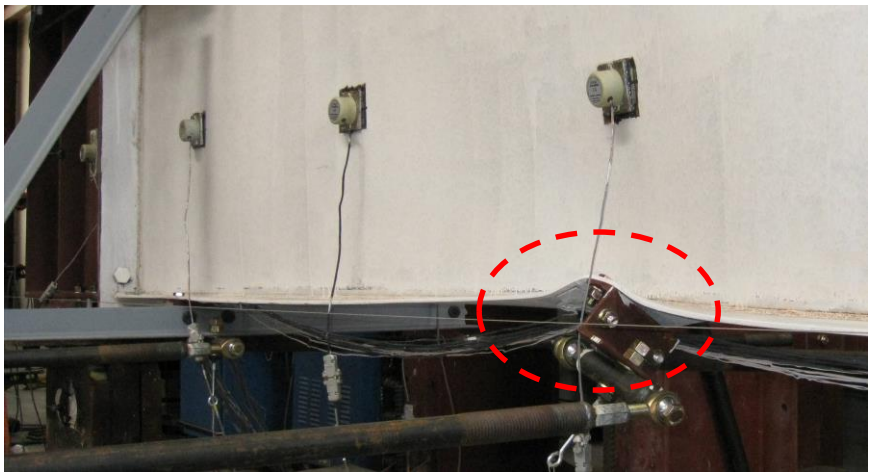

Figure 5.22 CS2 Outer Flange FLB (-3.5 in., 1st Cycle)

5.8 Assessment of Results

Results for all six specimens showed that numerical studies with the proposed beam-column element in OpenSees is limited. With the exception of Specimen CF1, events of initial LTB for the tested specimens showed simultaneous buckling modes of FLB taking place along the CS. Combined modes of LTB and FLB during the occurrence of initial LTB subsequently resulted to an immediate loss of strength during the remaining portion of that excursion. Analysis response of the specimens showed to capture initial LTB similar to testing. Strength degradation of these analyses, however, show to be decrease gradually to the equivalent counterpart from testing. These results suggest that effects of strength degradation, seen in testing, are dependent on LTB as well as FLB. Because of this, assessment of results prior to initial LTB are focused on.

Comparison of peak loads observed at initial LTB of both testing and analysis are reported in Table 5.5. Overall assessment of these loads obtained from analysis show to match up with testing within a tolerable discrepancy to that of testing. With the Exception of specimens CS1 and CS2, initial LTB captured by the proposed element are conservative

to the experimental counterpart. Specimen CS1-A is seen to have the highest error to the cyclic testing causing nearly a 22% under-predicted peak load while CS1 (equivalent specimen to CS1-A with no axial load) only yielded just over 5% over-predicted peak load. Possible explanation to such an error may be from the high web-taper, relative to all other specimens, that CS1-A had in addition to the axial load applied.

Pushover analyses were modeled using the proposed beam element and compared to the cyclic analyses counterparts. Results of peak loads obtained from both cyclic and pushover analysis at the occurrence of LTB is reported in Table 5.6. Critical values seen between the two data sets are seen to yield no more than 10% difference of peak load. Similar to the post-buckling response of the cyclic analyses in OpenSees, pushover response did not capture the rapid strength loss after initial LTB as seen for Specimen CF2 in Figure 5.7.

It is also observed that CS2 consists of a flange splice as well as two-sided welds throughout the CS. It is not entirely clear on how the changes of welding effect residual stresses, hence possibly leading to the simulated response. Due to the stiffer responses, the critical load that initiates LTB is over predicted and occurs at a smaller displacement compared to testing. Similar to Group 1, the rapid strength degradation due to combined FLB and LTB are not represented within the numerical results.

A study of initial imperfection implications was done through Specimen CS2. In addition to the initial imperfection used from measurements reported in testing, two more analyses consisting different imperfections along the CS were modeled. Classification of these three studies based on the initial imperfection values of:

- Case 1: Δ_0 = 0.14 in. (similar to measured initial imperfection of CS2)
- Case 2: Δ_0 = 0.07 in. (half the initial imperfection of Case 1)
- Case 3: Δ_0 = 0.28 in. (double the initial imperfection of Case 1)

Complete response for each case of varying initial imperfections are seen in Figure 5.23. Assessment of the overall cyclic analyses suggest that variation of the initial imperfection imposed along the CS does not yield significant, or any, differences in initial buckling and post-buckling response. Observed peak load at initial buckling for both case 2 and case 3 showed to be very minimal in difference compared to that of Case 1. Observed loads at initial LTB for Case 2 and Case 3 are compared to Case 1 and reported in Table 5.7. Conclusion of these results suggest variation in initial imperfections along the CS does not play a significant role in overall cyclic response behavior.

Additional studies for Specimen CS2 were done to better understand cyclic behavior undergoing different residual stresses. Prawel et al. (1974) tested web-tapered specimens which were assembled by using one-sided fillet welds at the web and flange connections. A suggested self-equilibrating residual stress pattern was provided by Prawel et al. and is seen in Figure 4.32. Because the cyclic tested specimens performed in this study also involved one-sided fillet welds at the web and flange connections, similar use of this residual stress pattern was used for analysis. Variation of this pattern was done by using 50% and 80% of the suggested residual stresses by Prawel et al. for Specimen CS2. Different cases of varying residual stress patterns are classified as:

- Case 1: original residual stresses suggested by Prawel et al. (1974)
- Case 2: 80% of the residual stresses of Case 1
- Case 3: 50% of the residual stresses of Case 2

Complete analysis response of all three cases are seen in Figure 5.24. Unlike the case studies done with initial imperfections, cyclic response is significantly affected through use of different residual stresses. Initial observations show that decreased residual stresses (i.e., Case 2 and Case 3) show greater member strength prior to initial LTB. Additionally, strength degradation of the latter cases are seen to be more apparent throughout the remaining portion of the +3.5 in. excursion. A similar increased strength is seen in the negative excursion to -3.5 in. of the first cycle as residual stresses are decreased. Post-buckling behavior of the remaining cycles following initial LTB show little to no difference throughout all three cases. Peak loads for Case 2 and Case 3 during initial LTB are reported in Table 5.8. Comparison of these values to Case 1 show the significant strength gained as residual stresses are decreased.

Kim (2010) ran simulations of buckling analyses involving various residual stress patterns through ABAQUS. These models were simulated to run analyses up to the buckling load of a system with no results of post-buckling response. Same use of the Prawel et al. (1974) residual stresses were one of the residual stresses tested in her models. Similar conclusions are made with the three cases of residual patterns used for specimen CS2. Use of the pure self-equilibrating stress patterns suggested by Prawel et al. have shown to yield conservative buckling loads to the tested specimens as mentioned by Kim. Alteration of these patterns though show an increase of strength as well as altered strength degradation response following initial LTB. Overall post-buckling behavior remains unaffected by the use of residual stresses as seen from the case study of CS2.

Although the proposed element shows to capture initial LTB fairly well relative to testing, it was observed that significant strength degradation is also contributed to FLB in

addition to LTB. Because the current proposed element is unable to capture local buckling effects, correlation between testing and the predicted analyses show significant deviation throughout the remaining cyclic response. Studies to assess the effects and implications of initial imperfections and residual stresses were performed. Conclusions from these studies show that imperfections take no part in overall cyclic behavior while residual stresses affect initial and post-buckling behavior of an analysis. Remaining cycles subsequent to initial LTB, however, are minimally, if at all, affected by these residual stresses. Even though these residual stresses show to play a significant part in strength degradation following initial LTB, consideration of local buckling effects must be studied and incorporated to the proposed element.

Table 5.5 Peak Force at Initial LTB for Experimental and Numerical Results

Specimen	P_{max} (kips)		Error (%)
	Test	OpenSees	
CF1	40.8	38.6	-5.3
CF2	41.2	35.9	-12.7
CF2-A	39.4	34.5	-12.3
CS1	30.6	32.2	+5.2
CS1-A	31.6	24.2	-21.8
CS2	23.1	25.4	+10.1

Table 5.6 Peak Force at Buckling for Cyclic and Pushover Simulations

Specimen	P_{max}(kips)		Error (%)
	Cyclic	Pushover	
CF1	38.6	37.3	-3.3
CF2	35.9	34.8	-3.0
CF2-A	34.5	33.1	-4.0
CS1	32.2	28.9	-10.1
CS1-A	24.2	24.3	+0.1
CS2	25.4	23.2	-8.8

Table 5.7 Peak Loads at LTB of CS2 with Modified Initial imperfections

Amplification Factor of Measured Initial Imperfection	P_{max} (kips)	Error (%)
0.5	24.7	-3.0
2.0	25.9	+1.8

Table 5.8 Peak Loads at LTB of CS2 with Modified Residual Stresses

Modification Factor (%)	P_{max} (kips)	Error (%)
80	28.3	+11.3
50	30.8	+20.9

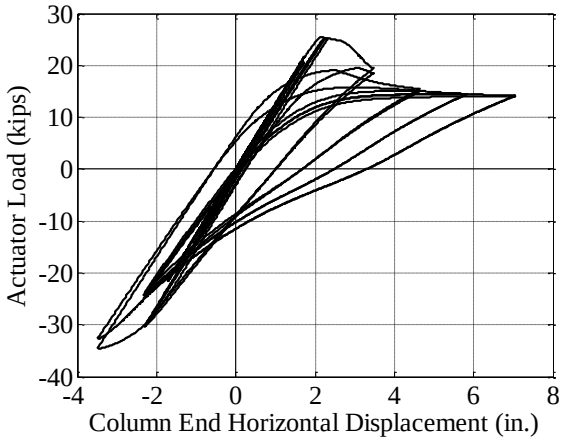

(a) Case 1: Δ_0 = 0.14 in.

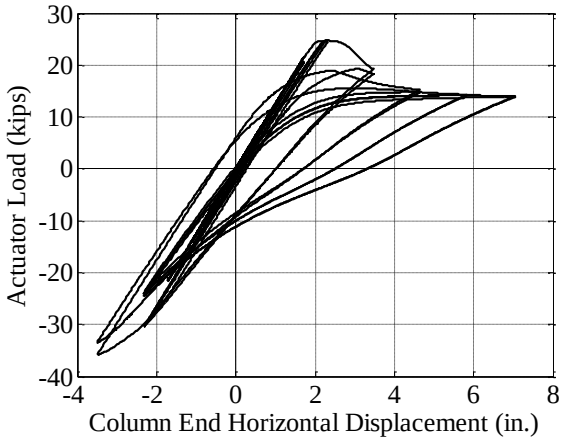

(b) Case 2: Δ_0 = 0.07 in.

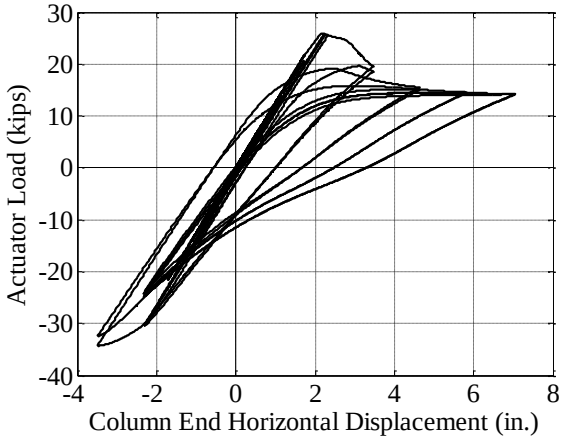

(c) Case 3: Δ_0 = 0.28 in.

Figure 5.23 Response of Initial Imperfection along Controlling Segment of CS2

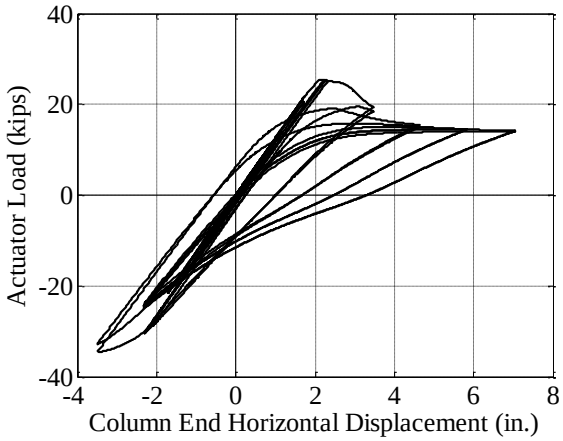

(a) Case 1: Original Residual Stress

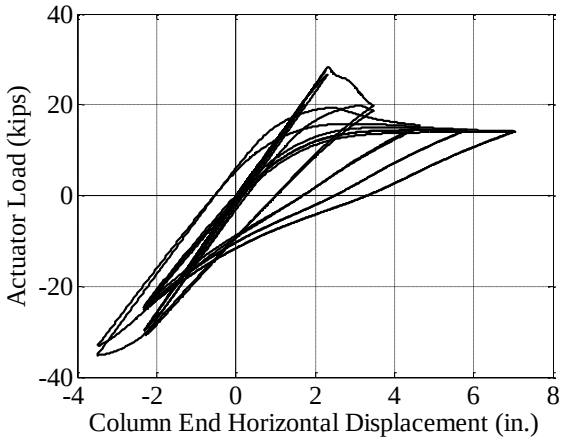

(b) Case 2: 80% of Original Residual Stress

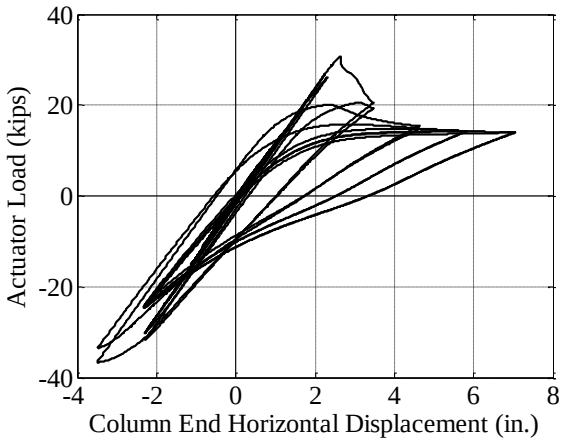

(c) Case 3: 50% of Original Residual Stress

Figure 5.24 Analysis Response of Residual Stresses on CS2

6 DEVELOPMENT OF TAPERED ELEMENT B

6.1 General

Although incorporation of a warping DOF shows reasonable correlation to experimental data, especially for members under monotonic loading, further development must be ensured in order to fully capture other buckling modes such as local buckling. Member buckling and local buckling are commonly handled to be independent of one another in design procedures. However, experimental testing, cyclic testing as presented in Chapter 5 in particular, has shown that the interaction between these buckling modes quite often occur simultaneously.

Utilization of the beam-column element (Tapered Element A presented in Chapter 2) is elaborated and expanded on in order to include local buckling effects in this chapter. Consideration of these effects requires additional DOFs that represent the top and bottom flange's rotations and curvatures. The proposed element, therefore, increases from 7 DOFs to 11 DOFs per element end node. Due to these additions, a single beam-column element consists of 22 DOFs in total. This concept of expanding Tapered Element A with additional DOFs are based off the work of Rajasekaran and Murray (1973). Throughout their work, it was shown that incorporation of plate theory concepts with the beam theory, discussed in Chapter 2, is able to couple local buckling with global buckling.

A physical representation of the proposed element with incorporation of the new DOFs is seen through Figure 6.1. As seen from the figure, the displacements are obtained and dependent on the flange's rotation about the longitudinal axis of the beam-column element. Correspondingly, the first derivative of the flange rotation, with respect to the

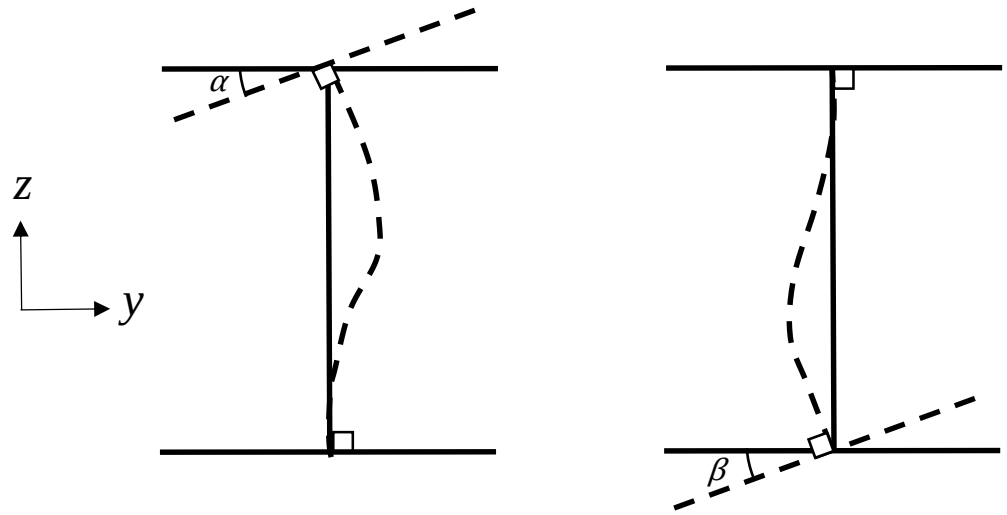

Figure 6.1 Incorporation of Rotation DOFs for Tapered Element B

beam-column longitudinal axis, represents the rate of change of this rotation along the member length. Analogously, this is similar conceptually to a beam with respect to its transverse displacement and corresponding slope. Because FLB is only represented at the end nodes of the proposed beam-column element, it is important to incorporate a sufficient number of elements to capture these events representatively.

The proposed element carries the assumption that the angle between adjacent component plates of the section remain perpendicular at the common edge during deformations. Hence, rotation of a flange carries the same rotation with the corresponding web plate edge as seen in Figure 6.1. Since rotation of the end of a web plate shares the same rotation with a corresponding flange, displacements of an arbitrary point on the web plate can be determined. From these relations, deformations of the web plate are dependent on flange deformation and considered to be coupled (i.e., WLB is coupled with FLB).

6.2 Element Tangent Stiffness Matrix

Development of the proposed beam-column element relies on the continuation of the beam theory discussed in Chapter 2. Since member global buckling is already taken into consideration through inclusion of the warping DOF, it stands to show that the additional four new DOFs will capture an element's local buckling. From these DOFs, a representation of each flange's rotation (Θ) and curvature (Θ') are to be captured at each element node (Rajasekaran and Murray 1973). Superimposing both beam theory displacements and the small deflections based on Kirchhoff's plate theory, displacements of a point on a cross-section can be determined.

In order to incorporate plate theory to the proposed element formulation, each flange and web plate are treated to have their own coordinate system. Hence, each plate has a displacement component of *u*, *v*, and *w* which can be determined through conventional plate theory. Convention used for a plate's rotation about its centroid for the top flange and bottom flange are $\alpha(x)$ and $\beta(x)$, respectively. Note that the positive rotation convention is based on a counter-clockwise direction for these DOFs. Due to the incorporation of the plate deformations, the displacement vector $\boldsymbol{q}_n$ previously defined in Eq. (2.1) is expanded to be:

$$\mathbf{q_n} = [\Theta_{1x} \quad \Theta_{1z} \quad \Theta_{1y} \quad \phi_1' \quad \Theta_{\mathbf{1}}^* \quad \Theta_{2x} \quad \Theta_{2z} \quad \Theta_{2y} \quad \phi_2' \quad \Theta_{\mathbf{2}}^* \quad e]^T \tag{6.1a}$$

$$\Theta_{\mathbf{1}}^* = [\alpha_1 \quad \alpha_1' \quad \beta_1 \quad \beta_1'] \tag{6.1b}$$

$$\Theta_{\mathbf{2}}^* = [\alpha_2 \quad \alpha_2' \quad \beta_2 \quad \beta_2'] \tag{6.1c}$$

Use of interpolation functions are again incorporated for the proposed element and utilize cubic Hermitian functions to determine the plate deformations. Therefore the flange rotations along an element's longitudinal axis can be determined through:

$$\alpha(x) = N_1\,\alpha_1 + N_2\,\alpha'_1 + N_3\,\alpha_2 + N_4\,\alpha'_2 \tag{6.2}$$

$$\beta(x) = N_1\,\beta_1 + N_2\,\beta'_1 + N_3\,\beta_2 + N_4\,\beta'_2 \tag{6.3}$$

Subsequent derivatives of Eqs. (6.2) and (6.3) are:

$$\alpha'(x) = N'_1\,\alpha_1 + N'_2\,\alpha'_1 + N'_3\,\alpha_2 + N'_4\,\alpha'_2 \tag{6.4}$$

$$\beta'(x) = N'_1\,\beta_1 + N'_2\,\beta'_1 + N'_3\,\beta_2 + N'_4\,\beta'_2 \tag{6.5}$$

$$\alpha''(x) = N''_1\,\alpha_1 + N''_2\,\alpha'_1 + N''_3\,\alpha_2 + N''_4\,\alpha'_2 \tag{6.6}$$

$$\beta''(x) = N''_1\,\beta_1 + N''_2\,\beta'_1 + N''_3\,\beta_2 + N''_4\,\beta'_2 \tag{6.7}$$

where

$$N_1 = 1 - 3\left(\frac{x}{L}\right)^2 + 2\left(\frac{x}{L}\right)^3 \tag{6.8}$$

$$N_2 = x\left(1 - \frac{x}{L}\right)^2 \tag{6.9}$$

$$N_3 = 3\left(\frac{x}{L}\right)^2 - 2\left(\frac{x}{L}\right)^3 \tag{6.10}$$

$$N_4 = -x\left(\frac{x}{L}\right) + x\left(\frac{x}{L}\right)^2 \tag{6.11}$$

In matrix form, Eqs. (6.2) through (6.7) result into:

$$\begin{bmatrix} \delta\alpha(x) \\ \delta\alpha'(x) \\ \delta\alpha''(x) \\ \delta\beta(x) \\ \delta\beta'(x) \\ \delta\beta''(x) \end{bmatrix} = \begin{bmatrix} N_1 & N_2 & N_3 & N_4 & 0 & 0 & 0 & 0 \\ N'_1 & N'_2 & N'_3 & N'_4 & 0 & 0 & 0 & 0 \\ N''_1 & N''_2 & N''_3 & N''_4 & 0 & 0 & 0 & 0 \\ 0 & 0 & 0 & 0 & N_1 & N_2 & N_3 & N_4 \\ 0 & 0 & 0 & 0 & N'_1 & N'_2 & N'_3 & N'_4 \\ 0 & 0 & 0 & 0 & N''_1 & N''_2 & N''_3 & N''_4 \end{bmatrix} \begin{bmatrix} \delta\alpha_1 \\ \delta\alpha'_1 \\ \delta\alpha_2 \\ \delta\alpha'_2 \\ \delta\beta_1 \\ \delta\beta'_1 \\ \delta\beta_2 \\ \delta\beta'_2 \end{bmatrix} \tag{6.12}$$

or

$$\delta\mathbf{v}^{\mathrm{P}} = \mathbf{B}^{\mathrm{P}}\delta\mathbf{q}_{\mathrm{n}}^{\mathrm{P}} \tag{6.13}$$

where $\mathbf{B}^{\mathrm{P}}$ are the interpolation functions for the local buckling DOFs and $\mathbf{q}_{\mathrm{n}}^{\mathrm{P}}$ is a subset of $\mathbf{q}_{\mathrm{n}}$ in Eq. (6.1a) that holds the flange rotations and curvatures.

Taking the rotations for each flange plate and using the following relationship based on plate theory (Hughes 1987),

$$v_P(x, y, z) = -z\,\Theta_P(x, y) \tag{6.14}$$

the beam displacements for the top and bottom plates are:

$$\begin{aligned} u_{top}^{P}(x) &= z\,\alpha'(x) \\ v_{top}^{P}(x) &= -z\,\alpha(x) \\ w_{top}^{P}(x) &= \alpha(x) \\ u_{bot}^{P}(x) &= z\,\beta'(x) \\ v_{bot}^{P}(x) &= -z\,\beta(x) \\ w_{bot}^{P}(x) &= \beta(x) \end{aligned} \tag{6.15}$$

Consideration of web plate displacements require more elaborate set of interpolation functions if the *y*-*z* plane origin is shifted from the top (or bottom) of the web plate to the web mid-height. A shift of the coordinate system results to the boundaries of the web-height changing from $0 \le y^* \le h_0$ to $-\frac{h_0}{2} \le y \le \frac{h_0}{2}$, where y^* is the range of the original frame, y is the range of the shifted frame, and h_0 is the total web plate height. The web plate's displacements are dependent on each flange's deformations and is represented with cubic functions. Because of the web plate's shift of reference axis, the cubic Hermitian shape functions are adjusted from those seen in Eqs. (6.8) and (6.10). The adjusted shape functions required for the web plate displacements are:

$$N_2^*(y) = \frac{h_0}{8} - \frac{y}{4} - \frac{y^2}{2h_0} + \frac{y^3}{{h_0}^2} \tag{6.16}$$

$$N_4^*(y) = -\frac{h_0}{8} - \frac{y}{4} + \frac{y^2}{2h_0} + \frac{y^3}{{h_0}^2} \tag{6.17}$$

A web plate fiber that exists in a linearly web-tapered member has a constant ratio of $\xi = y/h_0$ when the reference axis is located at the mid-height. Therefore, Eqs. (6.16) and (6.17) yield:

$$N_2^*(y) = h_0\left(\frac{1}{8} - \frac{\xi}{4} - \frac{\xi^2}{2} + \xi^3\right) \tag{6.18}$$

$$N_4^*(y) = h_0\left(-\frac{1}{8} - \frac{\xi}{4} + \frac{\xi^2}{2} + \xi^3\right) \tag{6.19}$$

The following equations are used to obtain the displacements of the web plate:

$$\begin{aligned} w_{web}^P(x) &= N_2^*(y)\,\beta(x) + N_4^*(y)\,\alpha(x) \\ u_{web}^P(x) &= -w_{,x} \\ v_{web}^P(x) &= -w_{,y} \end{aligned} \tag{6.20}$$

Taking the necessary derivatives, the forms for the web displacements are:

$$\begin{aligned} u_{web}^P(x) &= -[h_0'\,C_1\,\beta(x) + h_0\,C_1\,\beta'(x) + h_0'\,C_2\,\alpha(x) + h_0\,C_2\,\alpha'(x)] \\ v_{web}^P(x) &= -[C_3\,\beta(x) + C_4\,\alpha(x)] \\ w_{web}^P(x) &= h_0\,C_1\,\beta(x) + h_0\,C_2\,\alpha(x) \end{aligned} \tag{6.21}$$

where

$$C_1 = \frac{1}{8} - \frac{\xi}{4} - \frac{\xi^2}{2} + \xi^3 \tag{6.22}$$

$$C_2 = -\frac{1}{8} - \frac{\xi}{4} + \frac{\xi^2}{2} + \xi^3 \tag{6.23}$$

$$C_3 = -\frac{1}{4} - \xi + 3\xi^2 \tag{6.24}$$

$$C_4 = -\frac{1}{4} + \xi + 3\xi^2 \tag{6.25}$$

Strains obtained from plate theory are based on the curvatures involved. Thus, the second derivatives of the member's displacements referred to in Eqs. (6.15) and (6.21) are taken in order to obtain these strain relations. The proposed beam-column element is assumed to have no curvature at the flange plates along the z-axis. Therefore, the curvatures for each plate are:

$$\begin{aligned} \kappa_x^{top} &= v''^P_{top}(x) = -z\,\alpha''(x) \\ \kappa_z^{top} &= 0 \\ \kappa_{xz}^{top} &= -\alpha'(x) \end{aligned} \tag{6.26}$$

for the top flange,

$$\begin{aligned} \kappa_x^{bot} &= v''^P_{bot}(x) = -z\,\beta''(x) \\ \kappa_z^{bot} &= 0 \\ \kappa_{xz}^{bot} &= -\beta'(x) \end{aligned} \tag{6.27}$$

for the bottom flange, and

$$\begin{aligned} \kappa_x^{web} &= 2h_0'\,C_1\,\beta'(x) + h_0\,C_1\,\beta''(x) + 2h_0'\,C_2\,\alpha'(x) + h_0\,C_2\,\alpha''(x) \\ \kappa_y^{web} &= w(x)_{,yy} = \frac{C_{3,y}}{h_0}\,\beta(x) + \frac{C_{4,y}}{h_0}\,\alpha(x) \\ \kappa_{xy}^{web} &= w(x)_{,yx} = C_3\,\beta'(x) + C_4\,\alpha'(x) \end{aligned} \tag{6.28}$$

for the web.

The variation of these equations combined into matrix form results in the following:

$$\begin{bmatrix} \delta\kappa_x^{top} \\ \delta\kappa_{xz}^{top} \\ \delta\kappa_x^{bot} \\ \delta\kappa_{xz}^{bot} \\ \delta\kappa_x^{web} \\ \delta\kappa_y^{web} \\ \delta\kappa_{xy}^{web} \end{bmatrix} = \begin{bmatrix} 0 & 0 & -z & 0 & 0 & 0 \\ 0 & -1 & 0 & 0 & 0 & 0 \\ 0 & 0 & 0 & 0 & 0 & -z \\ 0 & 0 & 0 & 0 & -1 & 0 \\ 0 & 2h_0' C_2 & h_0 C_2 & 0 & 2h_0' C_1 & h_0 C_1 \\ \frac{C_{4,y}}{h_0} & 0 & 0 & \frac{C_{3,y}}{h_0} & 0 & 0 \\ 0 & C_4 & 0 & 0 & C_3 & 0 \end{bmatrix} \begin{bmatrix} \delta\alpha(x) \\ \delta\alpha'(x) \\ \delta\alpha''(x) \\ \delta\beta(x) \\ \delta\beta'(x) \\ \delta\beta''(x) \end{bmatrix} \tag{6.29}$$

or

$$\delta\boldsymbol{\kappa} = \mathbf{S}^{\mathrm{P}} \cdot \delta\mathbf{v}^{\mathrm{P}} \tag{6.30}$$

where $\delta\boldsymbol{v}^P$ is a sub-vector of $\delta\mathbf{d} = [\delta\boldsymbol{v}^T \quad \delta\boldsymbol{v}^{PT}]^T$ and $\mathbf{v}$ is the vector defined in Eq. (2.12).

As mentioned by Rajasekaran and Murray (1973), the variational form of the virtual work incremental equilibrium equation is expressed as:

$$\frac{1}{2}\int_V \overline{\boldsymbol{\sigma}}_{ij}\, \delta\left(\mathbf{u}_{k,i}\, \mathbf{u}_{k,j}\right) dV + \frac{1}{2}\int_V \boldsymbol{\sigma}_{ij}\, \delta\left(\mathbf{u}_{i,j}\, \mathbf{u}_{j,i}\right) dV = \int_S \mathbf{t}_i\, \delta\mathbf{u}_i\, dS \tag{6.31}$$

where

$\overline{\boldsymbol{\sigma}}_{ij}$ = the stress tensor prior to the increment,

$\mathbf{t}_i$ = the increment in the surface traction vector,

$\mathbf{u}_i$ = the increment in the displacement vector,

$\boldsymbol{\sigma}_{ij}$ = the increment in the stress tensor,

V = the volume of the member, and

S = the surface of the member.

Re-written, Eq. (6.31) can symbolically be represented by:

$$\delta(\mathbf{I}_1 + \mathbf{I}_2 - \mathbf{I}_3) = 0 \tag{6.32}$$

such that

$$\delta \mathbf{I}_1 = \int_V \boldsymbol{\sigma}_{ij}\, \delta \mathbf{u}_{i,j}\, dV \tag{6.33}$$

$$\delta \mathbf{I}_2 = \frac{1}{2} \int_V \overline{\boldsymbol{\sigma}}_{ij}\, \delta\left(\mathbf{u}_{k,i}\, \mathbf{u}_{k,j}\right) dV \tag{6.34}$$

$$\delta \mathbf{I}_3 = \int_S \mathbf{t}_i\, \delta \mathbf{u}_i\, dS \tag{6.35}$$

Superposition is imposed in order to obtain the total displacement and total stress increments by summing the beam and plate components together (Rajasekaran and Murray 1973):

$$\mathbf{u}_i = \mathbf{u}_i^{\mathrm{B}} + \mathbf{u}_i^{\mathrm{P}} \tag{6.36}$$

$$\boldsymbol{\sigma}_{ij} = \boldsymbol{\sigma}_{ij}^{\mathrm{B}} + \boldsymbol{\sigma}_{ij}^{\mathrm{P}} \tag{6.37}$$

Because the beam component for the proposed element uses a single layer of fibers in each plate and the stresses are taken to be uniform through the plate thickness, the coupling terms obtained by substituting Eqs. (6.36) and (6.37) into Eq. (6.33) may be neglected. Therefore, $\delta \mathbf{I}_1$ can be re-written as:

$$\delta \mathbf{I}_1 = \int_V \boldsymbol{\sigma}_{ij}^{\mathrm{B}}\, \delta \mathbf{u}_{i,j}^{\mathrm{B}}\ \mathrm{dV} + \int_V \boldsymbol{\sigma}_{ij}^{\mathrm{P}}\, \delta \mathbf{u}_{i,j}^{\mathrm{P}}\ \mathrm{dV} \tag{6.38}$$

Substitution of Eq. (6.36) into Eq. (6.34) yields:

$$\delta \mathbf{I}_2 = \delta \left[\frac{1}{2} \int_V \overline{\boldsymbol{\sigma}}_{ij}\, \mathbf{u}_{k,i}^{\mathrm{B}}\, \mathbf{u}_{k,j}^{\mathrm{B}}\, \mathrm{dV} + \frac{1}{2} \int_V \overline{\boldsymbol{\sigma}}_{ij}\, \mathbf{u}_{k,i}^{\mathrm{P}}\, \mathbf{u}_{k,j}^{\mathrm{P}}\, \mathrm{dV} + \int_V \overline{\boldsymbol{\sigma}}_{ij}\, \mathbf{u}_{k,i}^{\mathrm{B}}\, \mathbf{u}_{k,j}^{\mathrm{P}}\, \mathrm{dV} \right] \tag{6.39}$$

Both Eqs. (6.38) and (6.39) are then simplified symbolically:

$$\delta \mathbf{I}_1 = \delta \mathbf{I}_1^{\mathrm{B}} + \delta \mathbf{I}_1^{\mathrm{P}} \tag{6.40}$$

$$\delta \mathbf{I}_2 = \delta \mathbf{I}_2^{\mathrm{B}} + \delta \mathbf{I}_2^{\mathrm{P}} + \delta \mathbf{I}_2^{\mathrm{BP}} \tag{6.41}$$

$\delta\mathbf{I}_1^{\mathrm{B}}$ and $\delta\mathbf{I}_2^{\mathrm{B}}$ come directly from the linear and geometric stiffness matrices previously mentioned in Chapter 2 for Tapered Element A, respectively. Because of this, more focus will cover the plate's linear components, geometric components, and coupling between beam and plate theory seen through the terms $\delta \boldsymbol{I}_1^P$, $\delta \boldsymbol{I}_2^P$, and $\delta \boldsymbol{I}_2^{BP}$, respectively.

Using virtual displacements, the following derivation of the element tangent stiffness matrix for the proposed beam-column element is formed:

$$\delta\mathbf{I}_3 = \delta\mathbf{I}_1 + \delta\mathbf{I}_2$$

$$\delta\mathbf{q}_{\mathrm{n}}{}^{\mathrm{T}}\mathbf{P} = \int_0^L \delta\mathbf{q}_{\mathrm{n}}{}^{\mathrm{T}}\mathbf{N}_2^{\mathrm{T}}\mathbf{N}_1^{\mathrm{T}}\mathbf{k}_{\mathrm{s}}\mathbf{N}_1\mathbf{N}_2\mathbf{q}_{\mathrm{n}}\,dx + \int_0^L \delta\mathbf{q}_{\mathrm{n}}{}^{\mathrm{T}}\mathbf{N}_4^{\mathrm{T}}\mathbf{G}\mathbf{N}_4\mathbf{q}_{\mathrm{n}}\,dx$$

$$\mathbf{P} = \left[\int_0^L \mathbf{N}_2^{\mathrm{T}}\mathbf{N}_1^{\mathrm{T}}\mathbf{k}_{\mathrm{s}}\mathbf{N}_1\mathbf{N}_2\,dx + \int_0^L \mathbf{N}_4^{\mathrm{T}}\mathbf{G}\mathbf{N}_4\,dx\right]\mathbf{q}_{\mathrm{n}}$$

$$= [\mathbf{K_M} + \mathbf{K_G}]\mathbf{q}_{\mathrm{n}} = \mathbf{K_{tan}}\,\mathbf{q}_{\mathrm{n}} \qquad (6.42)$$

where $\mathbf{K_M}$ is referred to as the linear stiffness matrix, and $\mathbf{K_G}$ is the geometric stiffness matrix. The section tangent stiffness matrix, $\mathbf{k}_{\mathrm{s}}$, will be discussed in Section 6.3. $\mathbf{N}_2$ is the shape function matrix composed of the beam and plate interpolation functions and structured such that the proper conversions from $\mathbf{q}_{\mathrm{n}}$ to $\mathbf{d}$ are ensured. The matrix $\mathbf{N}_4$ represents the matrix of shape functions structured such that the displacement field is converted to the deformation vector:

$$\mathbf{z} = [v_0' \quad \Theta_{1z} \quad \Theta_{1y} \quad w_0' \quad \Theta_{2z} \quad \Theta_{2y} \quad v_0'' \quad w_0'' \quad \phi \quad \phi' \quad \alpha \quad \alpha' \quad \beta \quad \beta']^T \qquad (6.43)$$

Full matrix form of $\mathbf{N}_1$, $\mathbf{N}_2$, and $\mathbf{N}_4$ can be referred to in the Appendix.

To obtain the new geometric stiffness matrix, Eq. (6.41) is decomposed and restructured, per assumptions made by Rajasekaran and Murray, to:

$$\delta\mathbf{I}_2 = \delta\mathbf{I}_2^{\mathrm{B}} + \left(\delta\mathbf{I}_2^{\mathrm{topP}} + \delta\mathbf{I}_2^{\mathrm{botP}} + \delta\mathbf{I}_2^{\mathrm{webP}}\right) + \left(\delta\mathbf{I}_2^{\mathrm{topBP}} + \delta\mathbf{I}_2^{\mathrm{botBP}} + \delta\mathbf{I}_2^{\mathrm{webBP}}\right) \tag{6.44}$$

where $\delta\mathbf{I}_2^{\mathrm{B}}$ is identical to Eq. (2.46). Contributions based on plate flexure and the coupling terms are separated by each plate of a cross-section as seen in Eq. (6.44). Thus, the geometric stiffness matrix can be obtained analogously through:

$$\mathbf{G} = \mathbf{G}^{\mathrm{B}} + \left(\mathbf{G}^{\mathrm{topP}} + \mathbf{G}^{\mathrm{botP}} + \mathbf{G}^{\mathrm{webP}}\right) + \left(\mathbf{G}^{\mathrm{topBP}} + \mathbf{G}^{\mathrm{botBP}} + \mathbf{G}^{\mathrm{webBP}}\right) \tag{6.45}$$

where

$$\mathbf{G}^{\mathrm{B}} = \begin{bmatrix} \mathbf{G}^1_{10\times10} & \mathbf{0}_{10\times4} \\ \mathbf{0}_{4\times10} & \mathbf{0}_{4\times4} \end{bmatrix} \tag{6.46}$$

$$\mathbf{G}^1 = \begin{bmatrix} 0 & & & & & & & & & \\ 0 & \frac{4}{30}P & & & & & & & sym. & \\ 0 & 0 & \frac{4}{30}P & & & & & & & \\ 0 & 0 & 0 & 0 & & & & & & \\ 0 & -\frac{1}{30}P & 0 & 0 & \frac{4}{30}P & & & & & \\ 0 & 0 & -\frac{1}{30}P & 0 & 0 & \frac{4}{30}P & & & & \\ 0 & 0 & 0 & 0 & 0 & 0 & 0 & & & \\ 0 & 0 & 0 & 0 & 0 & 0 & 0 & 0 & & \\ 0 & 0 & 0 & 0 & 0 & 0 & M_y & M_z & 0 & \\ 0 & 0 & 0 & 0 & 0 & 0 & 0 & 0 & 0 & W \end{bmatrix} \tag{6.47}$$

$$\mathbf{G}^{\mathrm{topP}} = \int_{A^{top}} \bar{\sigma}_x \begin{bmatrix} \mathbf{0}_{10\times10} & \mathbf{0}_{10\times4} \\ \mathbf{0}_{4\times10} & \mathbf{G}^2_{4\times4} \end{bmatrix} dA^{top} \tag{6.48}$$

$$\mathbf{G}^2 = \begin{bmatrix} 0 & & & sym. \\ 0 & z^2 & & \\ 0 & 0 & 0 & \\ 0 & 0 & 0 & 0 \end{bmatrix} \tag{6.49}$$

$$\mathbf{G}^{\mathrm{botP}} = \int_{A^{bot}} \bar{\sigma}_x \begin{bmatrix} \mathbf{0}_{10\times10} & \mathbf{0}_{10\times4} \\ \mathbf{0}_{4\times10} & \mathbf{G}^3_{4\times4} \end{bmatrix} dA^{bot} \tag{6.50}$$

$$\mathbf{G}^3 = \begin{bmatrix} 0 & & & sym. \\ 0 & 0 & & \\ 0 & 0 & 0 & \\ 0 & 0 & 0 & z^2 \end{bmatrix} \tag{6.51}$$

$$\mathbf{G}^{\text{webP}} = \int_{A^{web}} \bar{\sigma}_x \begin{bmatrix} \mathbf{0}_{10\times10} & \mathbf{0}_{10\times4} \\ \mathbf{0}_{4\times10} & \mathbf{G}^4_{4\times4} \end{bmatrix} dA^{web} \tag{6.52}$$

$$\mathbf{G}^4 = \begin{bmatrix} {h_0'}^2 {C_2}^2 & & & sym. \\ h\, h_0' {C_2}^2 & h^2 {C_2}^2 & & \\ {h_0'}^2\, C_1 C_2 & h_0\, h_0'\, C_1 C_2 & {h_0'}^2 {C_1}^2 & \\ h_0\, h_0'\, C_1 C_2 & {h_0}^2\, C_1 C_2 & h_0\, h_0'\, {C_1}^2 & {h_0}^2 {C_1}^2 \end{bmatrix} \tag{6.53}$$

$$\mathbf{G}^{\text{topBP}} = \int_{A^{top}} \bar{\sigma}_x \begin{bmatrix} \mathbf{0}_{10\times10} & sym. \\ \mathbf{G}^5_{4\times10} & \mathbf{0}_{4\times4} \end{bmatrix} dA^{top} \tag{6.54}$$

$$\boldsymbol{G}^5 = \begin{bmatrix} 0 & 0 & 0 & 0 & 0 & 0 & 0 & 0 & 0 & 0 \\ -z & 0 & 0 & 0 & 0 & 0 & 0 & 0 & 0 & z^2 \\ 0 & 0 & 0 & 0 & 0 & 0 & 0 & 0 & 0 & 0 \\ 0 & 0 & 0 & 0 & 0 & 0 & 0 & 0 & 0 & 0 \end{bmatrix} \tag{6.55}$$

$$\mathbf{G}^{\text{botBP}} = \int_{A^{bot}} \bar{\sigma}_x \begin{bmatrix} \mathbf{0}_{10x10} & sym. \\ \mathbf{G}^6_{4x10} & \mathbf{0}_{4x4} \end{bmatrix} dA^{bot} \tag{6.56}$$

$$\mathbf{G}^6 = \begin{bmatrix} 0 & 0 & 0 & 0 & 0 & 0 & 0 & 0 & 0 & 0 \\ 0 & 0 & 0 & 0 & 0 & 0 & 0 & 0 & 0 & 0 \\ 0 & 0 & 0 & 0 & 0 & 0 & 0 & 0 & 0 & 0 \\ -z & 0 & 0 & 0 & 0 & 0 & 0 & 0 & 0 & z^2 \end{bmatrix} \tag{6.57}$$

$$\mathbf{G}^{\text{webBP}} = \int_{A^{web}} \bar{\sigma}_x \begin{bmatrix} \mathbf{0}_{10\times10} & sym. \\ \mathbf{G}^7_{4\times10} & \mathbf{0}_{4\times4} \end{bmatrix} dA^{web} \tag{6.58}$$

$$\mathbf{G}^7 = \begin{bmatrix} 0 & 0 & 0 & h_0'\, C_2 & 0 & 0 & 0 & 0 & h_0'\, y'\, C_2 & y\, h_0'\, C_2 \\ 0 & 0 & 0 & h_0\, C_2 & 0 & 0 & 0 & 0 & h_0\, y'\, C_2 & y\, h_0\, C_2 \\ 0 & 0 & 0 & h_0'\, C_1 & 0 & 0 & 0 & 0 & h_0'\, y'\, C_1 & y\, h_0'\, C_1 \\ 0 & 0 & 0 & h_0'\, C_1 & 0 & 0 & 0 & 0 & h_0\, y'\, C_1 & y\, h_0\, C_1 \end{bmatrix} \tag{6.59}$$

6.3 Section Tangent Stiffness Matrix

Derivation of the section stiffness matrix in Eq. (6.42) is obtained through the same process as in Eq. (2.32). Final form of the updated section stiffness matrix is composed of both beam and plate components such that:

$$\mathbf{k}_{\mathrm{S}} = \begin{bmatrix} \mathbf{k}_{\mathrm{S}}^{\mathrm{B}} & \mathbf{0}_{6\times6} \\ \mathbf{0}_{6\times6} & \mathbf{k}_{\mathrm{S}}^{\mathrm{P}} \end{bmatrix} \tag{6.60}$$

where $\mathbf{k}_{\mathrm{S}}^{\mathrm{B}}$ is the matrix formed in Eq. (2.34) and $\boldsymbol{k}_s^P$ is obtained through:

$$\mathbf{k}_{\mathrm{S}}^{\mathrm{P}} = \mathbf{k}_{\mathrm{S}}^{\mathrm{Top}} + \mathbf{k}_{\mathrm{S}}^{\mathrm{Bot}} + \mathbf{k}_{\mathrm{S}}^{\mathrm{Web}} \tag{6.61}$$

Prior to using Eq. (2.32) to determine the section stiffness matrix for the section plate contributions, the constitutive matrix for the flexural rigidity modulus of the plates, $\mathbf{C}^{\mathrm{P}}$, must be established.

Similar relations can be made between moments and curvatures for plate theory as were done for stress and strains for beam theory. Rajasekaran and Murray (1973) suggested these relations are established through:

$$\begin{aligned} M_\alpha &= -D\left(\kappa_\alpha + \nu\,\kappa_\beta\right) \\ M_\beta &= -D\left(\kappa_\beta + \nu\,\kappa_\alpha\right) \\ M_{\alpha\beta} &= -D(1-\nu)\kappa_{\alpha\beta} \end{aligned} \tag{6.62}$$

where ν is the Poisson's ratio. The aggregation of all incremental plate moments, incremental curvatures, and flexural rigidity modulus yield:

$$\begin{bmatrix} \Delta M_x^T \\ \Delta M_{xz}^T \\ \Delta M_x^B \\ \Delta M_{xz}^B \\ \Delta M_x^W \\ \Delta M_y^W \\ \Delta M_{xy}^W \end{bmatrix} = -\begin{bmatrix} D_x^T & & & & & & & \\ & D_{xz}^T(1-\nu) & & & & & & \\ & & D_x^B & & & & & \\ & & & D_{xz}^B(1-\nu) & & & & \\ & & & & D_x^W & D_y^W\nu & & \\ & & & & D_x^W\nu & D_y^W & & \\ & & & & & & D_{xy}^W(1-\nu) & \end{bmatrix} \begin{bmatrix} \Delta\kappa_x^T \\ \Delta\kappa_{xz}^T \\ \Delta\kappa_x^B \\ \Delta\kappa_{xz}^B \\ \Delta\kappa_x^W \\ \Delta\kappa_y^W \\ \Delta\kappa_{xy}^W \end{bmatrix}$$

or

$$\Delta\mathbf{M} = \mathbf{C}^{\mathrm{P}} \cdot \Delta\boldsymbol{\kappa} \tag{6.63}$$

Although Eq. (6.63) states the full constitutive relation between incremental moments and curvatures of the plates, the proposed element constrains a certain limitation. Ideally, treatment of the biaxial plate bending would be handled with a proper 2-D plate bending material model. However, the proposed element is currently only limited to use of uniaxial material models which only take in a single strain. Due to this limitation, each curvature must be treated independent of one another and thus results into various uses of uniaxial materials. But since the moment capacity is limited by the plastic moment, M_P, utilizing multiple uniaxial materials and treating them to be additive, as seen in the case of ΔM_x^W, can potentially result into exceeding M_P.

Based on these constraints, an alternative form of Eq. (6.63) is suggested for the proposed element utilizing uniaxial material models. In order to avoid exceedance of the M_P value, bending about each plate axis is treated completely independent of the orthogonal axis. Due to this assumption, the coupled bending moments and off-diagonal constitutive modulus in Eq. (6.63) are omitted:

$$\begin{bmatrix} \Delta M_x^T \\ \Delta M_x^B \\ \Delta M_x^W \\ \Delta M_y^W \end{bmatrix} = \begin{bmatrix} -D_x^T & & & \\ & -D_x^B & & \\ & & -D_x^W & \\ & & & -D_y^W \end{bmatrix} \begin{bmatrix} \Delta \kappa_x^T \\ \Delta \kappa_x^B \\ \Delta \kappa_x^W \\ \Delta \kappa_y^W \end{bmatrix} \tag{6.64}$$

The components that constitute Eq. (6.61) are therefore:

$$\mathbf{k}_{\mathrm{s}}^{\mathrm{Top}} = \int_{A^{Top}} \begin{bmatrix} 0 & 0 & 0 & 0 & 0 & 0 \\ 0 & 0 & 0 & 0 & 0 & 0 \\ 0 & 0 & -D_x^{top} z^2 & 0 & 0 & 0 \\ 0 & 0 & 0 & 0 & 0 & 0 \\ 0 & 0 & 0 & 0 & 0 & 0 \\ 0 & 0 & 0 & 0 & 0 & 0 \end{bmatrix} dA^{Top} \tag{6.65}$$

$$\mathbf{k}_{\mathrm{s}}^{\mathrm{Bot}} = \int_{A^{Bot}} \begin{bmatrix} 0 & 0 & 0 & 0 & 0 & 0 \\ 0 & 0 & 0 & 0 & 0 & 0 \\ 0 & 0 & 0 & 0 & 0 & 0 \\ 0 & 0 & 0 & 0 & 0 & 0 \\ 0 & 0 & 0 & 0 & 0 & 0 \\ 0 & 0 & 0 & 0 & 0 & -D_x^{bot} z^2 \end{bmatrix} dA^{Bo} \tag{6.66}$$

$$\mathbf{k}_{\mathrm{s}}^{\mathrm{Web}} = \int_{A^{web}} \begin{bmatrix} \boldsymbol{k}_s^{Web,1} & sym. \\ \boldsymbol{k}_s^{Web,2} & \boldsymbol{k}_s^{Web,3} \end{bmatrix} dA^{Web} \tag{6.67}$$

$$\mathbf{k}_{\mathrm{s}}^{\mathrm{Web,1}} = \begin{bmatrix} \dfrac{-D_y^{web}\ C_{4,y}{}^2}{h_0{}^2} & & sym. \\ 0 & -D_x^{web}\left(2\ h_0'\ C_2\right)^2 & \\ 0 & -2D_x^{web}\ h_0\ h_0'\ C_2{}^2 & -D_x^{web}\left(h_0\ C_2\right)^2 \end{bmatrix} \tag{6.68}$$

$$\mathbf{k}_{\mathrm{s}}^{\mathrm{Web,2}} = \begin{bmatrix} \dfrac{-D_y^{web}\ C_{3,y}\ C_{4,y}}{h_0{}^2} & 0 & 0 \\ 0 & -D_x^{web}\left(2\ h_0'\right)^2 C_1 C_2 & -2D_x^{web}\ h_0\ h_0'\ C_1 C_2 \\ 0 & -2D_x^{web}\ h_0\ h_0'\ C_1 C_2 & -D_x^{web}\ h_0{}^2\ C_1 C_2 \end{bmatrix} \tag{6.69}$$

$$\mathbf{k}_{\mathrm{s}}^{\mathrm{Web,3}} = \begin{bmatrix} \dfrac{-D_y^{web}\ C_{3,y}{}^2}{h_0{}^2} & & sym. \\ 0 & -D_x^{web}\left(2\ h_0'\ C_1\right)^2 & \\ 0 & -2D_x^{web}\ h_0\ h_0'\ C_1{}^2 & -D_x^{web}\left(h_0\ C_1\right)^2 \end{bmatrix} \tag{6.70}$$

Corresponding section stresses are obtained through the relation:

$$\mathbf{D}^{\mathrm{P}} = \int_A \mathbf{S}^{\mathrm{P}^{\mathrm{T}}} \mathbf{M}\, dA \tag{6.71}$$

Since the moments are taken to be per unit width of a plate, the integration boundaries are changed:

$$\mathbf{D}^{\mathrm{P}} = \int_w \mathbf{S}^{\mathrm{P}^{\mathrm{T}}} \mathbf{M}\, dw \tag{6.72}$$

and thus resulting the section stresses due to the plate contributions:

$$\mathbf{D}^{\mathrm{P}} = \begin{bmatrix} \int_w \left(\frac{1}{h_0} C_{4,y} \Delta M_y^W\right) dw \\ \int_w (2h_0' C_2 \Delta M_x^W) dw \\ \int_w (-z\Delta M_x^T)\, dw + \int_w (h_0 C_2 \Delta M_x^W)\, dw \\ \int_w \left(\frac{1}{h_0} C_{3,y} \Delta M_y^W\right) dw \\ \int_w (2h_0' C_1 \Delta M_x^W) dw \\ \int_w (-z\Delta M_x^B)\, dw + \int_w (h_0 C_1 \Delta M_x^W)\, dw \end{bmatrix} \tag{6.73}$$

Unlike the section stresses obtained in Tapered Element A, the section stresses seen in Eq. (6.73) do not have a significant physical interpretation (i.e., axial force, bending moment, etc.).

6.4 Discretization for Finite Element Implementation

Conversion of the closed form solutions, seen in Sections 6.2 and 6.3, are necessary prior to implementing Tapered Element B into OpenSees. Use of fiber discretization is used, as discussed in 2.6, in order to transform the integral form of the section stiffness matrix and stress resultant vector. Similar to Tapered Element A, each plate of a member's

cross-section is assumed to only have a single row of fibers along the plate width (see Figure 2.4). Therefore, the form of Eqs. (6.65) through (6.67) and Eq. (6.73) are replaced with:

$$\mathbf{k}_{\mathrm{s}}^{\mathrm{Top}} = \sum_{i=1}^{n^{top}} \begin{bmatrix} 0 & 0 & 0 & 0 & 0 & 0 \\ 0 & 0 & 0 & 0 & 0 & 0 \\ 0 & 0 & -D_x^{top} z^2 & 0 & 0 & 0 \\ 0 & 0 & 0 & 0 & 0 & 0 \\ 0 & 0 & 0 & 0 & 0 & 0 \\ 0 & 0 & 0 & 0 & 0 & 0 \end{bmatrix} \frac{A_i}{t_{pi}^{top}} \tag{6.74}$$

$$\mathbf{k}_{\mathrm{s}}^{\mathrm{Bot}} = \sum_{i=1}^{n^{bot}} \begin{bmatrix} 0 & 0 & 0 & 0 & 0 & 0 \\ 0 & 0 & 0 & 0 & 0 & 0 \\ 0 & 0 & 0 & 0 & 0 & 0 \\ 0 & 0 & 0 & 0 & 0 & 0 \\ 0 & 0 & 0 & 0 & 0 & 0 \\ 0 & 0 & 0 & 0 & 0 & -D_x^{bot} z^2 \end{bmatrix} \frac{A_i}{t_{pi}^{bot}} \tag{6.75}$$

$$\mathbf{k}_{\mathrm{s}}^{\mathrm{Web}} = \sum_{i=1}^{n^{Web}} \begin{bmatrix} \boldsymbol{k}_s^{Web,1} & sym. \\ \boldsymbol{k}_s^{Web,2} & \boldsymbol{k}_s^{Web,3} \end{bmatrix} \frac{A_i}{t_{pi}^{web}} \tag{6.76}$$

$$\mathbf{D}^{\mathrm{P}} = \begin{bmatrix} \sum_{\boldsymbol{i=1}}^{\boldsymbol{n^{Web}}} \left(\frac{1}{h_0} C_{4,yi} \Delta M_{yi}^W \right) \frac{A_i}{t_{pi}^{web}} \\ \sum_{\boldsymbol{i=1}}^{\boldsymbol{n^{Web}}} (2h_0' C_{2i} \Delta M_{xi}^W) \frac{A_i}{t_{pi}^{web}} \\ \sum_{\boldsymbol{i=1}}^{\boldsymbol{n^{Top}}} -z_i \Delta M_{xi}^T \frac{A_i}{t_{pi}^{top}} + \sum_{\boldsymbol{i=1}}^{\boldsymbol{n^{Web}}} (h_0 C_{2i} \Delta M_{xi}^W) \frac{A_i}{t_{pi}^{web}} \\ \sum_{\boldsymbol{i=1}}^{\boldsymbol{n^{Web}}} \left(\frac{1}{h_0} C_{3,yi} \Delta M_{yi}^W \right) \frac{A_i}{t_{pi}^{web}} \\ \sum_{\boldsymbol{i=1}}^{\boldsymbol{n^{Web}}} (2h_0' C_{1i} \Delta M_{xi}^W) \frac{A_i}{t_{pi}^{web}} \\ \sum_{\boldsymbol{i=1}}^{\boldsymbol{n^{Bot}}} -z_i \Delta M_{xi}^B \frac{A_i}{t_{pi}^{bot}} + \sum_{\boldsymbol{i=1}}^{\boldsymbol{n^{Web}}} (h_0 C_{1i} \Delta M_{xi}^W) \frac{A_i}{t_{pi}^{web}} \end{bmatrix} \tag{6.77}$$

where A_i is the area of a plate fiber and t_{pi} is the corresponding plate thickness.

6.5 Incorporating Tapered Element B into OpenSees

Incorporation of Tapered Element B into OpenSees follows a similar procedure described in Chapter 3. Tapered Element B is a more elaborate form of Tapered Element A which incorporates the plate theory discussed in Sections 6.2 and 6.3. These features are added to the implemented files of Tapered Element A and renamed such that both elements are available to the OpenSees users. The necessary files added to OpenSees for Tapered Element B relate to the Element class and Fiber Section class. Corresponding class calls for the new element formulation are distinguished through TaperedDispBeamColumnB3D and TaperedFiberSectionB3D.

Since each plate is treated to have its own section stiffness contribution, a fiber associated with the cross-section requires an additional parameter for the plate bending modulus, *D*. This additional material model for a plate fiber is associated with D_x^{top} for the top flange, D_x^{bot} for the bottom flange, and D_x^{web} and D_y^{web} for the web plate. Because Tapered Element B is simplified to neglect biaxial plate bending, uniaxial materials are used in determining the plate moduli previously mentioned. In the case of the web plate, the plate moduli for both the *x* and *y* bending use the same reference of the additional material call added for Tapered Element B.

6.6 Tapered Element B Preliminary Verification

Proceeding implementation of the 22-DOF Tapered Element B into OpenSees, verification was needed prior to re-assessing the response of cyclically tested specimens presented in Chapter 5. Because Tapered Element B, in a special case by excluding the

local buckling DOFs, has the same capabilities of Tapered Element A, it should be capable of replicating results of benchmark cases seen in Chapter 4.

This verification process included cases discussed by Andrade et al. (2007) which were modeled using Tapered Element B. Consistent modeling of these cases were done in the same fashion when using Tapered Element A. Difference of these models involved the incorporation of four DOFs per node. The nodes associated with member supports (i.e., fixed ends) were treated to have all the DOFs, including flange rotation and curvature, constrained. Varying use of element meshing was carried out with each case in Section 4.2.3 in order to be able to capture local buckling effects since these buckling modes are more concentrated in location compared to LTB modes. Element meshing for Case 1.b (see Figure 4.4), for instance, had a range of elements from 4 up to 20 along the cantilever beam.

It was observed that in cases where members were loaded directly at the node (web mid-height), exact results were obtained from that of Tapered Element A. However, difficulties occurred with cases involving cases of top flange or bottom flange loading with Tapered Element B involving abrupt termination mid-analysis or failure to start analyses in certain cases.

In addition to the monotonic pushover analyses in Chapter 4, test cases with local buckling were attempted based on the work of Rajasekaran and Murray (1973). Their documented cases involving elastic prismatic wide-flange members were modeled using Tapered Element B based on the stated boundary condition and geometrical properties. In particular, the case of an axially load column was modeled with the dimensions and finite element meshing stated by the authors. Although simulation of this case ran

successfully using Tapered Element B, results obtained showed no implication of local buckling and could not be compared to the results obtained by Rajasekaran and Murray. Because of these difficulties, further research and development of Tapered Element B is necessary.

6.7 Issues with Tapered Element B

6.7.1 Incorporation of Initial Imperfections

In order to initiate any form of buckling in numerical models, some form of imperfection must be imposed to the system. With beam-column elements, imperfections are typically imposed on a member through an initial out-of-plane displacement or even initial twist or bending. Application of such initial imperfection can easily be done through the nodal coordinates which connect the elements of a member.

In addition to initial lateral displacements, however, occurrences of imperfection throughout the web and flanges of built-up I-sections have also been reported from testing (see Figure 6.2). Unlike out-of-straightness imperfections, imposing flange imperfections cannot be easily handled through manipulation of a element's nodal coordinates. Because of this, initial displacements for the flanges must be imposed to the local buckling DOFs at each node. Although OpenSees has the option and capability of applying DOF initial displacements at the node, it is currently limited for use on the axial, transverse, and lateral DOFs (i.e., *u*, *v*, and *w* displacements). Further research is needed in order to incorporate imperfections in a similar fashion for the remaining DOFs such that local buckling can be captured with Tapered Element B.

Figure 6.2 Web Geometric Imperfection (Smith et al. 2013)

6.7.2 Corresponding Material Model For Tapered Element B

Formulation of Tapered Element B causes flange and web bending about axes both parallel and perpendicular to an element axis. This phenomenon is referred to as biaxial bending. Since biaxial bending of plates typically use two-dimensional plasticity models, assumptions of uniaxial material models to decouple plate bending may cause highly inaccurate results.

Alternatives such as stress-resultant models have promising potential for the Tapered Element B. With uniaxial materials, limitation is met when a fiber's stress state is solely dependent on the corresponding strain which is normal to the cross section. However, plate bending behavior is highly dependent on its curvatures more so than normal axial strains dealt with in cases of beams. Hence, a two-dimensional stress-resultant model would take into account multiple directions of a cross-section's stress state and then be compared to a yield surface criterion which determines occurrences of yielding. Examples

of such stress-resultant models are seen in a Von Mises model (SIMULIA Inc. 2013) which incorporate a yield surface as well as hardening flow rules to allow contributions of yielding from both member overall buckling, such as LTB, and local buckling.

7 SUMMARY AND CONCLUSIONS

7.1 Summary

Thin-walled metal members are typically seen in metal building frames (MBFs) which are commonly used throughout many of today's structures. To be economical, MBFs commonly utilize web-tapered members that correspond to the moment gradient along a member of the system; noncompact or slender sections are commonly used for this type of construction.

Generally, design of members in MBF systems is governed by lateral-torsional buckling (LTB) and local buckling. In order to better understand and study the behavior of these systems under earthquake excitations, numerical methods utilizing the finite element method can be useful in accomplishing these goals. Although various methods of modeling MBF systems can be done through various software, computational time and effort can be very exhausting for studies requiring extensive nonlinear time-history analyses of a suite of earthquake ground motions. Unlike shells or solids, one-dimensional line elements, when properly formulated, are efficient and easier to use in research that aims to develop a rational seismic design procedure for MBFs.

Use of beam-column line elements has been used by previous researchers to capture LTB phenomenon fairly well, such as Alemdar (2001), Chang (2006), and Zhang et al. (2011) to name a few. Such elements currently exist in the open source software OpenSees and is used by researchers and developers worldwide (McKenna et al. 2000). However, as it is, the current displacement-based beam-column element offered in OpenSees is unable to capture the effects of member global buckling, not to mention local buckling. Because

of this limitation, an alternative beam-column element formulation was needed in order to handle nonlinear analysis of systems involving events of member global buckling, especially LTB for MBFs.

The proposed element developed in this research introduced a new degree of freedom (DOF) in addition to the typical displacements and rotations seen at each node of a beam-column element. The additional DOF depicts a warping deformation which is shown to be crucial in analysis involving LTB. This nonlinear 14-DOF beam-column element has been implemented into OpenSees and is designated as Tapered Element A. Subsequent thorough verification with monotonic pushover models, correlation studies were done and compared to cyclic test data. Based on the observations from cyclic correlation study, an effort was also made to incorporate additional four DOFs at each node to simulate the local buckling effects. This 22-DOF beam-column is designated as Tapered Element B for OpenSees implementation.

7.2 Conclusions

Extensive testing and verification of Tapered Element A was carried out through numerous cases from previous works and experiments (Alemdar 2001, Andrade et al. 2007, Prawel et al. 1974, Shiomi and Kurata 1984). Variations of parameters such as elastic and inelastic materials were considered, various web-tapers, boundary conditions, loading locations (i.e., top or bottom flange loading), and residual stresses were considered. Correlation studies of experimental testing of web-tapered members under both monotonic and cyclic loadings were also carried out.

Correlation and observations of the monotonic analyses established in Chapter 4 showed that the predicted analyses are comparable to documented test data with small discrepancies. The following conclusions based on the results of these models are made:

- Flexural members involving elastic LTB compare well to results of more sophisticated elements, such as shells (Andrade et al. 2007).
- Different loading cases involving top flange and bottom flange loading can be done using rigid connecting elements (see Section 4.2.3) and are capable of yielding reasonable results.
- Materials based on true stress-strain relations and engineering stress-strain relations showed little to no difference of buckling load predictions. Post-buckling responses of these two models deviate and response of engineering stress-strain yields conservative results to that of true stress-strain results (see Figure 4.34).
- Application of constant axial load yields less strength capacity to results of incrementally increased axial load during an analysis. Post-buckling strength degradation is seen to show similar behavior in either case (see Figure 4.39).

Cyclic analysis of six full-scale specimens tested at UCSD (Smith et al. 2013) was conducted using Tapered Element A and correlated to test data. Predicted analysis results for all six specimens showed to correlate fairly well up to initial LTB. Upon initial LTB, however, test data showed significant strength degradation in the remaining excursion of current cycle, while the proposed element was unable to replicate. It was observed from testing that LTB almost always triggered simultaneous events of local buckling, especially flange local buckling (FLB), at the kink location(s) with the highest out-of-plane

curvatures. Since Tapered Element A could not simulate local buckling, similar behavior of strength degradation was not replicated.

In addition to cyclic correlation, several parametric studies were pursued to better understand the behavior and implications of varying axial load, initial imperfections, and residual stresses. The following conclusions were made:

- Response of cyclic behavior from constant axial compression showed significant differences of initial LTB and strength degradation than that without an axial compression (see Figure 5.10).
- Initial imperfections along the controlling unbraced segment involving LTB played little or no role in affecting cyclic results and behavior (see Figure 5.23).
- Residual stresses had a significant effect in responses of initial LTB and post-buckling behavior (see Figure 5.24). But response of subsequent cycles after initial LTB was unaffected for all variations of residual stresses.

7.3 Future Work

Based on the results observed from cyclic analyses, it was apparent that local buckling effects have a significant role in strength degradation. In attempt to capture these effects, Tapered Element B was developed (see Chapter 6) to incorporate DOFs associated with local buckling. Preliminary tests were done for this new element to compare its validity with LTB cases as well as local buckling cases. However, difficulties arose throughout this verification stage and prevented any further progress of using the element to re-evaluate the specimens of cyclic testing. Further research and development for

Tapered Element B is, therefore, needed to overcome these issues and limitations. The following issues need to be addressed:

- Incorporating a means of imposing initial displacements corresponding to the local buckling DOFs is needed to numerically trigger local buckling to occur in an analysis.
- Because Tapered Element B incorporates plate theory, development of a two-dimensional stress-resultant material model is ideal in order to handle bi-axial bending.
- Determine a consistent method and approach of using sufficient elements to ensure effects of local buckling are captured.

REFERENCES

AISC (2003), "Torsional Analysis of Structural Steel Members," *Steel Design Guide Series 9*, American Institute of Steel Construction, Chicago, IL.

AISC (2010a), *Specification for Structural Steel Buildings*, ANSI/AISC 360-10, American Institute of Steel Construction, Chicago, IL.

Alemdar, B.N. (2001), "Distributed Plasticity Analysis of Steel Building Structural Systems," *Doctoral Dissertation*, School of Civil and Enviornmental Engineering, Georgia Institute of Technology, Atlanta, GA.

Andrade, A., Camotim, D., and Dinis, P.B. (2007), "Lateral-Torsional Buckling of Singly Symmetric Web-Tapered Thin-Walled I-Beams: 1D Model vs. Shell FEA," *Computers & Structures*, Vol. 85, Issues 17-18, pp. 1343-1359.

ASCE/SEI (2010), *Minimum Design Loads for Buildings and Other Structures*, ASCE/SEI 7-10, American Society of Civil Engineers, New York, NY.

Belytschoko, T., Liu, W.K., and Moran, B. (2000), *Nonlinear Finite Elements for Continua and Structures*, John Wiley & Sons Inc, Hoboken, NJ.

Bradford, M.A., Cuk, P.E., Gizejowski, M.A., and Traheir, N. (1987), "Inelastic Lateral Buckling of Beam-Columns", *Journal of Engineering Mechanics*, Vol. 113, No. 11, pp. 2259-2277, American Society of Civil Engineers, New York, NY.

Chang, C.J. (2006), "Construction Simulation of Curved Steel I-Girder Bridges," *Doctoral Dissertation*, School of Civil and Environmental Engineering Georgia Institute of Technology, Atlanta, GA.

Chen, W.F. and Lui, E.M. (1987), *Structural Stability: Theory and Implementaion*, Elsevier Science Publish Co., Inc., New York, NY.

Crisfield, M.A. (1990), "A Consistent Co-Rotational Formulation for Non-Linear, Three-Dimensional, Beam-Elements," *Computer Methods in Applied Mechanics and Engineering*, Vol. 81, Issue 2, pp. 131-150.

Crisfield, M.A. (1991), *Nonlinear Finite Element Analysis of Solids and Structures, Volume 1: Essentials*, John Wiley & Sons.

FEMA (2009), "Quantification of Building Seismic Performance Factors," *FEMA P695*, Washington, D.C.

Fenves, G.L. (2004), "An Object-Oriented Software Enviornment for Collaborative Network Simulation." *World Conference on Earthquake Engineering*, Paper No. 1492.

Kim, Y.D. (2010), "Behavior and Design of Metal Building Frames Using General Prismatic and Web-Tapered Steel I-Section Members," *Doctoral Dissertation*, School of Civil and Environmental Engineering Georgia Institute of Technology, Atlanta, GA.

Kitipornchai, S. and Trahair, N.S. (1975), "Elastic Behavior of Tapered Monosymmetric I-Beams," *Journal of the Structural Division*, Vol. 101, No. 8, pp. 1661-1678, American Society of Civil Engineers, New York, NY.

Kitipornchai, S. and Trahair, N.S. (1975), "Buckling of Inelastic I-Beams Under moment Gradient," *Journal of the Structural Division*, Vol. 101, No. 5, pp. 991-1004, American Society of Civil Engineers, New York, NY.

McKenna, F., Genves, G.L., and Scott, M.H. (2000), "Open System for Earthquake Engineering Simulation," http://opensees.berkeley.edu, University of California, Berkeley, Berkeley, CA.

Newman, A. (2004), *Metal Building Systems: Design and Specifications*, 2nd Edition, McGraw-Hill, New York, NY.

Prawel, S.P., Morrell, M.L., and Lee, G.C. (1974), "Bending and Buckling Strength of Tapered Structural Members," *Welding Research Supplement*, Vol. 53, pp. 75-84.

Rajasekaran, S. and Murray, D.W. (1973), "Coupled Local Buckling in Wide-Flange Beam-Columns," *Journal of the Structural Division*, Vol. 99, No. 6, pp. 1003-1023, American Society of Civil Engineers, New York, NY.

Ronagh, H.R., Bradford, M.A., and Attard, M.M. (2000), "Nonlinear Analysis of Thin-Walled Members of Variable Cross-Section. Part I: Theory," *Computers and Structures*, No. 77, Issue 3, pp. 285-299.

Shiomi, H. and Kurata, M. (1984), "Strength Formula for Tapered Beam-Columns," *Journal of Structural Engineering*, Vol. 110, pp. 1630-1643.

SIMULIA, Inc. (2014), ABAQUS, Version 6.13, SIMULIA, Inc., Dassault Systems, Providence, RI.

Smith, M.D. (2013), "Seismic Testing and Analytical Studies for the Development of New Seismic Force Resisting Systems for Metal Buildings," *Doctoral Dissertation*, Department of Structural Engineering, University of California, San Diego, La Jolla, CA.

Smith, M.D., Turner, K.A., and Uang, C.M. (2013), "Experimental Study of Cyclic Lateral-Torsional Buckling of Web-Tapered I-Beams," *Report No. SSRP-12/06*, Department of Structural Engineering, University of California, San Diego, La Jolla, CA.

Ugural, A.C. and Fenster, S.K. (2012), *Advanced Mechanics of Materials and Applied Elasticity*, Pearson Education, Inc., Westford, MA.

Yang, Y.B. and McGuire, W. (1986), "Stiffness Matrix for Geometric Nonlinear Analysis," *Journal of the Structural Division*, Vol. 112, No. 4, pp. 853-877, American Society of Civil Engineers, New York, NY.

Yang, Y.B. and Yau, J.D. (1987), "Stability of Beams with Tapered I-Sections," *Journal of Engineering Mechanics*, Vol. 113, No. 9, pp. 1337-1357, American Society of Civil Engineers, New York, NY.

Zhang, X., Rasmussen, K.J.R., and Zhang, H. (2011), "Formulation and Implementation of Three-Dimensional Doubly-Symmetric Beam-Column Analyses with Warping Effects in OpenSees," *Research Report R917*, School of Civil Engineering, The University of Sydney.

APPENDIX: DEFINITION OF N_1, N_2, AND N_4

Discussion of the element stiffness matrix for Tapered Element B was formulated in Chapter 6. It was shown that derivation of the element stiffness matrix involved using matrices defined as $\boldsymbol{N}_1$, $\boldsymbol{N}_2$, and $\boldsymbol{N}_4$. These matrices are defined in their entirety throughout this section.

The $\boldsymbol{N}_1$ matrix is:

$$\boldsymbol{N}_1 = \begin{bmatrix} \boldsymbol{Q} & \boldsymbol{0}_{7\times5} \\ \boldsymbol{0}_{6\times12} & \boldsymbol{I}_{6\times6} \end{bmatrix} \tag{A.1}$$

where $\boldsymbol{0}_{m\times n}$ is a zero matrix that has a size of *m* by *n*, $\boldsymbol{I}_{n\times n}$ an identity matrix with a size of *n* by *n*, and $\boldsymbol{Q}$ defined in Eq. (2.44) as

$$\boldsymbol{Q} = \begin{bmatrix} 1 & \frac{1}{30}\Theta_n^T\boldsymbol{X} & 0 & 0 & 0 & 0 & 0 & 0 \\ 0 & 0 & 0 & 1 & \phi & w_0'' & 0 & 0 \\ 0 & 0 & 0 & \phi & -1 & v_0'' & 0 & 0 \\ 0 & 0 & 0 & 0 & 0 & 0 & \phi' & 0 \\ 0 & 0 & 0 & 0 & 0 & 0 & 0 & 1 \\ 0 & 0 & 0 & 0 & 0 & 0 & 1 & 0 \end{bmatrix} \tag{A.2}$$

$$\boldsymbol{X} = \begin{bmatrix} 0 & 0 & 0 & 0 & 0 & 0 \\ 0 & 4 & 0 & 0 & -1 & 0 \\ 0 & 0 & 4 & 0 & 0 & -1 \\ 0 & 0 & 0 & 0 & 0 & 0 \\ 0 & -1 & 0 & 0 & 4 & 0 \\ 0 & 0 & -1 & 0 & 0 & 4 \end{bmatrix} \tag{A.3}$$

The $\boldsymbol{N}_2$ matrix is:

$$\boldsymbol{N}_2 = \begin{bmatrix} \boldsymbol{B}_1 & \boldsymbol{B}_2 & \boldsymbol{B}_3 \\ \boldsymbol{B}_4 & \boldsymbol{B}_5 & \boldsymbol{0}_{5\times1} \\ \boldsymbol{B}_6 & \boldsymbol{B}_7 & \boldsymbol{0}_{6\times1} \end{bmatrix} \tag{A.4}$$

$$\boldsymbol{B}_1 = \begin{bmatrix} 0 & 0 & 0 & 0 & 0 & 0 & 0 & 0 \\ 1 & 0 & 0 & 0 & 0 & 0 & 0 & 0 \\ 0 & 1 & 0 & 0 & 0 & 0 & 0 & 0 \\ 0 & 0 & 1 & 0 & 0 & 0 & 0 & 0 \\ 0 & 0 & 0 & 0 & 0 & 0 & 0 & 0 \\ 0 & 0 & 0 & 0 & 0 & 0 & 0 & 0 \\ 0 & 0 & 0 & 0 & 0 & 0 & 0 & 0 \end{bmatrix} \tag{A.5}$$

$$\boldsymbol{B}_2 = \begin{bmatrix} 0 & 0 & 0 & 0 & 0 & 0 & 0 & 0 \\ 0 & 0 & 0 & 0 & 0 & 0 & 0 & 0 \\ 0 & 0 & 0 & 0 & 0 & 0 & 0 & 0 \\ 0 & 0 & 0 & 0 & 0 & 0 & 0 & 0 \\ 1 & 0 & 0 & 0 & 0 & 0 & 0 & 0 \\ 0 & 1 & 0 & 0 & 0 & 0 & 0 & 0 \\ 0 & 0 & 1 & 0 & 0 & 0 & 0 & 0 \end{bmatrix} \tag{A.6}$$

$$\boldsymbol{B}_3 = \begin{bmatrix} N_u' \\ 0 \\ 0 \\ 0 \\ 0 \\ 0 \\ 0 \end{bmatrix} \tag{A.7}$$

$$\boldsymbol{B}_4 = \begin{bmatrix} 0 & N_{v1}'' & 0 & 0 & 0 & 0 & 0 & 0 \\ 0 & 0 & -N_{w1}'' & 0 & 0 & 0 & 0 & 0 \\ N_{\phi 1} & 0 & 0 & N_{\phi 2} & 0 & 0 & 0 & 0 \\ N_{\phi 1}' & 0 & 0 & N_{\phi 2}' & 0 & 0 & 0 & 0 \\ N_{\phi 1}'' & 0 & 0 & N_{\phi 2}'' & 0 & 0 & 0 & 0 \end{bmatrix} \tag{A.8}$$

$$\boldsymbol{B}_5 = \begin{bmatrix} 0 & N_{v2}'' & 0 & 0 & 0 & 0 & 0 & 0 \\ 0 & 0 & -N_{w2}'' & 0 & 0 & 0 & 0 & 0 \\ N_{\phi 3} & 0 & 0 & N_{\phi 4} & 0 & 0 & 0 & 0 \\ N_{\phi 3}' & 0 & 0 & N_{\phi 4}' & 0 & 0 & 0 & 0 \\ N_{\phi 3}'' & 0 & 0 & N_{\phi 4}'' & 0 & 0 & 0 & 0 \end{bmatrix} \tag{A.9}$$

$$\boldsymbol{B}_6 = \begin{bmatrix} 0 & 0 & 0 & 0 & N_1 & N_2 & 0 & 0 \\ 0 & 0 & 0 & 0 & N_1' & N_2' & 0 & 0 \\ 0 & 0 & 0 & 0 & N_1'' & N_2'' & 0 & 0 \\ 0 & 0 & 0 & 0 & 0 & 0 & N_1 & N_2 \\ 0 & 0 & 0 & 0 & 0 & 0 & N_1' & N_2' \\ 0 & 0 & 0 & 0 & 0 & 0 & N_1'' & N_2'' \end{bmatrix} \tag{A.10}$$

$$\boldsymbol{B}_7 = \begin{bmatrix} 0 & 0 & 0 & 0 & N_3 & N_4 & 0 & 0 \\ 0 & 0 & 0 & 0 & N_3' & N_4' & 0 & 0 \\ 0 & 0 & 0 & 0 & N_3'' & N_4'' & 0 & 0 \\ 0 & 0 & 0 & 0 & 0 & 0 & N_3 & N_4 \\ 0 & 0 & 0 & 0 & 0 & 0 & N_3' & N_4' \\ 0 & 0 & 0 & 0 & 0 & 0 & N_3'' & N_4'' \end{bmatrix} \quad \text{(A.11)}$$

The $\boldsymbol{N}_4$ matrix is:

$$\boldsymbol{N}_4 = \begin{bmatrix} \boldsymbol{B}_8 & \boldsymbol{B}_9 & \boldsymbol{0}_{7\times1} \\ \boldsymbol{B}_{10} & \boldsymbol{B}_{11} & \boldsymbol{0}_{7\times1} \end{bmatrix} \quad \text{(A.12)}$$

$$\boldsymbol{B}_8 = \begin{bmatrix} 0 & N_{v1}' & 0 & 0 & 0 & 0 & 0 & 0 \\ 0 & 1 & 0 & 0 & 0 & 0 & 0 & 0 \\ 0 & 0 & 1 & 0 & 0 & 0 & 0 & 0 \\ 0 & 0 & -N_{w1}' & 0 & 0 & 0 & 0 & 0 \\ 0 & 0 & 0 & 0 & 0 & 0 & 0 & 0 \\ 0 & 0 & 0 & 0 & 0 & 0 & 0 & 0 \\ 0 & N_{v1}'' & 0 & 0 & 0 & 0 & 0 & 0 \end{bmatrix} \quad \text{(A.13)}$$

$$\boldsymbol{B}_9 = \begin{bmatrix} 0 & N_{v2}' & 0 & 0 & 0 & 0 & 0 & 0 \\ 0 & 0 & 0 & 0 & 0 & 0 & 0 & 0 \\ 0 & 0 & 0 & 0 & 0 & 0 & 0 & 0 \\ 0 & 0 & 0 & 0 & 0 & 0 & 0 & 0 \\ 0 & 0 & -N_{w2}' & 0 & 0 & 0 & 0 & 0 \\ 0 & 1 & 0 & 0 & 0 & 0 & 0 & 0 \\ 0 & 0 & 1 & 0 & 0 & 0 & 0 & 0 \end{bmatrix} \quad \text{(A.14)}$$

$$\boldsymbol{B}_{10} = \begin{bmatrix} 0 & 0 & -N_{w1}'' & 0 & 0 & 0 & 0 & 0 \\ N_{\phi1} & 0 & 0 & N_{\phi2} & 0 & 0 & 0 & 0 \\ N_{\phi1}' & 0 & 0 & N_{\phi2}' & 0 & 0 & 0 & 0 \\ 0 & 0 & 0 & 0 & N_1 & N_2 & 0 & 0 \\ 0 & 0 & 0 & 0 & N_1' & N_2' & 0 & 0 \\ 0 & 0 & 0 & 0 & 0 & 0 & N_1 & N_2 \\ 0 & 0 & 0 & 0 & 0 & 0 & N_1' & N_2' \end{bmatrix} \quad \text{(A.15)}$$

$$\boldsymbol{B}_{11} = \begin{bmatrix} 0 & 0 & -N''_{w2} & 0 & 0 & 0 & 0 & 0 \\ N_{\phi 3} & 0 & 0 & N_{\phi 4} & 0 & 0 & 0 & 0 \\ N'_{\phi 3} & 0 & 0 & N'_{\phi 4} & 0 & 0 & 0 & 0 \\ 0 & 0 & 0 & 0 & N_3 & N_4 & 0 & 0 \\ 0 & 0 & 0 & 0 & N'_3 & N'_4 & 0 & 0 \\ 0 & 0 & 0 & 0 & 0 & 0 & N_3 & N_4 \\ 0 & 0 & 0 & 0 & 0 & 0 & N'_3 & N'_4 \end{bmatrix} \tag{A.16}$$